Universidad de Sevilla

Ph.D. Thesis
Doctoral Programme in Physical Sciences and Technologies
Faculty of Physics / National Centre of Accelerators

Development of an external beam line for radiobiology experiments and microdosimetry applications at the 18 MeV proton cyclotron facility at CNA

Author:
Anna Baratto Roldán

Directors:
Prof. Miguel Antonio Cortés Giraldo
Dr. María del Carmen Jiménez Ramos
Prof. José Manuel Espino Navas

November 2020

A mi familia

Acknowledgements

The accomplishment of this long desired objective in my academic career would not have been possible without the advice, support, help and encouragement of the many people I crossed paths with during these last four years. I am extremely grateful for all the experiences and opportunities I was gifted with, but also for the challenges I had to face; all of them made me grow as a researcher and, more importantly, as person.

First of all, I would like to express my sincere gratitude to my supervisors, A/Prof. Dr. Miguel Antonio Cortés Giraldo, Dr. María del Carmen Jiménez Ramos and A/Prof. Dr. José Manuel Espino Navas, for believing in me and encouraging me to go beyond my own limits. Their guidance and support were fundamental for the completion of this work, and I owe them most of the knowledge I acquired during my doctoral studies. I am especially thankful for the friendship they have always demonstrated, for the patience with which they listened to me during the bad times and for the enthusiasm with which they celebrated the many good ones.

My special appreciation and thanks go to Prof. Dr. María Isabel Gallardo Fuentes, for her contagious curiosity and endless desire to learn. She has been a great inspiration and mentor, keeping the flame of my enthusiasm alight. I would also like to show my deep gratitude to Prof. Dr. Joaquín Gómez Camacho, who put his trust in me, and fought the bureaucracy to give me the opportunity to teach. Along these lines, I wish to express my gratitude to all the other colleagues and personnel of the Department of Atomic, Molecular and Nuclear physics, for the warmth with which they welcomed me, making me feel as a part of the family.

This work would not have been possible without the help and involvement of many collaborators from different institutions. In the first place, I would like to thank Prof. Dr. Francisco Javier García López and Dr. Begoña Fernández Martínez, from the CNA, for being always available to help during experimental measurements and for retrieving and lending the necessary material and equipment. Secondly, my sincere gratitude goes to A/Prof. Alejandro Cárabe Fernández, from the Hospital of the University of Pennsylvania; without him the content of the third chapter of this

thesis would have never come to existence. The discussions and the sharing of ideas we had during our meetings, and the team working with my colleagues Dr. Alvaro Perales Molina and Dr. Alejandro Bertolet Reina, were very prolific and exciting, opening a whole new line of research. In this context, I would also like to thank Dr. Giorgio Baiocco and Dr. Sofia Barbieri, who dedicated their time and effort to produce simulation results to be compared with ours. Then, I wish to acknowledge Dr. Consuelo Guardiola (CNRS - Paris, France) and Dr. Dieter Schardt (GSI - Darmstadt, Germany), for their sincere interest in my thesis work and for the many advices and ideas they shared with us. Finally, my deepest gratitude goes to A/Prof. Dr. Sonia Jimeno González and A/Prof. Dr. Pablo Huertas Sánchez, from CABIMER, for offering their expertise, laboratories and time to make the irradiation of cell cultures at the cyclotron happen.

I would like to express my deepest gratitude to Prof. Dr. Carsten Welsch and to all the partners of the OMA project, for believing in it and making it real: they created an outstanding network that was a countless source of knowledge, collaborations and training experiences. Being an OMA fellow was, without any doubt, the most precious gift of these doctoral years, and I hope that the friendship and companionship I found in the network will accompany me throughout my life. A special mention goes to our project managers, Magdalena and Samantha, who gave all their best to organise the meetings and to make sure that everything was fine among us. I found in them careful listeners and supportive friends, and more than once they encouraged me to not give up. And of course, this project would not have existed without the brilliance and liveliness of its fellows, the true heart of OMA, who became my dearest friends. A sincere thank goes especially to Ewa, Sud, Jacinta, Navrit, Michelle, Laurent and Roland, for all the laughters and the great moments we shared together.

I am extremely thankful to Dr. Michael Scholz, Prof. Dr. Marco Durante, and all the people of the GSI biophysics department, for welcoming me during my secondment and making me feel at home. I really enjoyed the time I spent there, the continuous occasions for learning and improvement, and the stimulant environment. A special thank goes to Dr. Olga Sokol, who patiently introduced me to the world of radiobiology, spending many hours with me under the flow hood to guide my hands for the preparation of cell samples. I consider her a great teacher and a precious friend. I had the chance to meet many wonderful people during my time at the GSI, but Francesca and Claire deserve a special mention. Even if we could just spend a short time together, their friendship was, and still is, an unexpected and amazing treasure. They gave me strength, enthusiasm, self-confidence and countless happy memories.

Concludere questo lavoro di tesi, durante i mesi di isolamento ed incertezza portati

dal COVID-19, sarebbe stato estremamente difficile senza l'appoggio di tutti i miei amici dall'Italia. Nonostante la lontananza e la solitudine forzata, non c'è stato un giorno in cui mi abbiano fatto mancare il loro affetto e la loro presenza. In particolare desidero ringraziare Valeria, per essere sempre rimasta al mio fianco e avermi capita, sostenuta e spronata a non mollare. La sua vivacitá, il suo coraggio e la sua determinazione sono per me una fonte di ispirazione. Sono estremamente grata per l'affetto che ci unisce e so di poter contare su di lei, come lei su di me. Le nostre interminabili telefonate sono state il balsamo che ha alleviato la mia solitudine. Grazie di cuore a Martina e alle nostre colazioni virtuali in quarantena. Nonostante la conosca da una vita riesce sempre a sorprendermi e a farmi mettere in discussione. Il suo spirito genuino, la sua allegria e il suo grande cuore sono la ricetta infallibile per il buonumore. Grazie anche a Francesca, per essermi stata vicina e per il suo appoggio e incoraggiamento. La ammiro per la sua forza, la sua resilienza e la sua capacitá di rimettersi sempre in gioco, e sono grata di poter fare affidamento sulla sua amicizia. E come dimenticare i miei cari "papiri", Elena, Luca, Camilla, Luca (DM), Francesco (Coach), Stefano, Eugenio (dove sarà Eugenio?), Francesco, Andrea e Enrico. I nostri ritrovi bisettimanali su meet e la loro compagnia mi hanno aiutato a scandire il passaggio del tempo e sono stati un dono prezioso in questi tempi stranianti che stiamo vivendo. Infine, grazie ad Alberto, Francis e a tutti gli altri amici che mi sono stati accanto in questo tempo di scrittura e nel percorso che mi ha portato fin qui.

Siviglia "tiene un color especial", come dicono qui, e mi ha incantata con la sua bellezza, i suoi sgargianti colori e la sua gente. Ma anche in un posto cosí accogliente e meraviglioso è inevitabile sentire, di tanto in tanto, nostalgia. Per questo ringrazio di cuore la mia piccola comunità di donne italiane a Siviglia, Cristina, Laura e Ilaria, con le quali ho potuto esprimere e condividere la mia italianitá e dalle quali mi sono sentita capita.

Durante mis años en Sevilla he tenido la suerte de cruzarme con personas maravillosas, que me han acogido con los brazos abiertos y cuya presencia me ha enriquecido. Gracias ante todo a los "mongolfiera", en especial Jorge, Mario, Cristina, Andrés, Mercedes, Carlos, Laura, Miguel, y Carlos, por ayudarme a emprender los primeros pasos en el camino del doctorado y hacerme sentir arropada. No bastan las palabras para expresar la gratitud que siento hacia mis compañeros del "despachito", Damián, Tere y Llanlle. Su llegada marcó un giro tanto en mi formación doctoral como en mi vida. Con ellos he compartido fracasos y logros, llantos y alegrías, momentos serios e incontables tonterías. Echaré muchísimo de menos nuestros momentos de complicidad en el despacho, aunque sé que seguirán estando a mi lado allá donde yo vaya. En especial, quiero agradecer a Damián todo el tiempo que me

ha dedicado y la enorme ayuda que me ha proporcionado en el desarrollo de mi tesis. Su apoyo y sus palabras me han sostenido en los momentos difíciles, haciéndome creer en mí misma.

Un gracias de todo corazón va a las personas que han compartido piso conmigo en estos años, convirtiendose en mi familia. A Elena, a mi adorable perrita Lana y a Bea, por su amistad y por hacerme descubrir Sevilla y a su gente. A mi querida luchadora Alessandra y a la dulcísima Jila, por haber dejado una huella en mi corazón. A Ibon, porque es el mejor amigo que podría desear y mi punto de referencia. Siempre ha estado presente para escucharme, animarme y darme todo su apoyo. Su amistad es un puerto seguro y una flor que deseo cultivar para toda mi vida. A Agata y a Rocío, por haberme acompañado en la última etapa de mi tesis doctoral, con lo que eso ha conllevado. Especialmente, quiero agradecer a Rocío la paciencia y la comprensión demostradas por mi creciente dejadez en las labores domésticas. Pero, sobre todo, le estoy inmensamente agradecida por su amistad, su complicidad y su capacidad de alegrarme siempre el día. Finalmente, gracias a Alex, mi futuro "compañero de piso" y el más inesperado de los regalos en este 2020 tan extraño. Su cariño y su apoyo me han dado la carga y el entusiasmo para acabar este trabajo y empezar una nueva aventura.

Un agradecimiento y un recuerdo especial van a Morgan, Boris y a toda la familia del CrossFit Macarena Box. No sé qué habría hecho sin ellos y sin las agotadoras sesiones de entrenamiento en cuarentena. Me han animado a ser tenaz, constante y a sobrepasar mis limites. Gracias a ellos he descubierto que soy más fuerte de lo que pensaba y que todo se puede consiguir con aplicación y esfuerzo. Los entrenamientos en el Macarena Box han sido, y son, mi momento desahogo y mi medicina; una ayuda valiosísima para mantenerme centrada y aclarar mi mente.

Gracias de todo corazón a mio tío Ángel, a mi tía Paqui y a mis primas Alicia y María. Su cercanía y su afecto me han hecho sentir menos sola y han sido mi hogar de referencia en estos años lejos de casa. Finalmente, no habría llegado donde estoy hoy sin mi familia y su incondicional apoyo. Mi madre, mi padre y mi hermano Silvio son el faro que me guía cuando estoy a la deriva y el hogar en el que me siento segura. Gracias a mi madre, mi modelo a seguir y la mujer que más admiro. Aunque ambas suframos por la distancia que nos separa, le estaré siempre agradecida por las alas que me ha dado y por velar mi vuelo. Gracias a mi padre, por su sabiduría y su don para tranquilizarme y transmitirme serenidad. Sé que puedo confiar en él en todo momento y conservo como un tesoro todos sus consejos. Y gracias a Silvio, la chispa de la casa. Cada día estoy más orgullosa del hombre en el que se está convirtiendo y de la determinación con la que prosigue su camino. Le agradezco su incansable y contagioso entusiasmo, que es la pimienta que da sabor a nuestro día a día.

Abstract

Cancer is one of the leading causes of mortality world-wide, killing more than one million people per year just in Europe. Nowadays, proton therapy is one of the most promising techniques in the fight against cancer, being two the main bases of its success: (1) the physical advantages of protons with respect to conventional radiotherapy with photons, resulting in a more selective energy deposition in depth; (2) the increased biological effectiveness of protons with respect to photons and their denser pattern of energy deposition in matter, usually determining a more lethal damage to the DNA. The biological effect of protons and other ions with respect to photons is described in terms of the Relative Biological Effectiveness (RBE), i.e., the ratio between the doses of the reference and studied radiation determining the same effect. In clinical proton therapy, a RBE value of 1.1 is currently used. However, there is an increasing awareness that proton RBE is not a constant, but seems to increase linearly with the Linear Energy Transfer (L_{D}) of the proton as it slows down in tissues, especially close to the distal region of the Bragg peak, possibly leading to toxicity in healthy tissue beyond the target. In this context, recent studies aim at including dose-averaged LET objective functions in treatment planning optimization to take full advantage of the increased RBE in protons beams. This last problem, and the characterisation of RBE, can be addressed with the formalism of microdosimetry, which, on one hand, permits the calculation of RBE from a microscopic approach by means of the microdosimetric kinetic model (MKM) and, on the other hand, provides physical concepts and computational tools to calculate macroscopic L_{D} distributions.

The rationale behind this thesis project is, therefore, given by the necessity of performing studies of proton RBE at low energies, close to the Bragg peak region of clinical proton beams (below 40 MeV), which would help reaching a consensus on the variation of proton RBE with LET. To do so, two main objectives were foreseen: (1) the design and mounting of a low energy proton facility at CNA (proton kinetic energy below 18 MeV) for the experimental study of RBE in mono-layer cell cultures and (2) the development of a simulation tool to study the patterns of energy deposition of protons in water at a micrometric scale, for the computation of microdosimetric quantities.

This thesis is divided in four chapters. In Chapter 1, the physics foundations of proton therapy are presented, followed by a description of the relevant biological parameters. In this context, special attention is given to the formalisms of microdosimetry and its most relevant quantities. Then, an insight into Monte Carlo simulations and the main codes used in this work is presented, together with a description of the radiation dosimeters employed for the experimental measurements performed.

Chapter 2 is dedicated to the description of the radiobiology beam line designed and mounted at the 18 MeV proton cyclotron facility installed at the National Centre of Accelerators (CNA, Seville, Spain), focusing especially on the overall optimization of the beam parameters to define the best setup for the irradiation of mono-layer cell cultures. In this chapter, a Monte Carlo simulation of the beam line, realised with Geant4 and validated towards experimental measurements, is also presented.

In Chapter 3 a Monte Carlo track structure application, which was developed for the computation of microdosimetric distributions of protons in liquid water, is described. This application, based on Geant4-DNA, provides two sampling methods, uniform and weighted, for the scoring of the quantities of interest in spherical sites. Furthermore, it is used to verify the validity range of a formula that links microdosimetric quantities to the macroscopic dose-averaged LET distribution, being a powerful tool for the development of analytical models to be used in treatment planning optimisation.

Chapter 4 presents the results of the first irradiation of cell cultures at the radiobiology beam line developed at the cyclotron facility. In this context, an application of the Monte Carlo code for the computation of microdosimetric quantities is shown. With this code, a theoretical derivation of the expected RBE for the experimental irradiation and cells under study could be done, through the use of the microdosimetric kinetic model.

Finally, a summary of the results obtained and a brief discussion on the future perspectives of this project conclude this work.

Contents

Chapter 1

Principles of Proton Therapy

1.1 Introduction

According to the estimates of the World Health Organization (WHO), cancer is among the top two leading causes of premature death in most countries with a high Human Development Index (HDI), and its incidence is expected to increase by about 70% over the next two decades [1]. Depending on the type of malignancy, location, stage of the disease and general state of the patient, different treatment options exist, surgery, chemotherapy and radiotherapy being the most common ones. If the tumour is operable, surgery is the preferable option as it directly removes all the cancerous tissue. Chemotherapy, on the other hand, is a pharmaceutical systemic treatment targeting rapidly-growing cells, such as cancer ones, in the whole body. For this reason, chemotherapy is an aggressive treatment for patients, as it also affects normal cells causing important side effects. Finally, radiotherapy is a localised treatment that uses ionising radiation to injure or destroy cancer cells. Radiotherapy plays an important role in cancer management, as about 70% of all patients diagnosed with cancer receive curative or palliative radiation treatments, most of the time performed with photon or electron beams [2]. Combined therapy modalities can also be applied: chemo-radiotherapy, for example, can be used to treat metastatic tumours, while radio-surgery applications are mainly adopted to shrink the tumour volume before irradiation or to reduce relapse probability after operation.

Thanks to the development of high-precision treatments and imaging techniques, the number of patients effectively treated with radiotherapy increased in the last decades, meaning that the improvement of this treatment modality may impact significantly on the global outcome of cancer treatment [3, 4]. At present, the Intensity Modulated Radiation Therapy (IMRT) is one of the cutting edge technologies in traditional radiotherapy with X-rays [5, 6]. IMRT is an advanced technique of high-precision radiotherapy that allows to conform the radiation dose more precisely to the three-

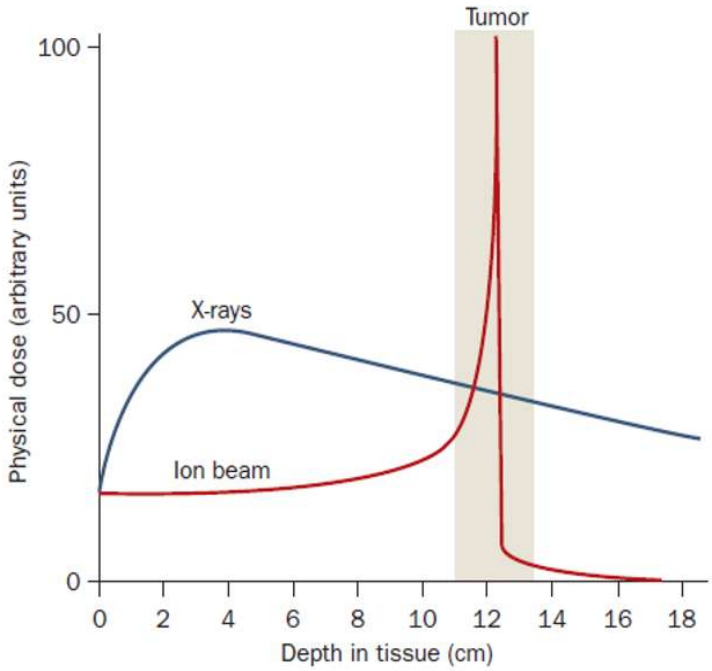

Figure 1.1: Comparison of the profiles of energy deposition in water as a function of depth (Physical dose) of an X-ray beam and high-energy charged particles. While an X-ray beam exhibits an exponential decrease of energy deposition at depths greater than few cm (approximately 1.5 cm for a 6 MV clinical beam), charged particles deposit most of their energy at the end of their path, defining a region usually called Bragg peak, while sparing both proximal and distal located normal tissues (taken from [11]).

dimensional shape of the tumour, by modulating the intensity of the radiation beam. Typically, multiple fields coming from different directions are combined to deliver a patient specific radiation dose: maximised in the tumour and minimised in the adjacent normal tissues [7]. However, since the aim of any treatment modality is to kill as many cancerous cells as possible, while minimising damage to the healthy-tissues, in some situations conventional radiotherapy is not sufficient due to the tumour location close to organs at risks, that sometimes results in the delivery of a radiation dose above their tolerance. The urge for clinical solutions to treat these cases has stimulated in the last twenty years both remarkable technological developments in conventional photon therapy and an increasing enthusiasm in the use of particle beams for radiation therapy, which could not be fully exploited before the achievement of these advances [8].

The article in *Radiology* [9], published by Robert Wilson in 1946 about the therapeutic interest of protons for treating cancer, is usually considered as the starting point of

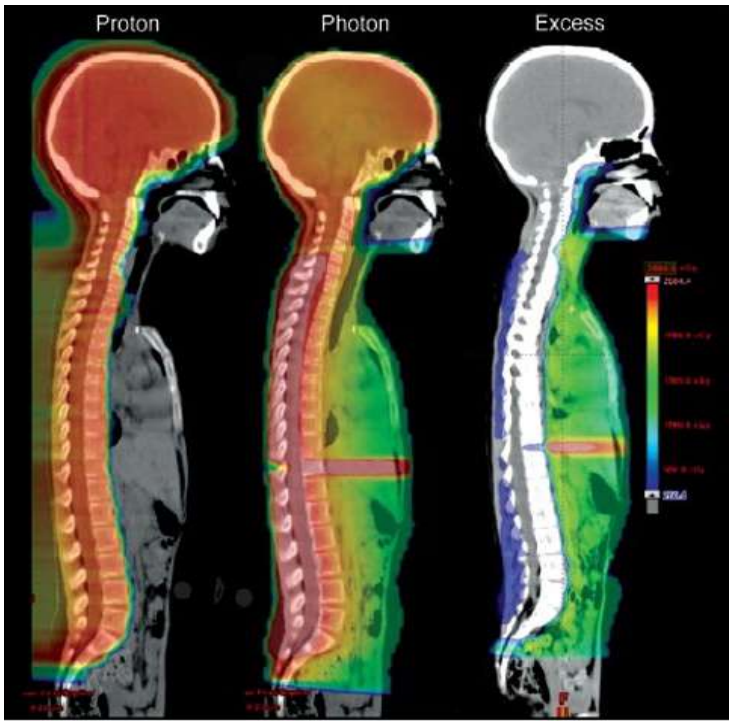

Figure 1.2: Comparison of saggital images of proton and photon treatment plans for a pediatric patient treated with craniospinal radiation. On the right, the excess dose deposited from photon treatment is highlighted (taken from [12]).

particle therapy: less than ten years later, in 1954, the first treatments with protons took place in the Lawrence Berkeley Laboratory (Berkeley, CA, USA). Today, particle therapy has grown into an advanced clinical modality, counting more than 100 000 patients treated worldwide with protons since the establishment in 1990 of the first hospital-based treatment centre in Loma Linda (California, USA) and more than 10 000 treated with heavier ions, generally carbon [10].

The clinical interest in particle therapy comes from the favourable physical properties of charged particles, especially their characteristic curve of energy deposition in depth, which allows precise delivery of radiotherapy treatments. As emerges from Figure 1.1, while an X-ray beam deposits energy slowly and mainly exponentially as it penetrates tissue, the energy deposition of charged particles increases with penetration depth, reaches a maximum just before coming at rest in the region called the Bragg peak and then exhibits a rapid fall-off. Since the Bragg peak position in depth increases with the kinetic energy of the incident particle, it is possible to target a well-defined region at a certain depth in the body, tuning the position of the Bragg peak by adjusting the energy of the incident particle beam, while sparing

both proximal and deeper located normal tissues, as shown in Figure 1.2.

As already mentioned, tumour indications for particle therapy are generally those close to organs at risk, being chordomas and chondrosarcomas of the base of the skull and eye tumours some typical cases [13]. However, other indications exist, for example for patients where the reduction of the radiation dose received by normal tissues is essential: children treated with curative intent and patients with genetic, radiosensitive syndromes [13]. More generally, the high-precision and non-invasiveness of the Bragg peak would be beneficial for most cancer cases. However, in some situations the clinical benefit is not significant enough, while substantial differences in cost exist between X-ray-based therapy and particle therapy, being the latter more expensive both in terms of initial investment and cost per treatment, making the issue of cost-benefit ratio highly controversial [14].

In addition to the physical advantages derived from the energy loss mechanism that characterises the interaction of protons and other ions with matter, the use of particle therapy is associated with important biological advantages, which can be exploited in the clinics. The biological properties of any type of radiation are derived from the energy deposition pattern: if compared to photons, charged particles (especially light ions) exhibit a more condensed ionisation pattern in traversed cells, resulting in the induction of more complex damages and different cellular responses, which can be exploited in particle therapy. This is usually quantified by the *Relative Biological Effectiveness* (RBE), defined for a given radiation type as the ratio between a reference radiation dose (generally ^{60}Co, γ-rays or 250 keV X-rays) and the dose of the radiation type considered that produces the same biological effect. While for heavy ions like carbon the increase in RBE is clearly advantageous for treatments, the case of protons is not fully understood and a lot of uncertainties exist both in experimental measurements and models of proton RBE [16]. In clinical practice with protons, a fixed RBE value of 1.1 is used [15], despite the evidences suggesting that the RBE changes along the Bragg curve, but that is justified by the fact that the available biological data are insufficient to support the implementation of other proposed RBE models in clinical environment [17–22].
The work presented in this thesis is inserted into this context and has two main objectives: (1) the design and mounting of a low energy proton facility (proton kinetic energy below 18 MeV) for the experimental study of RBE in mono-layer cell cultures, as described in Chapter 2; and (2) the development of a simulation tool to study the patterns of energy deposition events of protons in water at a micrometric level, useful to infer the biological effects of protons at a macroscopic scale through specific models as described in Chapters 3 and 4.

In the following sections, the physics fundamentals and the radiobiological bases of

proton therapy will be described in details; followed by a brief overview about Monte Carlo methods and radiation detectors for dosimetry in particle therapy.

1.2 Physical aspects

The phenomena associated with the interaction of ionising radiation with matter include a wide variety of physical mechanisms, whose knowledge is of fundamental importance to allow the widespread of new techniques and applications. Radiation interacts with matter in terms of its fundamental elements: atoms, nuclei and their individual constituents, with a probability that is governed by quantum mechanics and depends on radiation nature, energy and type of material. The type of processes occurring for each type of radiation define its propagation through matter, its detection characteristics as well as its effects on biological organisms. The most common processes which take place when charged particles or photons pass through matter are governed by electromagnetic interactions. Light ions undergo energy losses mainly due to excitation and ionisation of the atoms of the medium close to their trajectory. Electrons and positrons also lose energy by radiating photons. Finally, photons are attenuated in matter by single scattering with atomic electrons of the medium or by a few subsequent interactions mainly governed by Compton scattering, photoelectric effect and pair production, the last two eventually leading to full absorption of the photon in matter [23].

In this section, the physical principles of the interaction of protons with matter, relevant to therapeutic applications, are discussed. Two are the main processes that characterise the passage of these particles through a material: energy loss and deflection from the particle original direction. Protons interact with matter primarily through Coulomb forces between their positive charge and the negative charge of the electrons of the absorber atoms. Depending on the closeness of such interactions, the impulse felt by the electrons from the attractive Coulomb force may be sufficient either to raise the electron to a higher-lying shell within the atom (excitation) or to remove it completely from the atom (ionisation) [26], subsequently causing new ionisations as the freed electron travels and interacts with other neighbouring atoms. In the slowing down process, most protons travel in a nearly straight line and no significant deflections of their trajectory are observed, as their rest mass is approximately 2000 times greater than that of an electron. In contrast, a proton passing close to the atomic nucleus of the absorber, whose mass is much bigger, experiences a repulsive elastic Coulomb interaction, that deflects the proton from its original trajectory. Although such interactions occur rarely, when they take place the target nucleus absorbs a very little amount of energy while the incident particle is scattered, causing a deflection of its trajectory. For example, for a 1 MeV proton

impinging on a carbon nucleus, the maximum scattering angle is approximately 5° with an interaction probability of only about 0.1% that decreases with increasing energy. Therefore, elastic nuclear interactions only play a small role towards the very end of the proton path [24].

In the following, the two main processes of proton interaction with matter, which can be generally identified as *stopping* and *scattering*, will be discussed in detail.
A third type of process contributes to determine the shape of the Bragg peak: the nuclear interaction of proton projectiles with the target nuclei. This type of interaction leads to the excitation of the target nucleus, to the formation of a compound nucleus or to a direct interaction with an individual component of the nucleus. The result is an energy loss of many MeV per collision, eventually accompanied by the emission of secondary particles and by a significant change in the flight direction of the proton. The probability for non-elastic nuclear reactions increases rapidly with increasing proton energy being about 1% for a 25 MeV proton and up to 25% for a 200 MeV proton [24, 25]. However, since for the energies considered for the purpose of this thesis (below 18 MeV) head-on collisions of protons with nuclei are very rare, their contribution will be neglected.

1.2.1 The stopping power and the Bragg peak

As previously mentioned, the energy loss of protons in matter is mostly described by their electromagnetic collisions with the target electrons, which are statistical in nature. The amount of energy transferred after each collision is a very small fraction of the kinetic energy of the incident particle. However, depending on the density of the material traversed by the protons, the number of interactions per unit of length might be very large. It is then possible to define an average energy loss per unit path length, the so-called *stopping power* $\mathrm{d}E/\mathrm{d}x$, where $\mathrm{d}E$ is the mean energy loss and $\mathrm{d}x$ is the distance traversed by the particle in the medium. The energy loss rate is described by the Bethe [27] and Bloch [28] formula reported here in the relativistic version described by Fano [29]:

$$-\frac{\mathrm{d}E}{\mathrm{d}x} = 4\pi N_\mathrm{A} r_\mathrm{e}^2 m_\mathrm{e} c^2 \rho \frac{Z_\mathrm{t}}{A}\frac{Z_\mathrm{p}^2}{\beta^2}\left[\ln\frac{2m_\mathrm{e}c^2\gamma^2\beta^2}{\langle I\rangle} - \beta^2 - \frac{C}{Z_\mathrm{t}} - \frac{\delta}{2}\right], \qquad (1.1)$$

where N_A is Avogadro's number, r_e, m_e and e are the electron classical radius, mass and charge, Z_t and Z_p denote the atomic numbers of the target and the projectile, A is the atomic weight of the target material and ρ its mass density, $\beta = v/c$, where v is the particle velocity and c is the speed of light, $\gamma = (1-\beta^2)^{-1/2}$, and $\langle I\rangle$ is the mean excitation potential of the target material. The terms C and δ are two correction factors which are derived from relativistic theory and quantum

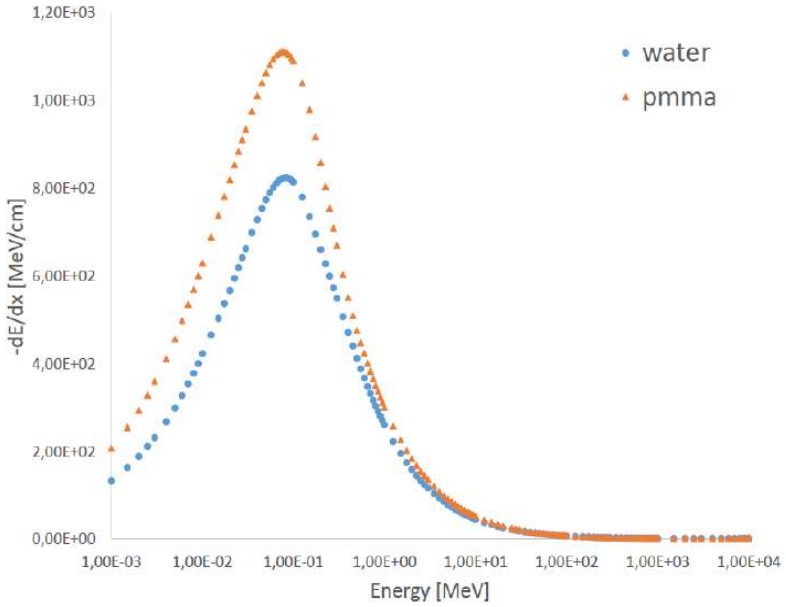

Figure 1.3: Variation of $-\mathrm{d}E/\mathrm{d}x$ as a function of the proton kinetic energy in water (blue circles) and in Polymethyl methacrylate (PMMA, $\rho = 1.19\,\mathrm{g\,cm^{-3}}$, orange triangles). Data extracted from the National Institute of Standard and Technologies (NIST, Maryland, MD, USA) Standard Reference Database PSTAR [31].

mechanics, and need to be considered respectively when projectiles at very low (below few MeV for protons [23]) or very high energy (close to 1 GeV for protons in biological materials [30]) are used in calculations. The shell correction C arises as the incident particle velocity gets closer to the velocity of atomic electrons. In this energy region, many complex phenomena take place, the most important of them being the electronic capture by the incident particle, that determines a decrease of its charge state and consequently of its stopping power. The density effect δ, instead, originates from the electric field produced by the incident particle, which tends to polarise the electrons of the medium along its path. This effect increases with the particle energy, meaning that further electrons feel a shielded electric field and give a lower contribution to the energy loss.

At high velocities the atomic electrons are completely stripped off and the projectile charge is equal to the atomic charge Z_p. At lower velocity, below about $10\,\mathrm{MeV\,u^{-1}}$ for light ions, the mean charge state decreases due to the interplay of ionisation and recombination (electron exchange) processes. To account for this phenomenon, Barkas [32] proposed to replace Z_p by a projectile effective charge Z_eff, parametrised as a function of β and Z_p of the incident particle with the following empirical formula:

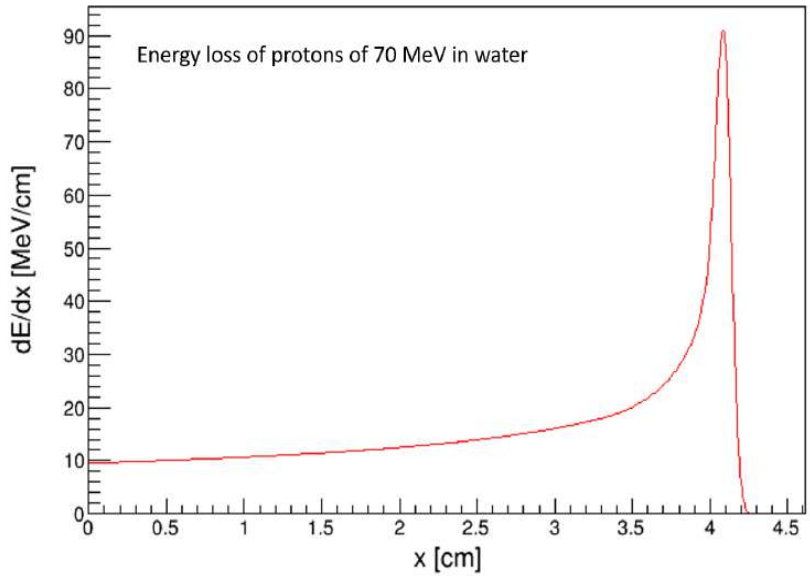

Figure 1.4: A typical Bragg curve, showing the variation of $-\mathrm{d}E/\mathrm{d}x$ as a function of the penetration depth for protons having a kinetic energy of 70 MeV in water. Computed with the Monte Carlo code Geant4 (see Section 1.4).

$$Z_{\mathrm{eff}} = Z_{\mathrm{p}} \left[1 - \exp\left(-125 \beta Z_{\mathrm{p}}^{-2/3} \right) \right]. \tag{1.2}$$

Some interesting considerations can be done by observing the dependences of the energy loss on the projectile and material characteristics in Equation (1.1). Indeed, $\mathrm{d}E/\mathrm{d}x$ is proportional to the inverse square of the velocity of the incident particle and on the square of its charge, and there is no dependence on the projectile mass. On the other side, Equation (1.1) puts in evidence the strong influence of the target material on the energy loss rate. In fact, the stopping power is proportional to the electron density $N_{\mathrm{A}}\rho Z_{\mathrm{t}}/A$ of the target material, and depends on its $\langle I \rangle$ value, which varies from about 19 eV for hydrogen to about 820 eV for lead, being 78 eV the one of water [33]. However, since this last dependence goes with the logarithm of $\langle I \rangle^{-1}$, its effect is diminished, and the strongest elements affecting the energy loss in the human body are the material density, which can vary by about three orders of magnitude from air in the lung to cortical bone, and the particle velocity, which can cause the stopping power in water to vary by a factor of 60 for proton energies between 1 and 250 MeV [34] (see Figure 1.3).

Taking into account the aforementioned considerations, as a light ion slows down inside matter, its rate of energy loss changes, determining a greater amount of energy deposited per unit length at the end of its path rather than at its beginning. This

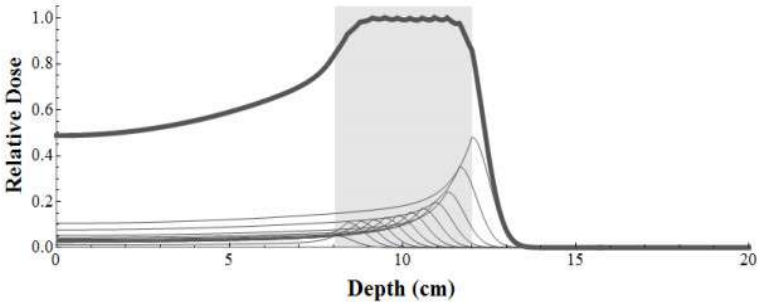

Figure 1.5: Example of the method of summing up different Bragg peaks with different energies and weights, to build the SOBP (taken from [35]).

effect is shown in Figure 1.4, which represents the amount of energy deposited by a proton as a function of its position along its slowing-down path. The curve is known as *Bragg curve* and its maximum is usually indicated as *Bragg peak*. In the clinical practice, the aim is usually to obtain an irradiation profile broader than the individual Bragg peak, in order to achieve a better coverage of the tumour volume. This is done by superimposing different beams with slightly different energies and fluence weights, as depicted in Figure 1.5, generating a *spread out Bragg peak* (SOBP) that deposits the required radiation dose in the treatment volume.

Until now, proton energy loss has been described in an approximate way on the assumptions that a proton loses energy along a linear trajectory and that the energy loss is continuous. However, the absorption of this energy occurs in a three-dimensional volume, and the random fluctuations in the location and size of primary ionisation events result in a proton ionisation track with an irregular three-dimensional structure. Indeed, some of the recoil electrons produced by the proton interaction, usually defined as δ-rays, are sufficiently energetic to create small spur tracks of ionisation emanating from the main track. The maximum possible energy transfer to a δ-ray ($E^{\delta}_{\max}$) following the collision of a proton with an unbound stationary electron is:

$$E^{\delta}_{\max} = 2m_{\mathrm{e}}c^2\beta^2\gamma^2\left[1 + 2\gamma\frac{m_{\mathrm{e}}}{M} + \left(\frac{m_{\mathrm{e}}}{M}\right)^2\right]^{-1}, \tag{1.3}$$

where M is the mass of proton. Even for very energetic protons, the secondary electrons do not acquire enough energy to travel more than a few millimetres from the proton track; for example, a 250 MeV proton can transfer to an electron a maximum energy of ~ 600 keV resulting in a maximum travelled distance from the proton track in water of about 2 mm. For targets having atomic numbers ranging between $Z_{\mathrm{t}} = 6$ and $Z_{\mathrm{t}} = 92$ in the δ-ray energy range 0.7 keV − 30 MeV, the

maximum distance travelled by secondary electrons ($R^{\delta}_{\max}$) can be calculated by a semi-empirical equation developed by Tabata et al. [36]:

$$R^{\delta}_{\max} = a_1 \left[\frac{1}{a_2} \ln\left(1 + a_2 \frac{E^{\delta}_{\max}}{m_e c^2}\right) - \frac{a_3 \frac{E^{\delta}_{\max}}{m_e c^2}}{1 + a_4 \left(\frac{E^{\delta}_{\max}}{m_e c^2}\right)^{a_5}} \right], \tag{1.4}$$

where the parameters a_i are given by simple functions of the atomic number Z_t and the mass number A of the target material. The expressions for the parameters a_i are listed here:

$$\begin{aligned} a_1 &= b_1 A / Z_t^{b_2}, \\ a_2 &= b_3 Z_t, \\ a_3 &= b_4 - b_5 Z_t, \\ a_4 &= b_6 - b_7 Z_t, \\ a_5 &= b_8 / Z_t^{b_9}, \end{aligned} \tag{1.5}$$

where the symbols b_i are constants, independent on the target material, which have been determined by Tabata et al. [36] and whose values are listed in Table 1.1.

Table 1.1: Values of the constants $b_i (i = 1, 2, ..., 9)$ of Equation (1.5). Reprinted from [36]

i	b_i
1	0.2335
2	1.209
3	1.78×10^{-4}
4	0.9891
5	3.01×10^{-4}
6	1.468
7	1.180×10^{-2}
8	1.232
9	0.109

If Equation (1.4) is applied to materials that are mixtures or compounds, the atomic and mass number should be replaced by respective effective values (Z^*_t and A^*):

$$Z_{\mathrm{t}}^{*} = \sum_{i} f_i Z_i, \tag{1.6}$$
$$A^{*} = Z_{\mathrm{t}}^{*} \left(\sum_{i} f_i \frac{Z_i}{A_i} \right)^{-1},$$

where f_i is the fraction by weight of the constituent elements with atomic number Z_i and atomic weight A_i. For a water medium, for example, $Z_{\mathrm{t}}^{*} = 7.22$ and $A^{*} = 13.0$. The spatial characteristics of secondary electrons should, in principle, be taken into account near material interfaces and in cases where the radiation quality is of interest, as it happens in the microdosimetric characterisation of individual energy deposition events, which will be described in Section 1.3.3.

1.2.2 Range and energy straggling

The peculiar shape of the stopping power distribution as a function of the material penetration depth has led to the conception, and later on the development, of proton therapy as a technique in cancer research and therapy. Indeed, a key aspect of proton therapy is the precise knowledge of the beam *range*, a distance beyond which no primary particle will penetrate. Assuming the energy loss to be continuous, this distance should be a well defined magnitude, the same for all identical particles with the same initial energy in the same medium. However, as shown in Figure 1.6, this is not necessarily true as the incident protons stop within a certain interval of thicknesses. This behaviour, known as *range straggling*, is due to the fact that the energy loss has a statistical nature, which leads to an approximately Gaussian distribution of the range. Consequently, the *range* is an average quantity, defined for a beam and not for individual particles.

Since the path of most protons in matter is nearly a straight line, on average their true path length is approximately equal to their projected path length and range. This fact makes many proton range calculations resolvable with relatively simple numerical or analytical approaches. Bearing in mind the previous considerations and under the hypothesis of Continuous Slowing Down Approximation (CSDA), from a theoretical point of view the range $R(E_0)$ of an incident particle with energy E_0 can be calculated integrating the Bethe and Bloch formula as follows:

$$R(E_0) = \int_0^R \mathrm{d}x(E) = \int_{E_0}^0 \frac{\mathrm{d}x}{\mathrm{d}E}\,\mathrm{d}E = \int_{E_0}^0 \left(\frac{\mathrm{d}E}{\mathrm{d}x}\right)^{-1} \mathrm{d}E. \tag{1.7}$$

For any given particle, however, the path-length or equivalently the amount of energy loss per unit path length will not generally be equal to its mean value, due to the

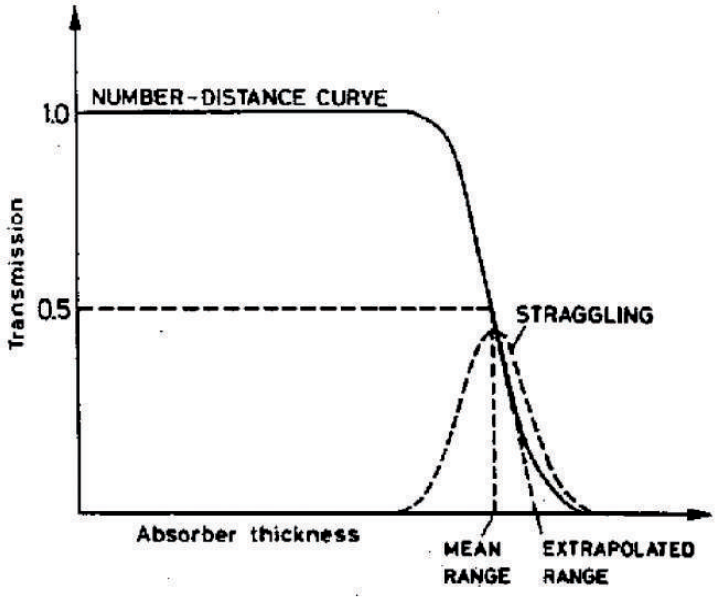

Figure 1.6: Experimentally, the range can be determined by measuring the ratio of transmitted to incident particles (I/I_0), coming from a mono-energetic and collimated beam impinging on different thicknesses of the same material. The distribution of ranges is approximately Gaussian in form. The mean and extrapolated ranges are highlighted (taken from [37]). A typical curve, depicted in , shows this ratio as a function of the absorber thickness.

statistical fluctuations in the number of collisions and in the energy transferred, resulting in a broadening of the Bragg peak. These fluctuations in energy lost, or *energy straggling*, are described by the asymmetric Vavilov distribution [38], which is characterised by a long tail deriving from the non zero probability of having large energy transfers in a single collision. For relatively thick absorbers, in the limit of many collisions, the Vavilov energy loss distribution becomes a Gaussian [39, 40]:

$$f(\Delta E) = \frac{1}{\sqrt{2\pi}\sigma_{\mathrm{E}}} \exp\left[-\frac{\left(\Delta E - \overline{\Delta E}\right)^2}{2\sigma_{\mathrm{E}}^2}\right], \tag{1.8}$$

where ΔE is the energy lost, $\overline{\Delta E}$ is the mean energy loss and σ_{E}^2 is the variance, which is proportional to the thickness of traversed material. Since, in principle, range straggling imposes a limit on the accuracy with which the particle energy can be determined from its range [41], the variance σ_{R}^2 of the range distribution is related to the variance σ_{E}^2 of the energy loss straggling distribution:

$$\sigma_{\mathrm{R}}^2 = \int_0^{E_0} \left(\frac{\mathrm{d}\sigma_{\mathrm{E}}}{\mathrm{d}x}\right) \left(\frac{\mathrm{d}E}{\mathrm{d}x}\right)^{-3} \mathrm{d}E, \tag{1.9}$$

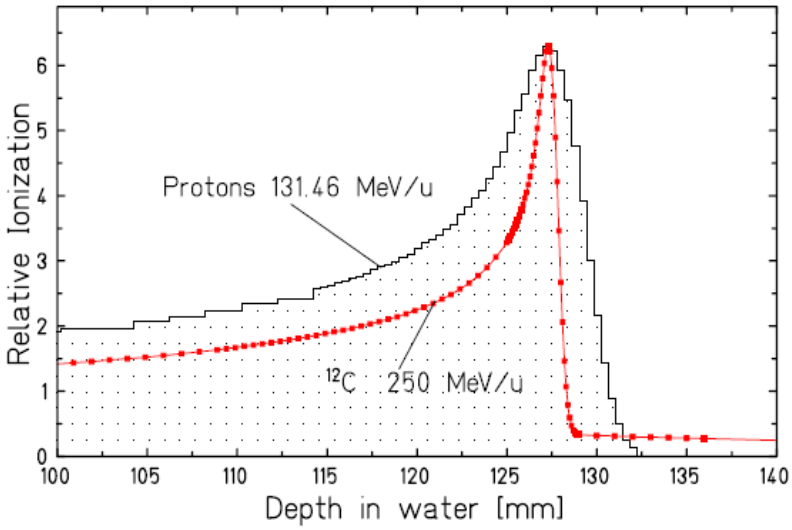

Figure 1.7: Experimental depth dose curves of protons and ^{12}C ions having the same mean range in water (taken from [42]). Due to the higher relative range straggling experienced by protons, the width of their Bragg peak is enlarged with respect to the carbon ions distribution.

where E_0 is the particle initial energy.

The relative range straggling of a particle of energy E and mass M is nearly constant and can be described by [42]:

$$\frac{\sigma_{\mathrm{R}}}{R} = \frac{1}{\sqrt{M}} \cdot f \cdot \left(\frac{E}{Mc^2} \right), \tag{1.10}$$

where f is a slowly varying function depending on the target material [43]. Equation (1.10) means that the relative straggling is smaller for heavier particles: by comparing Bragg peaks of protons and carbon ions having the same mean range in water, as illustrated in Figure 1.7, it can be observed that the peak for a carbon ion beam is much narrower than for a proton one.

1.2.3 Lateral beam spread

While the depth of the Bragg peak depends on the particle initial energy, its width is modulated by the energy dispersion in both the longitudinal and the transverse directions. The first is due to the energy straggling, as described in Section 1.2.2, while the second is mainly due to the elastic Coulomb collisions experienced by the primary particles when impinging on the target nuclei. In the treatment of Coulomb scattering, three main regions can be distinguished [37]:

1. *Single scattering* occurring for very thin absorbers where the probability of more than one Coulomb scattering is small. In this case, the angular distribution is given by the Rutherford formula [44], valid in the classical limit for point-like projectiles and targets.

2. *Plural scattering* occurring if the average number N of independent scattering events is $N < 20$. This case is difficult to treat since neither Rutherford formula nor statistical methods can be applied.

3. *Multiple scattering* occurring for $N > 20$. If the energy loss is small or negligible, the problem can be treated statistically to obtain the probability distribution for the net deflection angle as a function of the thickness of crossed material. This is what is generally known as *Multiple Coulomb Scattering*.

In clinical proton therapy, most targets considered are thick enough to produce a large number of scattering events, and multiple Coulomb scattering plays a major role. A rigorous calculation of multiple Coulomb scattering is extremely complicated and the most elegant and comprehensive theory for incident protons is that of Molière, which is generally valid for all particles up to angles of $\theta \simeq 30°$ [37]. In the formulation by Molière, the polar angle distribution is expressed as a power series. If the target thickness is big enough, in the first approximation, the greater order terms of this series may be excluded, and the angular distribution function is approximately Gaussian in form:

$$P(\theta)\,\mathrm{d}\Omega \simeq \frac{2\theta}{\langle\theta^2\rangle}\exp\left(\frac{-\theta^2}{\langle\theta^2\rangle}\right)\mathrm{d}\theta, \tag{1.11}$$

where the parameter $\langle\theta^2\rangle$ represents the variance of the scattering angle distribution. A better estimation of this quantity, however, is obtained using the empirical formula proposed by Highland [45], which is valid for target atomic numbers $Z_\mathrm{t} > 20$ and for target thicknesses $10^{-3} \times L_\mathrm{rad} < d < 10 \times L_\mathrm{rad}$:

$$\sigma_\theta = \frac{14.1\,\mathrm{MeV}}{p\beta c} Z_\mathrm{t}\sqrt{\frac{d}{L_\mathrm{rad}}}\left(1 + \frac{1}{9}\log_{10}\frac{d}{L_\mathrm{rad}}\right). \tag{1.12}$$

In the previous formula, L_rad is the material radiation length, d is the material thickness, p is the particle momentum and σ_θ is the variance of the scattering angle distribution expressed in radians. Equation (1.12) tells us that, independently of their mass, particles with the same kinetic energy, which can be derived from $p\beta c$, undergo the same deflection. At the same time, the term $p\beta c$ in the denominator, influences the behaviour of the lateral spread, which grows inversely with the energy.

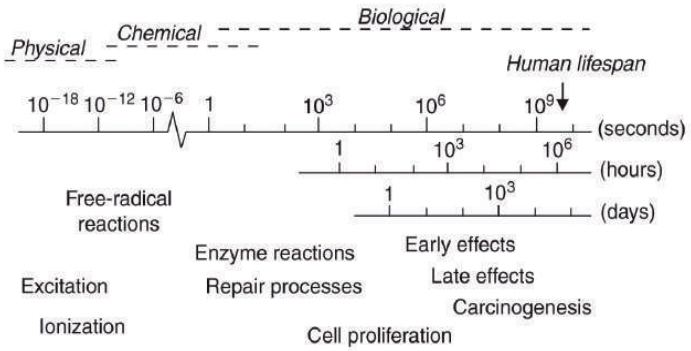

Figure 1.8: Time-scale of the effects of radiation exposure on biological systems (taken from [46]).

1.3 Radiobiological aspects

When dealing with the biological effect of any radiation type on living cells and tissues, several differences to the action on non-living material must be taken into account, the first being the capability of living cells to actively process the damage induced by radiation. This damage processing takes time, implying a strong time dependence of biological effects, which spans a scale from minutes to years. Indeed, the irradiation of any biological system generates a succession of processes that differ enormously in time scale [46], as it is illustrated in Figure 1.8.
These processes can be divided into three phases: *physical*, *chemical* and *biological*, each of them having a characteristic time span.

- **Physical Phase**

  During the physical phase, radiation interacts with the atoms and molecules composing the tissue. A high-speed electron, for example, takes about 10^{-18} s to traverse the DNA molecule and about 10^{-14} s to pass across a mammalian cell, inducing ionisation or excitation of the atoms.

- **Chemical Phase**

  The chemical phase describes the period in which damaged atoms and molecules react with other cellular components in rapid chemical reactions. Ionisation and excitation lead to the formation of highly reactive molecules known as *free radicals*.

- **Biological Phase**

  The biological phase includes all subsequent processes; the vast majority of lesions are successfully repaired, while some rare lesions fail to be repaired and

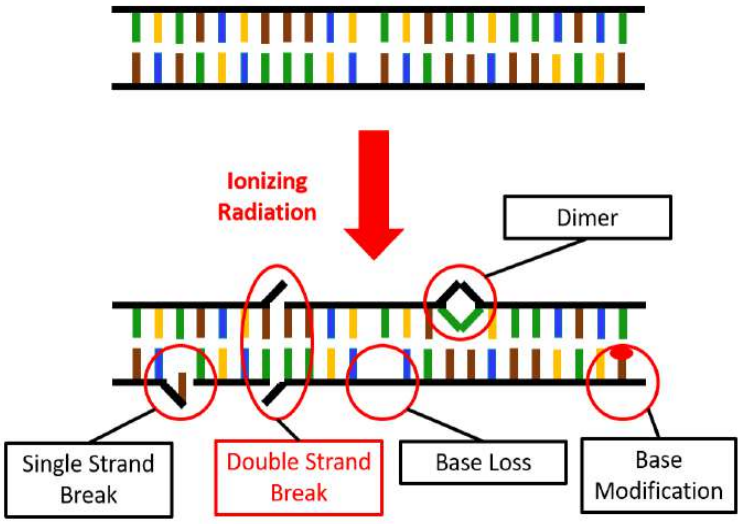

Figure 1.9: Graphical representation of different types of DNA damage induced by ionising radiation. (taken from [48]).

may eventually lead to cell death. At later times the so-called late reactions appear, which may finally lead to carcinogenesis.

Although all molecules in the cell might be damaged by ionising radiation, experimental results have demonstrated a strong correlation between radiosensitivity and DNA content. Indeed, the damage to the DNA molecule appears to be the decisive lesion for mutation induction, carcinogenic transformation and cell killing, due to its central role in all cellular functions, such as cell division and gene expression.
DNA damage can be induced by radiation in two different ways: indirectly or directly. In the former case, ionising radiation interacts with the water molecules surrounding the DNA molecule, leading to the production of highly reactive free radicals; these can migrate over distances of a few nanometres and react with the DNA or other molecules of the cell, damaging them. In the latter case, the DNA of the exposed cell is directly ionised, subsequently leading to the breakage of molecular bonds and the disruption of one or both strands of the DNA [47].

Due to the importance of DNA, cells and organisms have developed a complex series of processes and pathways for DNA-damage repair. Specialised repair systems have therefore evolved for detecting and repairing damage to bases, Single-Strand Breaks (SSB) and Double-Strand Breaks (DSB), which are the major types of DNA damage induced by ionising radiation (see Figure 1.9). Since the information on both strands

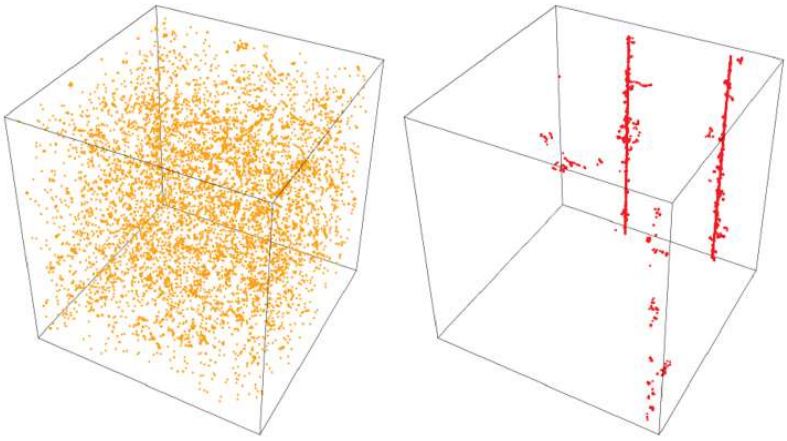

Figure 1.10: Representation of ^{60}Co photon (left) and 1 MeV proton (right) energy deposition patterns inside a cubic volume, for an absorbed dose of 2 Gy (taken from [49]).

of the DNA molecule is specular, injuries affecting only one strand of the double helix can be potentially easily repaired by using the duplicated information. Therefore, DSBs are generally considered as the critical event for the induction of lethal lesions.

The main radiobiological difference between photons and light ions resides in their different direct ionisation capability: while photon ionisation density can be assumed to be uniformly distributed and sparse, light ion ionisation density is very localised, as depicted in Figure 1.10. This implies a higher probability, with respect to photons, for DSBs, inducing a more severe damage to the cell.

1.3.1 Absorbed dose and radiation damage

To characterise the amount of radiation-induced damage during a radiotherapy treatment, one of the most important physical quantities is the dose deposited in tissues. The *absorbed dose* D is defined as the mean energy per unit mass deposited by ionising radiation in a mass element:

$$D = \frac{\mathrm{d}E}{\mathrm{d}m}. \tag{1.13}$$

The International System (SI) unit for the absorbed dose is the Gray (Gy), where $1\,\mathrm{Gy} = 1\,\mathrm{J\,kg^{-1}}$. The absorbed dose, though, is not enough to determine the biological effect of different radiation qualities, as the most striking difference between photons and ions concerns their microscopic spatial distribution of energy deposition events. A physical quantity which better describes the radiobiological effect of different types of radiation is the *Linear Energy Transfer* or LET. From a physical point of view, the LET is equal to the electronic stopping power, but conceptually focuses on the

energy locally given to the medium, rather than on the energy lost by the incident particle. As for the electronic stopping power, the LET is defined as the mean energy $\mathrm{d}E$ lost in the target medium by a slowing-down particle in a track segment of length $\mathrm{d}l$, and it is usually expressed in $\mathrm{keV\,\mu m^{-1}}$:

$$\mathrm{LET} = \left(\frac{\mathrm{d}E}{\mathrm{d}l}\right). \tag{1.14}$$

The LET defined in this way is called *unrestricted*. In some practical cases, it can be useful to exclude interactions that carry energy far away from the original track, imposing an upper threshold Δ for the energy of secondary electrons. This is usually referred to as *restricted* LET (LET_Δ), and tends to the unrestricted LET (thus to the electronic stopping power) if the threshold tends to infinity [51]. The physical absorbed dose and the LET are strictly related; indeed, for a parallel beam with particle fluence Φ, the dose deposited in a thin slice of an absorber material with mass density ρ can be calculated as:

$$D = 1.6 \times 10^{-9} \times \Phi \times \mathrm{LET} \times \frac{1}{\rho}. \tag{1.15}$$

The LET depends on the energy of a particle and, in the usual case of a beam with a broad energy spectrum, a distribution of LET will be observed in the exposed material. Therefore, to characterise the radiation field by a single parameter, a mean LET value must be used. There are two common ways of specifying LET distribution and, consequently, two different mean values: the *frequency distribution*, defined in terms of the total track length (which decreases as particles are stopped) of the incident particle or, equivalently, in terms of the particle fluence, and the *dose distribution*, defined in terms of the absorbed dose deposited by the particle at a specified LET [50, 51].

- *Frequency distribution*

  Let $F(L)$ be the distribution function of the fraction of the total track length that is associated with a LET not larger than L:

  $$F(L) = \frac{\phi_\mathrm{L}}{\phi}, \tag{1.16}$$

  where ϕ is the total fluence and ϕ_L is the fluence of particles with LET not exceeding L. The density of LET in track length or fluence is denoted by $f(L) = \mathrm{d}F(L)/\mathrm{d}L$, being the *frequency-* (or *track-*) *averaged* LET, $\overline{L}_\mathrm{F}$, its mean value:

$$\overline{L}_{\mathrm{F}} = \int L f(L)\,\mathrm{d}L. \tag{1.17}$$

- *Dose distribution*

  Let $D(L)$ be the distribution function of the fraction of absorbed dose due to particles with linear energy transfer not larger than L:

  $$D(L) = \frac{D_{\mathrm{L}}}{D}, \tag{1.18}$$

  where D is the total absorbed dose, and D_{L} is the absorbed dose due to particles with LET not exceeding L. The corresponding density of LET in dose is denoted by $d(L) = \mathrm{d}D(L)/\mathrm{d}L$. The *dose-averaged* (or *weighted-averaged*) LET $\overline{L}_{\mathrm{D}}$ is:

  $$\overline{L}_{\mathrm{D}} = \int L d(L)\,\mathrm{d}L. \tag{1.19}$$

The dose and frequency distributions of LET are related as follows:

$$d(L) = \frac{L f(L)}{\overline{L}_{\mathrm{F}}}. \tag{1.20}$$

Accordingly, the dose-averaged LET can be expressed in terms of the first two moments of $f(L)$:

$$\overline{L}_{\mathrm{D}} = \frac{1}{\overline{L}_{\mathrm{F}}} \int L^2 f(L)\mathrm{d}L = \frac{\overline{L^2_{\mathrm{F}}}}{\overline{L}_{\mathrm{F}}}. \tag{1.21}$$

1.3.2 Survival curves and Relative Biological Effectiveness

A common way to analyse the different effects of photons and light ions on living materials is by means of cell survival curves.

A cell survival curve describes the relationship between the physical dose and the portion of cells that survives. The word *survival* can take different meanings depending on the context, but usually refers to the capability of a certain cell type to preserve a specific function. In the case of proliferating cells, such as cancerous ones, the response of the cells to ionising radiation, in vitro, is frequently quantified in terms of the probability of *clonogenic* survival, where clonogenic refers to the ability of the survivor to maintain the reproductive integrity and duplicate to form a large colony. Cell survival experiments are relatively easy to perform: cells from an actively growing stock culture are irradiated and then incubated for 1 or 2 weeks before being fixed and stained. Then, cell proliferation is analysed counting as survivors only

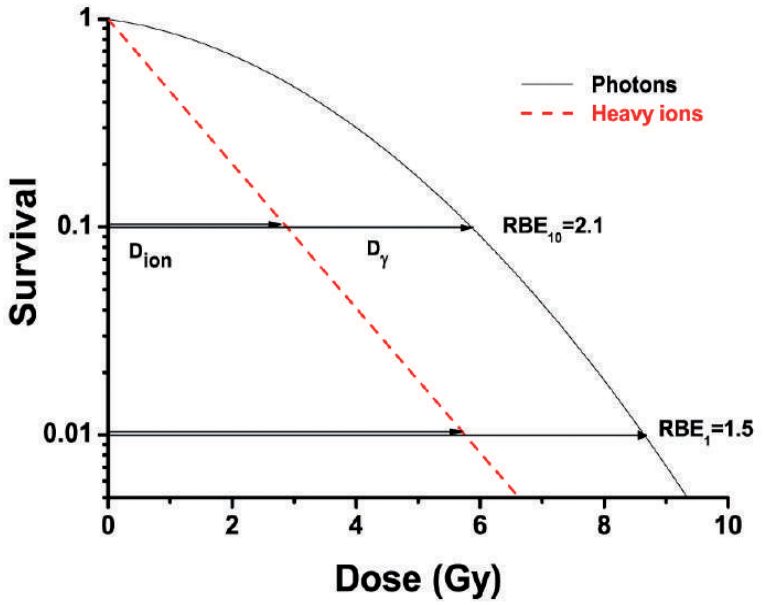

Figure 1.11: Survival curve for photons (solid black line) and ions (red dashed line), and determination of RBE at 10% and 1% survival level (taken from [42]).

those cells which have formed colonies with more than a certain threshold of daughter cells, usually set to 50. Finally the surviving fraction is given by normalisation to the number of seeded cells [47].
Survival curves are usually reported plotting the dose on a linear scale and the surviving fraction on a logarithmic scale, as shown in Figure 1.11.
Qualitatively, the shape of the survival curve can be described in simple terms:

- For low-LET radiation qualities, on the log-linear plot, the survival curve starts with a finite initial slope, bends for higher doses and finally straightens again for very high doses.
- For densely ionising or high-LET radiation qualities, the cell survival curve is linear in the log-linear plot throughout the whole dose range.

Therefore, the most common way to parametrise the cell survival curve is by means of an exponential function, theorised in the frame of the *Linear Quadratic* (LQ) model:

$$S(D) = \exp(-\alpha D - \beta D^2), \tag{1.22}$$

where S is the survival fraction, D is the absorbed dose and α and β are experimentally determined parameters. The LQ model assumes that there are two components to

cell killing by radiation, respectively proportional to the dose and to the square of the dose, which in some way depend on the severity of DNA damage. The ratio α/β determines the shoulder of the survival curve, i.e. the radiation sensitivity, and corresponds to the dose at which the linear and quadratic contributions to cell killing are equal. For a given endpoint, the dose-response curves from proton radiation are steeper than those for photon radiation (higher α/β), probably indicating a lower damage repair probability. This effect becomes more pronounced at low proton energies and, specifically, α typically increases with increasing LET while β is not significantly affected [25]. Even if the LQ model is rather accurate in the classical dose range of conventional radiotherapy, the picture just presented is greatly simplified, and a universal theory of radiation cell killing is not yet available [52, 53].

As mentioned in Section 1.3.1, the biological effects of radiation cannot be predicted only by means of the absorbed dose. In order to take into account the different biological effects induced by different radiation types for the same physical dose, the *Relative Biological Effectiveness* (RBE) coefficient has been defined: the ratio between the absorbed dose of a reference radiation (generally ^{60}Co, γ-rays or 250 keV X-rays) and that of the test radiation (for example light ions), required to produce the same biological effect (isoeffect):

$$\mathrm{RBE} = \left.\frac{D_{\mathrm{ref}}}{D_{\mathrm{test}}}\right|_{\mathrm{iso}} . \tag{1.23}$$

Typically, the RBE is determined from cell survival curves, using for example the 10% survival fraction as isoeffect, as shown in Figure 1.11.
It is important to note that the statement of a RBE value requires both the specifications of the reference radiation and the level of the biological effect. Usually, RBE values reported in literature use different types of reference photon energies, from mega-voltage to kilo-voltage [19]. As emerges from Figure 1.12, however, different photon energies are subject to a different LET, which for neutral beams is defined via the respective secondary electrons and charged products. Therefore, when reporting a RBE value, it is mandatory to give also the information about the reference radiation.

In spite of its simple definition, the RBE is a very complex radiobiological concept, which depends on several factors and variables. In the specific case of proton therapy treatments, however, a proton RBE relative to high-energy photons equal to 1.1 is currently assumed, neglecting any dependency of RBE on dose, biological endpoint or proton beam properties [19]. Nevertheless, it is well known that the RBE is not a constant, but clinical data can neither indicate that the use of a generic RBE of 1.1 is unreasonable nor confirm that it is correct [25]. Recently, efforts have been made to include a variable RBE scheme in proton therapy treatment planning, and several

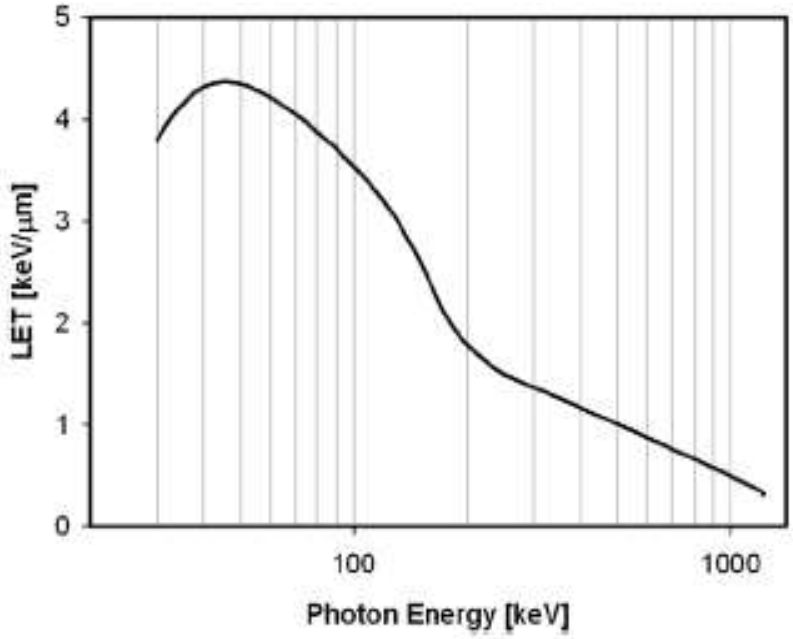

Figure 1.12: Dose-averaged LET of the resulting secondary electrons as a function of the nominal photon energy (taken from [19]).

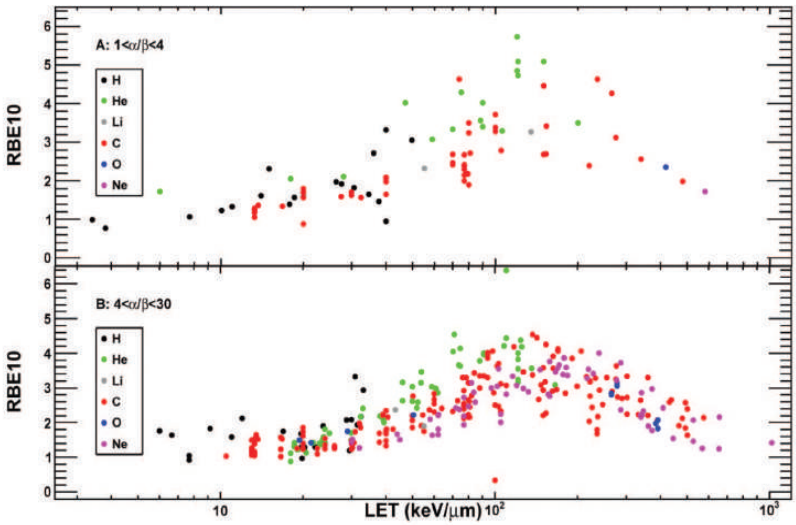

Figure 1.13: RBE at 10% survival of different monoenergetic particle beams as a function of LET, grouped in different α/β sensitivity ranges (taken from [54]).

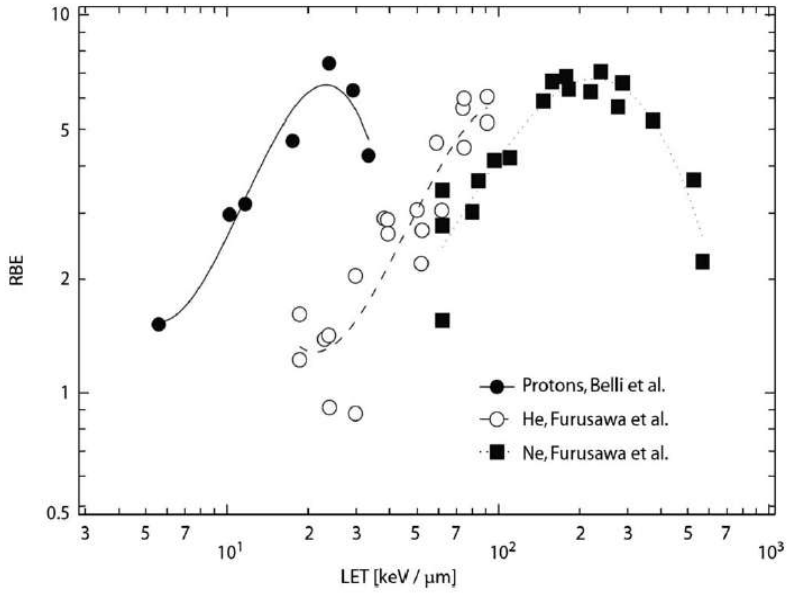

Figure 1.14: Variation of the $\mathrm{RBE}_\alpha = \alpha_{\mathrm{test}}/\alpha_{\mathrm{ref}}$ as a function of the particle type and the LET, where α_{ref} and α_{test} are the linear part of the survival curve for photons and ions, respectively (taken from [48]).

models have been proposed for proton RBE prediction [21]. Indeed, evidences exist that a generic RBE value of 1.1 could under- or overestimate the RBE for certain tumours or organs at risk, having a potential impact on the clinical efficacy of proton therapy [19].

In order to implement RBE variations in treatment planning, a deep understanding of the relationship between RBE and LET, dose and biological endpoint is necessary. In general, as emerges from Figure 1.13, for light ions, the RBE increases with increasing LET up to a certain maximum, and then decreases due to a saturation effect for LET values above $100\,\mathrm{keV\,\mu m^{-1}}$. This is related to the fact that, for very high LET, a single-particle traversal is sufficient to reduce the cell survival probability, making further ionisations unnecessary, leading to an "overkill" effect and to a decrease of RBE with increasing LET. For protons, the maximum RBE occurs at extremely low proton energies and a linear relation can be assumed between RBE and LET, with a slope depending on the biological endpoint [25].
The position of the RBE maximum is also influenced by the particle type, being shifted towards higher LET values for heavier particles as shown in Figure 1.14. For example, comparing protons and alpha particles in the LET region from 20 to $30\,\mathrm{keV\,\mu m^{-1}}$, the first show a higher effectiveness. This is related to the different track structure of the two particles: at equal LET, alpha particles have a higher

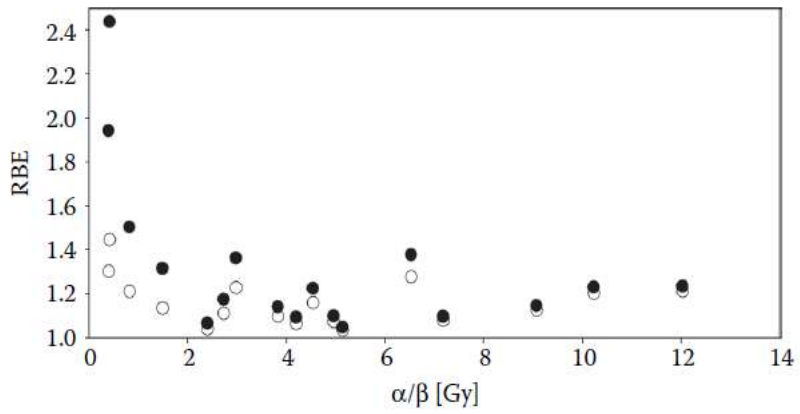

Figure 1.15: Proton RBE values calculated as a function of α/β for 2 Gy (full dots) and 6 Gy (open circles) (taken from [25]). An increase in RBE for late responding tissues ($\alpha/\beta < 4$ Gy) is observed for lower doses.

energy, resulting in broader tracks wih lower ionisation density in the centre, leading to a lower RBE.

Finally, by definition, the RBE depends on the dose and on the chosen level of effect, which can vary strongly based on the biological system considered. For example, normal and malignant cells respond differently due to differences in their repair and cell re-population mechanisms; furthermore, oxygenation is decisive, especially for indirect effects, as low oxygen levels may determine a greater resistance to radiation [47].

Usually, different cell lines and tissues are classified depending on the α/β ratio of the photon survival curve. Two main groups can be identified: early responding tissues (high α/β values above 4 Gy) and late responding tissues (low α/β values between 1 and 4 Gy), depending on their damage repair capability. The dependence of proton RBE on the α/β ratio has been extensively studied using experimental data and theoretical models [19]. Figure 1.15 shows that the RBE for late responding tissues seems to be higher than for early responding ones, and the biggest variations in RBE are expected to be observed for low α/β ratios at low doses. This, for example, can be advantageous in prostate (low α/β) treatment with proton therapy, but disadvantageous for other treatment sites, if for example the spinal cord has to be irradiated to achieve sufficient tumour coverage [25].

Some studies have been performed in the past, trying to include a variable RBE scheme in proton therapy treatment planning [21], based on different phenomenological models for RBE prediction [55,56]. Despite starting from different model assumptions, these studies have shown the importance of considering RBE corrections in treatment

plans, as consistent deviations to the current practice of proton therapy biological planning with a constant RBE of 1.1 have been observed [57–59]. These findings suggest that considering at least main RBE dependencies, i.e. dose, LET and α/β, would be beneficial for treatment planning, especially in correspondence to organs at risk and for late responding tissues. Therefore, the development of computational tools for the modelling of such variable RBE would be strongly advisable.

An alternative possibility with respect to the implementation of a variable RBE in proton therapy could be the use of a dose distribution optimisation based on physical quantities that can be predicted with higher accuracy. An example of this could be a LET-guided plan optimisation capable to maximise dose-averaged LET in the tumour while minimising it in the normal tissue, exploiting the linear dependence of the RBE on the LET [60, 61].

1.3.3 Microdosimetry

When describing the energy loss on a cellular level, the LET concept is only a crude approximation, because the pattern of energy deposition events, which are stochastic in nature, plays a role in defining the radiobiological properties of radiations with similar LET. Indeed, the LET is a macroscopic parameter that, by definition, describes the energy lost by an incident particle per unit path length, and it is not well suited to describe the energy actually deposited in sub-cellular volumes. On the other side, the biological effect of radiation depends strongly on the information about the energy distribution in microscopic structures and in the local concentration of radiation-induced ionisations.
To study the fluctuations of energy depositions in the tracks of charged particles, and the resulting biological effectiveness of radiation, the formalisms of *microdosimetry* was introduced by Rossi and co-workers [62–64]. Microdosimetry postulates that the biological effect of radiation is determined by the amount of energy deposited in certain sensitive cellular structures called *sites*. The basic microdosimetric quantities are the *energy imparted*, ϵ, the *specific energy*, z and the *lineal energy*, y, defined in a site S of a specified shape and size, usually having micron dimensions [65].
The energy imparted ϵ is the sum of all energy transfers ϵ_i within S:

$$\epsilon = \sum_i \epsilon_i. \tag{1.24}$$

The energy imparted is a random variable, and its value varies with repeated irradiations, being the fluctuations greater for small sites, densely ionising radiations and small doses. Therefore, predictions can be only made on the basis of probability distributions.

The specific energy z is closely related to the energy imparted and it is defined as:

$$z = \frac{\epsilon}{m} \tag{1.25}$$

where m is the mass of the site. The specific energy can be considered as the stochastic microscopic analogous of the absorbed dose, and in the SI it is given in Gy as well.

Finally the lineal energy y is somehow the stochastic analogous of the LET, and it is defined by the quotient:

$$y = \frac{\epsilon_{\mathrm{s}}}{\bar{l}}, \tag{1.26}$$

where ϵ_{s} is the energy imparted to the site by a single energy-deposition event, and $\bar{l}$ is the mean chord length of the site. The chord length l is a stochastic quantity and represents the length of a particle track within a site. It depends on the shape and dimensions of the site and, if the track is considered as a straight line, $\bar{l}$ is defined as the mean length of randomly oriented chords in the site, whose determination is a purely geometric problem.

An important concept in microdosimetry is that of *event* in a site, defined as the energy deposition due to particles that are statistically correlated, e.g. a charged particle and all the secondary electrons generated by its interaction with matter. The *single-event distribution* $f(\epsilon_{\mathrm{s}})$ of the energy imparted is defined as the distribution of energy deposited in the site by exactly one event:

$$f(\epsilon_{\mathrm{s}}) = \frac{N_{\epsilon_{\mathrm{s}},\mathrm{d}\epsilon_{\mathrm{s}}}}{N}, \tag{1.27}$$

where $N_{\epsilon_{\mathrm{s}},\mathrm{d}\epsilon_{\mathrm{s}}}$ is the number of events with energy imparted in the interval $[\epsilon_{\mathrm{s}}, \epsilon_{\mathrm{s}}+\mathrm{d}\epsilon_{\mathrm{s}}]$, and N is the overall number of events.

The expectation value of ϵ_{s} following $f(\epsilon_{\mathrm{s}})$ is called frequency-mean imparted energy per event $\bar{\epsilon}_{\mathrm{sF}}$, and it is given by:

$$\bar{\epsilon}_{\mathrm{sF}} = \int_0^\infty \epsilon_{\mathrm{s}} f(\epsilon_{\mathrm{s}})\, \mathrm{d}\epsilon_{\mathrm{s}}. \tag{1.28}$$

For radiobiological considerations, it is also useful to consider the *weighted* or *dose distribution* $d(\epsilon_{\mathrm{s}})$ of the energy imparted per event, where the contribution of each event is weighted by the energy it deposits:

$$d(\epsilon_{\mathrm{s}}) = \frac{\epsilon_{\mathrm{s}} f(\epsilon_{\mathrm{s}})}{\bar{\epsilon}_{\mathrm{sF}}}. \tag{1.29}$$

The expectation value of ϵ_{s} following $d(\epsilon_{\mathrm{s}})$ is called dose-mean imparted energy per

event $\overline{\epsilon}_{\mathrm{sD}}$, and it is given by:

$$\overline{\epsilon}_{\mathrm{sD}} = \int_0^\infty \epsilon_{\mathrm{s}} d(\epsilon_{\mathrm{s}})\,\mathrm{d}\epsilon_{\mathrm{s}} = \frac{1}{\overline{\epsilon_{\mathrm{sF}}}} \int_0^\infty \epsilon_{\mathrm{s}}^2 f(\epsilon_{\mathrm{s}})\,\mathrm{d}\epsilon_{\mathrm{s}} = \frac{\overline{\epsilon_{\mathrm{sF}}^2}}{\overline{\epsilon}_{\mathrm{sF}}}. \tag{1.30}$$

From Equation (1.30) it is possible to relate both averages through:

$$\overline{\epsilon}_{\mathrm{sD}} = \overline{\epsilon}_{\mathrm{sF}} + \frac{\sigma_{\epsilon_{\mathrm{s}}}^2}{\overline{\epsilon}_{\mathrm{sF}}}, \tag{1.31}$$

where $\sigma_{\epsilon_{\mathrm{s}}}^2$ is the variance of $f(\epsilon_{\mathrm{s}})$.

Since $\epsilon_{\mathrm{s}} = z_{\mathrm{s}} \cdot m = y \cdot \bar{l}$, where $z_{\mathrm{s}} = \epsilon_{\mathrm{s}}/m$ is the single event specific energy, frequency and dose mean specific and lineal energy can be defined in an analogous way:

$$\overline{z}_{\mathrm{sD}} = \frac{\overline{z_{\mathrm{sF}}^2}}{\overline{z}_{\mathrm{sF}}}, \qquad\qquad \overline{y}_{\mathrm{D}} = \frac{\overline{y_{\mathrm{F}}^2}}{\overline{y}_{\mathrm{F}}}. \tag{1.32}$$

The frequency mean lineal energy, $\overline{y}_{\mathrm{F}}$, is approximately analogous to the frequency mean LET, $\overline{L}_{\mathrm{F}}$, introduced in Section 1.3.1. If energy-loss straggling and the lateral escape of δ-rays out of the site are negligible, and if the range of the ionising particle is sufficiently large, the two mean values tend to be equal and $\overline{L}_{\mathrm{F}} = \overline{y}_{\mathrm{F}}$. As demonstrated by A. Kellerer in different works [66–68], a relation between the dose-averaged LET, $\overline{L}_{\mathrm{D}}$, and its microdosimetric equivalent, $\overline{y}_{\mathrm{D}}$, can also be derived. The demonstration, however, is not straightforward and will be discussed in more detail in Chapter 3.

Microdosimetric Kinetic Model

One of the main advantages of the microdosimetry theory is that it permits the calculation of RBE from a microscopic approach by means of the Microdosimetric-Kinetic Model (MKM) [69–71]. The foundations of this model lay on the theory of dual radiation action [72], which predicts that the observable effect of ionising radiation is determined by the combined action of sub-lesions, generated in the cell by a specific pattern of energy deposition, interacting in pairs to produce lethal lesions. Based on this concept, the following fundamental assumptions are made in the MK model [73]:

1. a cell nucleus can be divided into a number of microscopic volumes called domains;

2. following radiation exposure, two types of DNA damage are created in cell nuclei, named lethal and sub-lethal;

3. the number of these lesions in a domain is proportional to the specific energy z deposited in the domain;

4. a sub-lethal lesion can be repaired or converted into a lethal lesion by spontaneous transformation or interaction with another sub-lethal lesion created in the same domain;

5. a domain is to be considered dead when a lethal lesion is formed within it;

6. a cell is considered dead when a domain in its nucleus has died.

Lethal lesions correspond to clustered DNA damages that are difficult to repair and induce chromosome aberrations, whereas sub-lethal lesions are likely to be double-strand breaks or similar damages that are generally repaired but, occasionally, mis-repaired. In order to be repaired, the two sides of a break must not drift apart and/or combine with another lesion. It is unlikely that actual compartments exist in the nucleus corresponding to domains. More probably, the diameter of the domain is a measure of the distance a sub-lethal lesion can travel through the nucleus before being removed by repair. Nevertheless, the concept of a domain is useful, as mammalian cells are found to survive or die after irradiation as if they had compartments like domains, with diameters ranging from 0.5 to 1 µm [71].
The concept of domain is equivalent to the physical sites described by theoretical microdosimetry. According to the MK model, therefore, the effects of ionising radiation on a cell population depend on the statistical distribution of energy imparted, or specific energy z, to these sites. The average number of lethal lesions L in a domain for a specific energy z is given by [71]:

$$L = A\overline{z} + B\overline{z}^2, \tag{1.33}$$

where A and B are domain dependent parameters.
Each passage of a charged particle through or close to the domain, determining an energy deposition, identifies an event. The number of events in a domain is a random variable following a Poisson distribution whose mean value and variance are equal to $\overline{\nu}$. Furthermore, the dose deposited in a domain by each event z_s is itself a random variable, whose frequency mean is $\overline{z}_\mathrm{sF}$. Therefore, if a nucleus contains N domains, the average number of lethal lesions in a nucleus L_n is given by:

$$L_\mathrm{n} = N\overline{L} = N\left(A\overline{z} + B\overline{z^2}\right) = N\left(A\overline{z} + B\left(\overline{z}^2 + \sigma_\mathrm{z}^2\right)\right), \tag{1.34}$$

where σ_z^2 is the standard deviation of the distribution of z in a domain. The specific energy z imparted to a domain by a beam is a function of the single event specific energy z_s. At a specified absorbed dose D, indeed, the specific energy imparted to

the domain is the result of a *compound Poisson process* with $D = \overline{z}$, and it can be demonstrated that $\overline{z} = \overline{\nu}\,\overline{z}_{\mathrm{sF}}$ and $\sigma_{\mathrm{z}}^2 = \overline{z}_{\mathrm{sD}} D$ [68].
For a LET low enough (approximately $40 - 90\,\mathrm{keV\,\mu m^{-1}}$ depending on the cell type [74]), so that the lethal lesions can be considered as Poisson distributed among the cells of the irradiated population, the fraction of cells that survive without a lethal lesion is $\ln S = -L_{\mathrm{n}}$. Therefore, substituting the previous equivalences in Equation (1.34), the following relation is obtained:

$$L_{\mathrm{n}} = -\ln S = (\alpha_0 + \beta_0 \overline{z}_{\mathrm{sD}})\, D + \beta_0 D^2, \tag{1.35}$$

where $\alpha_0 = NA$ and $\beta_0 = NB$ are parameters independent of LET and represent the α, β parameters of the linear quadratic model in the limit LET = 0. Therefore, for a general radiation type R, $\alpha_{\mathrm{R}} = \alpha_0 + \beta_0 \overline{z}_{\mathrm{sD}}$ and $\beta_{\mathrm{R}} = \beta_0$. Knowing that the single event microdosimetric quantities z_{s} and y are related by $z_{\mathrm{s}} = \left(\bar{l}/m\right) y$, and assuming a spherical domain, the expression for α_{R} can be rewritten as:

$$\alpha_{\mathrm{R}} = \alpha_0 + \beta_0 \left(\frac{\overline{y}_{\mathrm{D}}}{\rho \pi r_{\mathrm{d}}^2} \right), \tag{1.36}$$

where ρ and r_{d} are the density and radius of the domain. As already mentioned, Equation 1.35 is valid as long as the number of lethal lesions in the domain can be considered as Poisson distributed. Indeed, corrections to the MK model will be generally necessary to account for the overkill effect happening for high-LET radiation [71, 73]. However, in the case of protons, typical $\overline{y}_{\mathrm{D}}$ values are not large enough to reach the overkill effect [75], and Equation (1.36) can be used as a valid estimator of the LQ model parameters.

1.4 Monte Carlo simulations

Computer simulations are used in many areas of research and development and, among them, Monte Carlo techniques are rapidly increasing their relevance in the field of medical physics, especially for particle therapy [76]. Indeed, Monte Carlo simulations are an essential tool in particle therapy for many reasons, as they can be used for the design and commissioning of clinical facilities, for treatment room design, for shielding and radiation protection, for the commissioning of treatment planning systems and for other applications [25]. This comes from the fact that Monte Carlo techniques allow the precise simulation of experimental conditions and, if properly benchmarked, can be used to create potential scenarios that are difficult to reproduce experimentally, as it is the case of a patient being treated with particle therapy. The main goal of these simulations in radiation therapy is the prediction of the delivered dose distribution to the patient, especially in cases where the accuracy of treatment

planning systems (TPS) may not be optimal due to the particular geometry of the treatment volume. However, such simulations constitute also a powerful tool to study the physics of proton beams, and find multiple applications in the field of proton therapy research.

The Monte Carlo method is the most detailed for the simulation of particle interactions within a medium. In general, Monte Carlo techniques are numerical methods that use random numbers to solve mathematical problems. These techniques, which were initially developed to solve differential equations and calculate integrals, can be used to simulate physical interactions on a step-by-step basis. The basic structure of the Monte Carlo method is simple: first of all, a random number is sampled from a probability density function of the magnitude of interest; then, this procedure is repeated a number N of times so that the outcomes of the simulations are statistically independent; finally, the value of the quantity of interest is computed as the mean value of the obtained results, with an error proportional to $1/\sqrt{N}$ as follows from the *Central Limit Theorem*.
The simulation of a particle track begins by sampling a number of events (usually called *histories* in medical physics) from a starting source distribution. Then, the passage of the particle through a well-defined geometry and material is simulated, randomly sampling from one or more probability distributions at each step, to choose how the particle interacts in consistency with the laws of physics. This procedure is known as tracking.
In the specific case of charged particles, the outcome of such a Monte Carlo simulation depends on the chosen step size. The smaller the step size, the more precise the simulation results will be, but also more time consuming. Indeed, for uncharged particles like photons, it is feasible to simulate all physics processes as they travel in a straight line until a discrete interaction occurs (compton, photoelectric effect, etc.), while this approach would be computationally ineffective for charged particles like protons, which have a high interaction probability. Based on these considerations, two main approaches exist in the development of Monte Carlo codes for charged particles tracking: the *condensed history* method and the *track structure* method.

- **Condensed history**

  In condensed history algorithms, a particle trajectory is segmented into discrete steps in which energy losses and directional changes are condensed (or summed). Therefore, at the end of each step, the scattering angle of the particle and the energy transferred to the surrounding materials are determined using stochastic methods based on the interaction probabilities of the relevant physical processes. Typically, a maximum step size is defined, up to which continuous energy loss and a certain multiple coulomb scattering angle is assumed. Furthermore, a

threshold for the explicit production of secondary particles might be defined, below which continuous energy loss of the primary particle is assumed. This permits to increase the computational efficiency of the simulation, provided that not tracking these secondaries does not alter the simulation outcome.

- **Track structure**

  In a track structure algorithm, interactions are simulated as they happen in the real world on an collision-by-collision basis, following an explicit model of each interaction. This technique is highly relevant at the microscopic scale but also very time consuming, therefore it is usually applied below a certain energy threshold, where particle tracking is switched from condensed history to event by event mode.

Typically, Monte Carlo methods use a combination of both condensed history and track structure algorithms, to model continuous and discrete processes, respectively. In proton therapy, for example, discrete processes are typically nuclear interactions, secondary particle production and large angle Coulomb scattering, while other processes are usually treated with the condensed history approach [25].

In the following, the Monte Carlo codes used in this thesis work will be presented briefly.

SRIM (The Stopping and Range of Ions in Matter) This program is specialised in ion transport calculations up to 2 GeV through a geometry defined by subsequent layers of different materials. It does not require a registration for its use, but the source code is not public [77]; the current version is SRIM-2013.

GEANT4 (Geometry ANd Tracking) This code is able to simulate the transport of particles of any kind in an energy range from 250 keV to 10 TeV. It is especially powerful in the reproduction of complex geometries and can be used both in high energy physics applications and medical physics. The current version of GEANT4 is 10.6 (released in December 2019), its source code is totally public and no registration is needed for its use [78–80].

GEANT4-DNA This code is an extension of GEANT4, which contains processes for the modelling of biological damage induced by ionising radiation at the DNA scale. In GEANT4-DNA, all the included processes are discrete and simulate physical interactions in liquid water following a track structure approach down to the eV scale [81–84].

1.5 Radiation Dosimeters

Dosimetry is one of the most important aspects of physics in radiation therapy, since the assessment of the dose is a fundamental part of treatment planning. Usually, quality assurance measurements are done in water phantoms and most analytical dose calculation algorithms are based on water models, therefore dosimetry in radiation therapy is mostly based on dose to water [85].
Dosimetry detector systems have different specifications; most of them, however, are based on the detection of dose-dependent magnitudes such as charge, heat, light or changes in the optical or chemical properties produced by the incident radiation on the detector material [86]. In general, to be employed as a dosimeter, a detector must own a physical property which can be correlated to the dosimetric quantity of interest with a proper calibration. Furthermore, dosimeters should ideally have the following properties: a linear response to the dose received, an independence from the energy of the incoming particle and a high spatial resolution.
Primary standards for reference dosimetry are typically set by regulatory bodies, and standard laboratories measure absorbed dose as accurately as possible under selected reference conditions [33]. For particle therapy, there is in general agreement that calorimetry is the method of choice for reference dosimetry, since temperature rise is the most direct consequence of energy absorption in a medium. Water calorimeters are the most popular but calorimeters based on other materials, for example graphite, are used as well [13]. An alternative for reference dosimetry in particle therapy is given by ionisation chambers that, once calibrated towards a primary standard, can be used for the calibration of radiotherapy beams.
In the next sections, some of the most common detectors used for dosimetric purposes will be presented, focusing especially on the radiation detectors employed for the purpose of this thesis.

1.5.1 Ionisation chambers

Ionisation chambers are used in radiotherapy and diagnostic radiology for the determination of radiation dose and for absolute dosimetry during routinely quality assurance. These detectors are basically made of a cavity filled with gas surrounded by conductive walls and having a central collecting electrode, as shown in Figure 1.16. Their operation principle is based on the collection of electron-ion pairs generated when the incident radiation ionises the gas contained in the chamber, whose number is proportional to the energy deposited. By applying an electric field, the electrons are accelerated towards the anode and the ions towards the cathode, generating a current signal whose intensity depends on the magnitude of the voltage applied. In order to reduce leakage current when the chamber is polarised, the wall and the

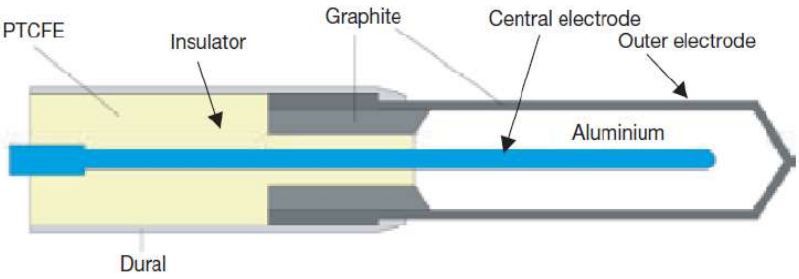

Figure 1.16: Scheme of a typical ionisation chamber (Farmer type). In the picture, the materials used as electrodes, walls and insulators are also indicated (taken from [86]).

collecting electrodes are separated by an insulator. Furthermore, a guard electrode is usually provided, which intercepts the leakage current and allows it to flow to ground, improving the field uniformity in the sensitive volume. Finally, the output current generated by ionisations and collected by the electrode is generally very small and needs to be measured with an electrometer.

In the experimental measurements conducted in this thesis, a parallel plate ionisation chamber was used. Chambers of this kind are usually made by two plane walls, serving as entry window and polarising electrode and as back wall and collecting electrode, respectively, separated by a guard ring system. Parallel plate ionisation chambers are usually recommended for dosimetry of electron beams with energies below 10 MeV [86]. Therefore, for detecting low energy protons as those used in this project (see Chapter 2) a special ionisation chamber with thinner electrodes was used, built at the GSI Helmholtz Centre for Heavy Ion Research laboratories (Darmstadt, Germany).

1.5.2 Silicon detectors

Silicon is the most widely used semiconductor material for charged particle detection [37]. A silicon dosimeter is basically a p-n junction diode, made by taking an n type (excess of electrons) or p type (excess of holes) silicon and counter-doping the surface to produce the opposite type material.
In the interface between the two materials of a p-n junction, the difference in the concentration of electrons and holes generates a diffusion of holes towards the n-region and a similar diffusion of electrons towards the p-region (see top panel of Figure 1.17a). Since p and n structures are initially neutral, the electron-hole recombination occurring after diffusion generates a charge build up on each side of the junction and therefore an electric field gradient across the junction. The region of changing potential is known as depletion zone and is sensitive to the passage of ionising radiation: electron-hole pairs created in this area after a ionisation event

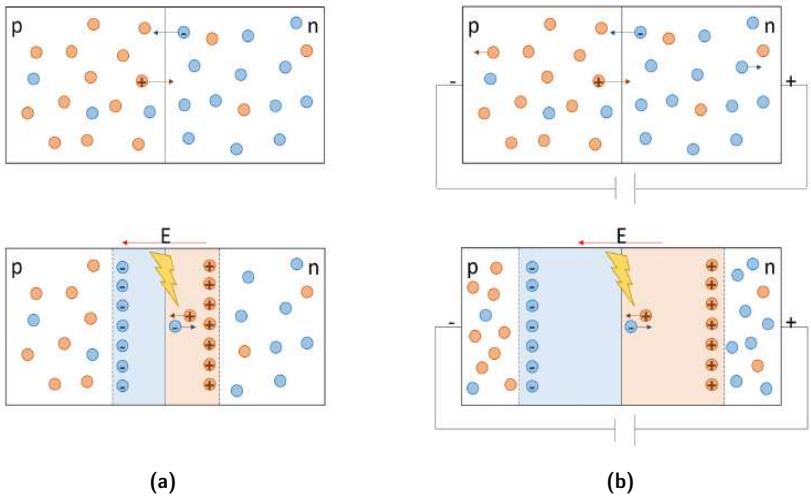

Figure 1.17: Working principle of a p-n junction without **(a)** and with **(b)** the application of an inverse bias voltage to increase the size of the depletion zone.

are swept out by the electric field and, if electrical contacts are placed on either end of the junction, a current signal proportional to the ionisation can be detected, as shown in Figure 1.17a (bottom panel).

In order to increase the depth of the depletion zone and the sensitive volume of the detector, an inverse bias voltage is usually applied to the junction, as shown in Figure 1.17b. The maximum voltage that can be applied, however, is limited by the resistance of the semiconductor.

In radiotherapy applications, p-type silicon is generally used for dosimetry [86], as it is less affected by radiation damage and has a small dark current, i.e. a small fluctuating current that flows through the junction when the voltage is applied, contributing to the signal noise. Silicon dosimeters are very sensitive and small in size, being particularly useful for measurements in phantoms with small fields and high dose gradients. However, they can be employed only for relative dosimetry, since they are affected by radiation damage and their sensitivity might change with repeated use.

For the experimental measurements conducted in this thesis, a lithium-drifted silicon detector was used. One drawback of silicon detectors is the difficulty of achieving a depletion zone thicker than a few millimetres, necessary to stop a proton beam of tens of MeV. This problem is solved with lithium-drifted silicon detectors [37], which can reach a depletion zone with thicknesses up to $10 - 15$ MeV.

1.5.3 Radiochromic films

Radiochromic films are extensively employed in radiation therapy for quality assurance measurements [87]. These films are mainly used for photon dosimetry because their response is independent on the energy of the incident clinical photons. This is not true in the case of proton irradiation, where an energy dependence emerges if the highly ionising region of the Bragg peak falls inside the active layer of the film [88–93].

The most widely used radiochromic films in recent years are the Gafchromic EBT films (Gafchromic, International Specialty Products, Wayne, New Jersey, USA), which show a significantly increased sensitivity with respect to the previous models available [94]. Different EBT type films exist, such as EBT2 and the most recent EBT3 and EBT-XD [95], each of them having different properties and dynamic ranges. For the measurements performed in this work, EBT3 films were used.

EBT3 type films are made of a single 28 µm thick active layer (56.8% H, 27.6% C, 13.3% O, 1.6% Al and 0.6% Li, with a mass density of $1.2\,\mathrm{g\,cm^{-3}}$ [96] compatible with Lucite), mounted between two 125 µm thick polyester substrates. Their composition is nearly tissue equivalent [86, 87] and they contain a special dye that is polymerised under exposure to ionising radiation developing a blue colour. The polymer absorbs light, whose transmission through the film can be measured with a suitable densitometer such as a flatbed scanner. EBT3 films are self-developing films and do not require post exposure processing. The full colour development of these films is usually very rapid, occurring in a few milliseconds. However, some chemical processes require more time, minutes and even hours after irradiation, to reach completion. Therefore, a time window of 24 h is usually recommended before scanning [97].

The dynamic dose range of these films goes from 0.1 Gy to 20 Gy, but the optimum dose range lays between 0.2 Gy and 10 Gy. Above 10 Gy the EBT3 dose response curves show a shallow slope, which may lead to increased uncertainties at higher doses [98].

The working principle of radiochromic films is based on the colour change after radiation exposure, which is somehow proportional to the absorbed dose. The response of a radiochromic film to irradiation is commonly expressed in terms of the change in its net optical density (netOD), that represents the difference in optical densities of the same film piece sampled after and before irradiation, where the optical density is computed as the logarithm of the inverse transmission. To compute the netOD, pixel values (PV) of the film scanned in transmission mode are sampled over predefined regions of interest and the following formula is applied:

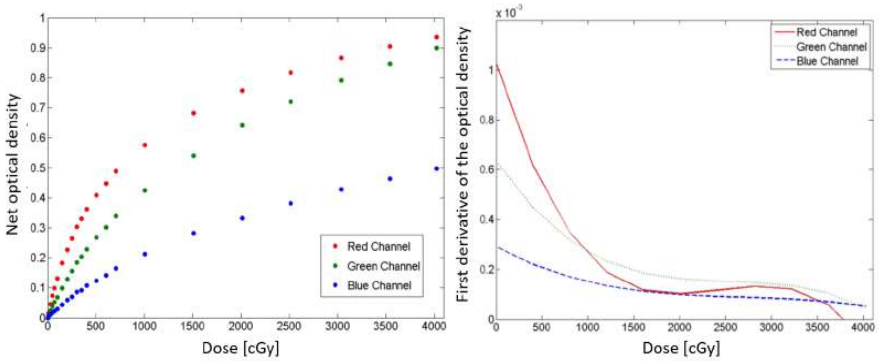

Figure 1.18: EBT3 dose response curves (left) and first derivatives (right) for dose values up to 40 Gy, plotted for the three colour channels that compose the image: red, green and blue (taken from [99]).

$$\text{netOD} = \text{OD}_\text{f} - \text{OD}_\text{i} = \log_{10}\frac{PV_0}{PV_\text{f}} - \log_{10}\frac{PV_0}{PV_\text{i}} = \log\frac{PV_\text{i}}{PV_\text{f}}, \tag{1.37}$$

where PV_0 represents the pixel value of a non attenuated beam and for a 16-bit image is equal to 2^{16}, and PV_i and PV_f are the pixel values of the film before and after irradiation, respectively.

As can be observed in Figure 1.18, each colour channel of a scanned EBT3 film shows a different slope in the netOD-to-dose curve, related to the different ratio between the dose dependent and dose independent portion of the signal [99]. The red channel has a higher response from 0 to 10 Gy, visible from the derivative of its response curve in this dose range, which is higher than the green and blue ones. Above 10 Gy, the use of the green channel would be preferable, while the blue channel is generally less useful for dose measurements. Recently, dosimetric methods have been proposed for the combined used of all colour channels for the computation of the dose [100, 101]; however, the discussion of these methods is beyond the scope of this thesis.

Radiochromic films are known to show a significant under-response in dose for higher LET radiation in the proximity of the Bragg peak [88–93]. This effect, known as quenching, is related to the local saturation of the polymerisation process: the number of radiation-induced activated polimerysation sites increases with LET until, eventually, no more sites are available for activation and the polimerysation stops locally. Therefore, corrections must be applied if films are used for dose determination in the Bragg peak region or, more generally, in low energy ion beams [92, 93].

1.6 Work outline

The work performed during this doctoral thesis was framed in the context of proton RBE variability, a topic that has been faced with two different approaches. The first one, experimental, focused on the design of a beam line for radiobiology experiments at the 18 MeV proton cyclotron installed at the National Centre of Accelerators (CNA, Seville, Spain). The second one, computational, was centred on the development of a Monte Carlo track structure application for the computation of microdosimetric quantities in water, to be used for the calculation of macroscopic dose-averaged LET distributions.

The core of the thesis is divided in three main parts. Chapter 2 is dedicated to the description of the radiobiology beam line, focusing especially on the overall optimization of the beam parameters to define the best setup for the irradiation of mono-layer cell cultures. In this chapter, a Monte Carlo simulation of the beam line, realised with Geant4 and validated towards experimental measurements, is also presented.

In Chapter 3 the Monte Carlo track structure application developed for the computation of microdosimetric distributions of protons in liquid water, is described. This application, based on Geant4-DNA, provides two sampling methods, uniform and weighted, for the scoring of the quantities of interest in spherical sites. Furthermore, it is used to verify the validity range of a formula that links microdosimetric quantities to the macroscopic dose-averaged LET distribution, being a powerful tool for the development of analytical models to be used in treatment planning optimisation.

Chapter 4 presents the results of the first irradiation of cell cultures at the radiobiology beam line developed at the cyclotron facility. In this context, an application of the Monte Carlo code for the computation of microdosimetric quantities is shown. With this code, a theoretical derivation of the expected RBE for the experimental irradiation and cells under study could be done, through the use of the microdosimetric kinetic model.

Finally, Chapter 5 collects a summary of the results obtained, followed by a brief discussion on the future perspectives of this work.

Chapter 2

Preparation of a radiobiology beam line at the 18 MeV proton cyclotron facility at CNA

2.1 Introduction

As explained in Section 1.3.2, in current clinical practice it is assumed that proton beams are 10% more efficient than clinical photon beams as for cell-killing effectiveness; i.e., they have a constant RBE value of 1.1. However, the conventional use of this value has been questioned for some time, as the RBE varies with parameters such as tissue type, dose, biological endpoint and LET [19]. Nevertheless, the lack of accurate biological data, makes it difficult to implement biophysically optimised treatment plans in clinical practice. In this context, radiobiological investigations using particle accelerators have gained an increasing interest in the last decades [102–106], aiming at collecting accurate biological data especially for proton energies typically found at the Bragg peak region of clinical beams, roughly below 40 MeV, where the RBE is expected to increase [19, 107].
Low energy proton accelerator facilities provide the perfect tool for this kind of studies, as they can produce high LET beams with narrow energy distributions. In fact, radiobiological experiments with low energy protons should be ideally performed at facilities providing proton beams with nominal energy below the limit mentioned, in order to minimise the straggling related to passive degradation.

At the National Centre of Accelerators (CNA, Seville, Spain), two beam lines of this kind are available at the 3 MV tandem (Pelletron 9SDH-2 model) and at the cyclotron (Cyclone 18/9 model) facilities, respectively. To adapt these beam lines for radiobiological studies, special beam optimisation and dosimetric techniques

Figure 2.1: Picture of the experimental room. From the exit flange to the room wall there is approximately a distance of 2 m.

are needed [102–106]. Indeed, radiobiological experiments at proton facilities pose stringent conditions both on the physical and on the biological point of view. Firstly, a homogeneous dose distribution throughout the biological sample must be ensured, with a meaningful dose rate comparable to that used in the clinic ($\approx 2\,\mathrm{Gy\,min^{-1}}$). Furthermore, when dealing with low-energy accelerators, the limited particle range (lower than 5 mm in water for a proton beam of 20 MeV) makes it difficult to irradiate samples in tissue flasks filled with medium, meaning that cells must be exposed inside open culture vessels vulnerable to bacterial contaminations. Finally, as biological targets are always made of living material, the environmental parameters such as room temperature, air pressure and humidity must be kept under control, to ensure no external factor impacts on the cell viability.

In the case of the radiobiology beam line designed for the 3 MV tandem, these constraints were met by making some significant changes in the beam line, adding a manipulator for the insertion of a scattering foil in the vacuum pipe and a fast-closing valve to start and stop irradiations [106]. A specific sample holder was then designed, to irradiate cell culture plates in the vertical position, removing the growth medium immediately before exposure and treating the cells immediately afterwards to fix the

damage.

Compared to the tandem, the 18 MeV cyclotron facility offered some increased challenges, mainly related to its installation environment and workflow. First, unlike the tandem beam line, the experimental beam line of the cyclotron is common to different research groups and it is devoted to multi-purpose research. Therefore, potential changes in the beam line structures should interfere neither with the experimental work of other groups nor with the normal workflow of the production of radioisotopes for Positron Emission Tomography (PET). Second, the space available in the experimental room is limited (approximately 2 m from the exit window to the wall, see Figure 2.1), and the insertion of new elements extending the length of the beam line was not feasible.

In this chapter the setup proposed for the irradiation of cell samples at the cyclotron facility is presented, focusing in particular on the beam optimisation procedures and dosimetric characterization, and on the Monte Carlo simulations performed to attain these tasks.

2.2 Materials and Methods

The cyclotron installed at the CNA in Seville is a Cyclone 18/9 from the IBA company (Ion Beam Applications, Louvain-La-Neuve, Belgium), which accelerates protons and deuterons to 18 and 9 MeV, respectively. This cyclotron has eight target ports: seven dedicated to the production of radioisotopes for PET and one used for the transport of the proton beam to an external beam line for interdisciplinary research.

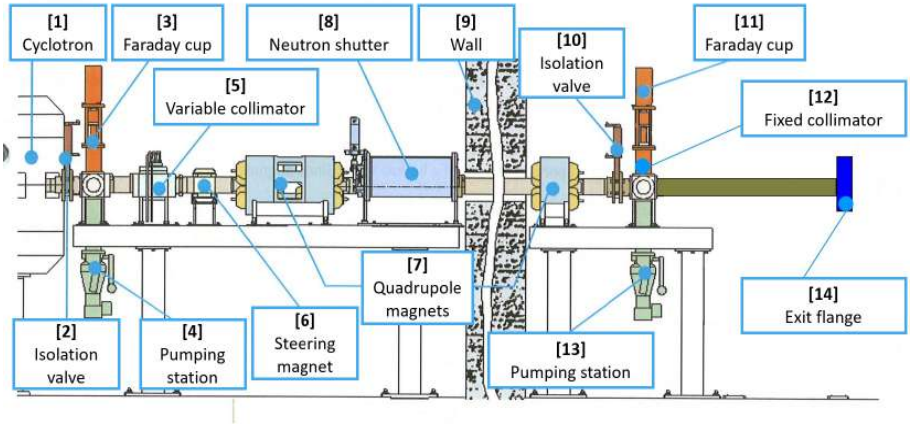

Figure 2.2: Schematic representation of the beam line (not scaled).

In this section, the procedures and equipment used to obtain a proton beam suitable for the irradiation of cell samples are described, focusing on the characterisation of the beam energy and profile and on the optimisation of the experimental setup for radiobiological measurements.

2.2.1 Beam line

As depicted in Figure 2.2, the 18 MeV proton beam, produced by the cyclotron, proceeds horizontally to the experimental room via the beam transport system.
The beam line is divided into two sections, respectively located in the cyclotron bunker and in the experimental room, separated by a two meter thick concrete wall (number **9** in Figure 2.2). The first section includes a series of remote control permanent elements to monitor and define the beam current and size:

1. a retractable graphite Faraday cup for beam current monitoring (number **3**);
2. a variable graphite slit (number **5**), an XY set of magnetic steerers (number **6**) and a quadrupole doublet (number **7**, left) for beam shaping and guidance.

A neutron shutter (number **8** in Figure 2.2) completes this part of the beam line, protecting the downstream elements in the experimental room from neutron radiation when the cyclotron is under operation for radioisotopes production.
The second section of the beam line, in the experimental room, contains a single quadrupole magnet (number **7**, right), a circular water-cooled fixed aluminium collimator of 15 mm diameter (number **12**), a pumping station (number **13**) and a second retractable graphite Faraday cup (number **11**), covered with a phosphor scintillator (ZnS–Ag) to observe the beam shape and size by means of a video camera. Finally, a pneumatic isolation valve (number **10**) placed between the wall and the fixed collimator, and controlled manually from the control room, can be used to isolate the vacuum in the cyclotron from the beam pipe of the experimental room.

All the elements described above are an integral part of the experimental beam line, and cannot be modified or replaced without interfering with the normal workflow of the facility or with other research activities. Apart from them, however, two other components complete the beam line, playing a major role in the optimisation of the system for the irradiation of cell cultures: a manipulator (not represented in Figure 2.2), for the insertion of targets in the vacuum pipe, and the exit flange (number **14**). The target manipulator is placed between the wall and the isolation valve, at a distance of 2 m from the exit flange, and can be used to insert scattering foils of different thicknesses and materials in the beam path. It has different slots for the insertion of various targets, whose position can be changed manually. However

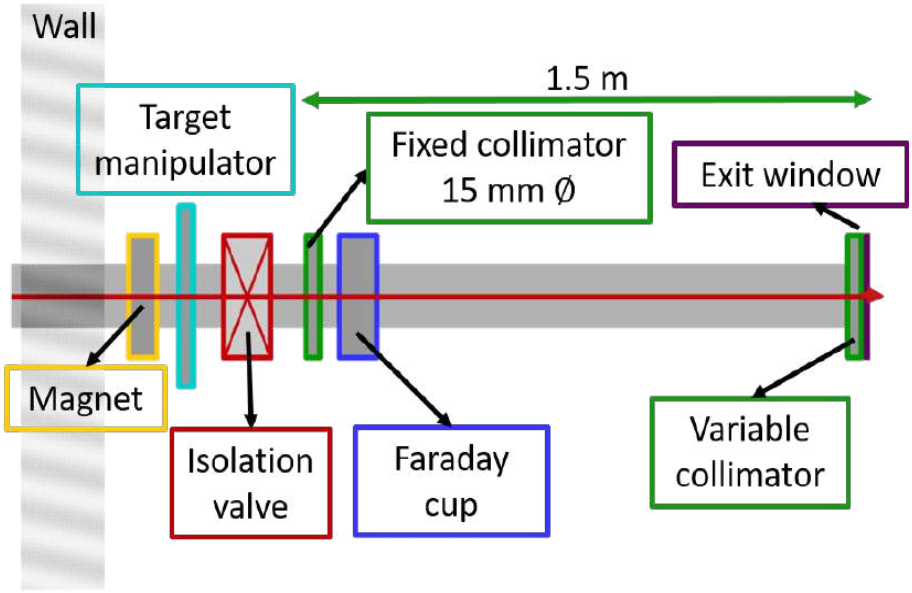

Figure 2.3: Graphical representation of the external beam line in the experimental room (not scaled), with a particular focus on the positioning of the two collimators.

due to its placement upstream the isolation valve, the insertion of targets in the manipulator can only be done during special maintenance days, when the whole beam line and cyclotron are ventilated. For this reason, the preliminary tests for the development of the radiobiology beam line at the cyclotron facility were conducted degrading the beam directly in air, placing scattering foils of various thicknesses after the exit window.

On its part, the design of the exit flange was especially developed to reduce activation of its components during irradiation, covering the internal part with a 5 mm thick absorbent layer of graphite acting as a collimator with customisable inner diameter. Therefore, on its path the beam encounters two subsequent collimators, as shown in Figure 2.3, the aluminium one of 15 mm diameter, and the graphite one with variable aperture, separated by a distance of 1.5 m. Finally, exit windows of different materials and thicknesses can be attached to this collimator, being Mylar the material chosen for the purpose of this study.

As already mentioned, some major requirements must be taken into account when it comes to the irradiation of biological samples.

1. The beam intensity impinging on the sample should be of the order of tens of pA to control properly the fluence within suitable irradiation time scales. Ideally, a dose rate comparable to that used in the clinic should be achieved, of the order of $2\,\mathrm{Gy\,min^{-1}}$.

2. In order to cover the whole sample a broad irradiation field is necessary, which in the case of Petri dishes means of about 10 cm^2.

3. All cells in the sample must receive the same dose, therefore a homogeneous beam profile in both energy and spatial distribution must be achieved over the whole sample surface.

Following these considerations, the first measures taken were to lower the extracted beam current to the minimum achievable, without losing beam stability, and to turn off all the magnets for beam optics, with the aim of enlarging the beam spot by having a completely unfocused beam. With these conditions, however, the control of the position of the beam maximum intensity became harder, and could be only partially achieved by resorting to the set of steering magnets placed immediately after the cyclotron exit port.

The solutions presented above were not enough to attain the objective sought. Therefore, two different approaches were tested, both relying on passive degradation through scattering foils to reduce beam intensity and enlarge the beam spot. The general underlying principle is that of taking advantage of the multiple Coulomb scattering occurring when the beam traverses any material, while preserving at the same time a narrow energy distribution with the highest possible mean energy value. To do so, ideally, very thin foils of a high Z material should be used, such as gold or tungsten, since Coulomb scattering and energy straggling are directly proportional to the atomic number of the material, being the second also linear with the material thickness.

Due to the initial difficulties encountered in the insertion of scattering foils directly in the manipulator mounted inside the beam line, the first tests for the preparation of the radiobiology beam line were conducted intercepting the beam directly in air. Furthermore, at the beginning of the project, all the available flanges had a built-in collimator of 15 mm diameter. The first feasibility study, therefore, was carried out by placing tungsten scattering foils of two different thicknesses, 150 and 220 µm, immediately after a 125 µm thick Mylar exit window.

For the final setup, instead, a 500 µm aluminium scattering foil was inserted in the manipulator to scatter the beam at a further distance from the sample, taking advantage of the subsequent angular spread to flatten the profile. Then, a different exit flange was chosen for the irradiation of biological samples, consisting of a 100 µm thick Mylar window mounted on a circular graphite collimator of 40 mm diameter. A summary of the differences between the two exit flanges can be found in Table 2.1. As described in Section 2.3.2, with these modifications a higher degree of homogeneity could be achieved at the position of the samples, reducing the distance from the exit

Table 2.1: Summary of the characteristics of the two exit flanges used for the preliminary and final configurations tested for the preparation of the radiobiology beam line.

Exit Flange	Preliminary (A)	Final (B)
Collimator diameter	15 mm	40 mm
Window material	Mylar	Mylar
Window thickness	125 µm	100 µm

window and increasing the energy range available, if compared to the preliminary setup.

2.2.2 Monte Carlo simulation

As emerges from the previous section, the cyclotron external beam line structure is simple and versatile, having been installed for general purpose experiments and interdisciplinary research. This beam line does not count on many devices for beam diagnostics, being the two Faraday cups the only instruments available to monitor the beam. Furthermore, the limited space left in the experimental room, approximately 2 m from the exit window to the wall, reduces the possibility of inserting new elements for diagnostics extending the length of the beam line. Finally, the necessity to turn off all the focusing magnets, makes it more difficult to control the beam optics and to get information about the position of the maximum beam intensity.
Taken together, the previous considerations imply that beam diagnostics must necessarily be performed at the exit of the beam line, in air, measuring the beam energy distribution and lateral profiles and comparing the observations with Monte Carlo simulations. To this end, a dedicated and versatile Monte Carlo application with GEANT4 was developed, to reproduce the geometry of the beam line and the different experimental setups mounted for measurements.

In the following, the characteristics of the Monte Carlo code developed and the measurements carried out to characterise the beam and benchmark the simulation are presented.

Geometry

Figure 2.4 illustrates the geometry of the simulation of the experimental beam line. The primary protons are created 2 m far from the exit flange, immediately upstream the aluminium scattering foil; if not intercepted by the aluminium collimator, protons proceed horizontally in the vacuum pipe, cross the exit window and reach the detector, whose characteristics and distance from the flange are easily customisable. The various elements of the beam line have been implemented with an accuracy better than 2 mm in what respects their thickness and positioning.

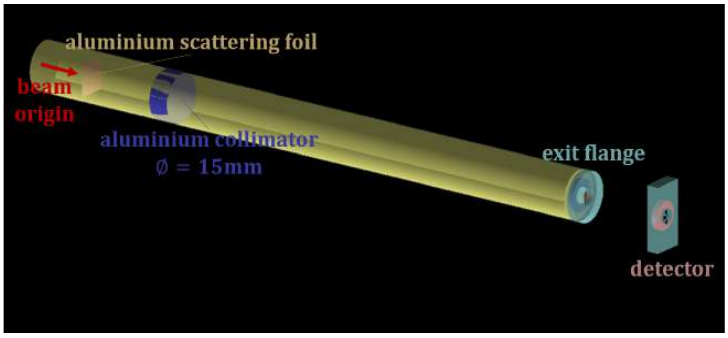

Figure 2.4: Geometry of the GEANT4 simulation developed to reproduce the cyclotron external beam line.

To make this simulation versatile, the materials, dimensions and positions of all the variable elements, i.e., scattering foils, exit window and detectors, can be changed before running the simulation by a series of simple macro commands, so that no new compilations of the code are needed whenever a parameter is changed. An example of a typical macro file for the initialisation of the geometry is shown in the following:

Listing 2.1: Geometry initialisation

```
[...]
# %%%% SCATTERING FOIL IN MANIPULATOR %%%%
/mygeom/foil            false
/mygeom/FoilZ           500. um
/mygeom/FoilMat         G4_Al

# %%%% EXIT WINDOW %%%%
/mygeom/EWColR          7.5 mm
/mygeom/WindZ           125 um
/mygeom/WindMat         G4_MYLAR

# %%%% SCATTERING FOIL IN AIR %%%%
/mygeom/degrader        true
/mygeom/DegZ            150 um
/mygeom/DegMat          G4_W

# %%%% DETECTOR: IONISATION CHAMBER %%%%
/mygeom/holder          false
/mygeom/chamber         false

# %%%% DETECTOR: EBT3 FILM %%%%
/mygeom/film            false
/mygeom/FilmMat         G4_POLYSTYRENE
```

```
/mygeom/SensFilmMat     G4_LUCITE

# %%%% DETECTOR: SILICON DETECTOR %%%%
/mygeom/sidet           true
/mygeom/SiDetZ          5. mm
/mygeom/SiDetR          4. mm
/mygeom/SiColZ          5. mm
/mygeom/SiColR          4. mm
/mygeom/SiColMat        G4_GRAPHITE

# %%%% FILM TO EXIT WINDOW DISTANCE %%%%
/mygeom/WFdist          30. cm

# %%%% CHAMBER HOLDER TO EXIT WINDOW DISTANCE %%%%
/mygeom/WHdist          25.3 cm

# %%%% SILICON DETECTOR TO EXIT WINDOW DISTANCE %%%%
/mygeom/WSdist          22.5 mm
[...]
```

where the boolean variables allow to insert or remove specific elements, and the commands ending with `Z`, `R` or `Mat` set their length along the beam axis, radius (if applicable) and material, respectively. Specifically, the example reported in Listing 2.1 refers to one of the configurations for the measurement of the beam energy distribution, characterised by the exit flange (A) in Table 2.1, on which a tungsten scattering foil of 150 µm is attached for beam degrading, and the silicon detector as the only scorer activated.

Following the definition of the geometry, the initial characteristics of the beam must be implemented in the code to allow for a realistic reproduction of the experimental measurements. To this end, different experiments were performed, whose results were used to adjust the initial beam parameters, such as energy spread and shape, and validate the simulations. Since the aim of these measurements was to infer the initial characteristics of the beam, to be eventually used in other experimental applications, they were carried out without the aluminium scattering foil inside the beam line.
All the simulations were conducted by using our computing cluster hosted at Centro Informático Científico de Andalucía (CICA, Seville, Spain), consisting of 24 computational nodes, each with 2×12C AMD Abu Dhabi 6344 (2.6 GHz/6 MB) L3.

Determination of the beam energy distribution

The measurements to obtain the energy distribution of the beam were carried out with the exit flange of the preliminary configuration (A) in Table 2.1. A lithium-

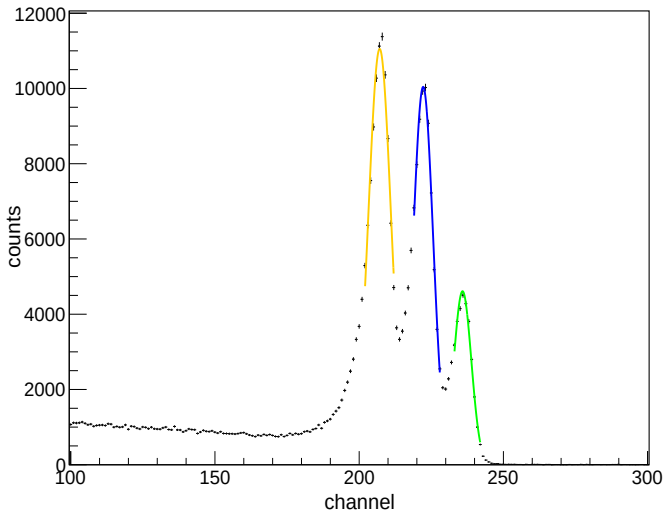

Figure 2.5: Fit of the α MCA spectrum acquired with the silicon detector. Each of the three peaks has been fitted with a Gaussian function, to extract information about the position of the mean value. These fits have been performed only on the peaks, since the Gaussian tails of the three emissions are overlapping each other and with noise. The results of these fits are reported in Table 2.2.

drifted silicon detector (L-040-075-5, ORTEC, Oak Ridge, Tennessee, USA) was used to measure the energy and energy distribution of the beam. This detector, powered with a bias voltage of 800 V, has an active thickness of 5 mm, sufficient to stop the 18 MeV protons coming from the cyclotron. To calibrate the detector and its electronic chain, a triple alpha source of ^{239}Pu–^{241}Am–^{244}Cm was employed.

The three isotopes of the ^{239}Pu–^{241}Am–^{244}Cm emit, on their most probable decay channels, α particles of energies 5156.59, 5485.56 and 5804.82 keV respectively. Due to the limited range of these α particles in air, the calibration of the silicon detector and its electronic chain was carried out attaching the radioactive source to the external support of the detector, at a distance of 2.5 mm from the surface of the active area. Then, to derive the actual energy of the particles impinging on the detector, a SRIM simulation was used.

After being amplified, the signal coming from the detector was read by a multi-channel analyser (MCA-8000D, AMPTEK, Bedford, Michigan, USA) and the content of each channel was saved in a ROOT histogram format to be subsequently analysed with a custom-made ROOT macro. This macro acquired the histogram and then fitted the three peaks of the α spectrum with Gaussian functions, as shown in Figure 2.5, in order to extract information about the mean channel value to be associated with the respective α energies.

Table 2.2: Summary of data points used for the calibration curve plotted in Figure 2.6. The initial particle energies (E_{in}) are the decay energies of the α particles and the nominal energy of the proton beam; while the final energies (E_{fin}) are those with which the particles imping on the detector, computed with SRIM. The associated MCA channels have been extracted from the Gaussian fit of the measured spectra.

particle	E_{in}	E_{fin}	channel
α ^{239}Pu	5156.59 keV	4916.8 keV	207
α ^{241}Am	5485.56 keV	5256.2 keV	222
α ^{244}Cm	5804.82 keV	5585.8 keV	235
proton	18 MeV	17.46 MeV	738

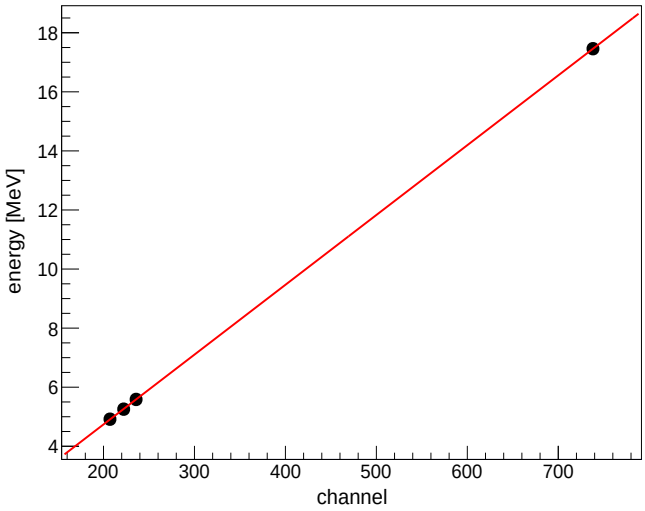

Figure 2.6: Calibration curve energy-channel of the silicon detector. The points in Table 2.2 have been fitted with a linear equation of the form $y = p_0 + p_1 \cdot x$, where $p_0 = 0.01(9)$ MeV and $p_1 = 0.0236(3)$ MeVchannel^{-1}.

The α source used covers only the energy range $4.9 - 5.5$ MeV, while the maximum proton energy emitted by the cyclotron, 18 MeV, is well above. Even if a linear response of the detector towards higher energies can be assumed, for the sake of the calibration an extra measurement was taken, irradiating the detector with the direct proton beam. This was done to avoid subsequent extrapolations far from the calibration range with experimental points. The high energy point was then added to the calibration curve, computing again with SRIM the residual energy of the proton after crossing the exit window and the air distance to reach the detector. Indeed, a difference of 10 channels was observed for an energy of 18 MeV between calibration curves depending on the inclusion or not of the high energy point, leading to a difference in energy of almost 0.3 MeV. Table 2.2 collects the information about

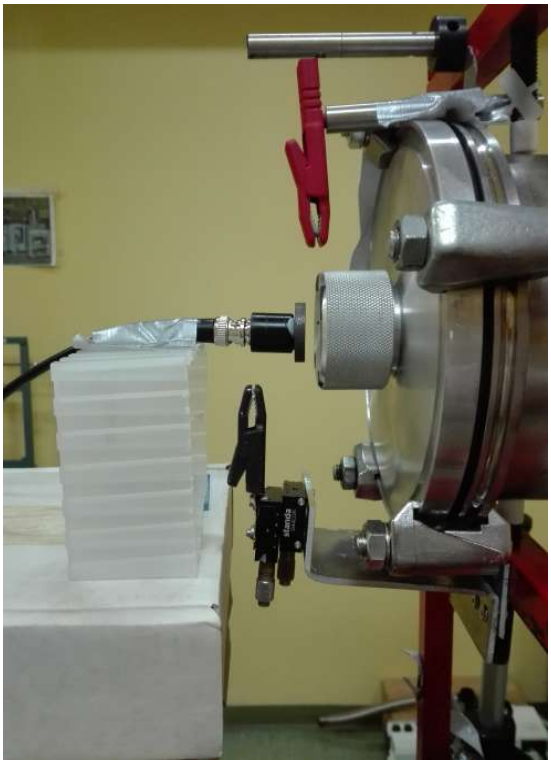

Figure 2.7: Setup for the measurement of the energy distribution of protons with a 5 mm thick lithium-drifted silicon detector.

the points used to build the energy-channel calibration curve shown in Figure 2.6.

Once calibrated, the silicon detector was used to measure the energy distribution of the beam in different configurations, by placing the detector in front of the exit window together with a graphite collimator of 1 mm diameter to avoid saturation, and by degrading the beam with tungsten scattering foils with thicknesses ranging from 50 to 320 µm. A picture of the experimental setup is shown in Figure 2.7.

Finally, experimental spectra were compared to simulated ones to find the optimal values for the initial mean energy and energy spread, to be inserted as initialisation parameters in the Monte Carlo code. To this end, a point-like proton source with Gaussian energy distribution was simulated, setting the mean energy equal to 18 MeV and changing the standard deviation from 0.10 to 0.18 MeV in steps of 10 keV. The optimal value for the energy spread was then set as that minimising the differences between experimental and simulated data for all the experimental configurations considered.

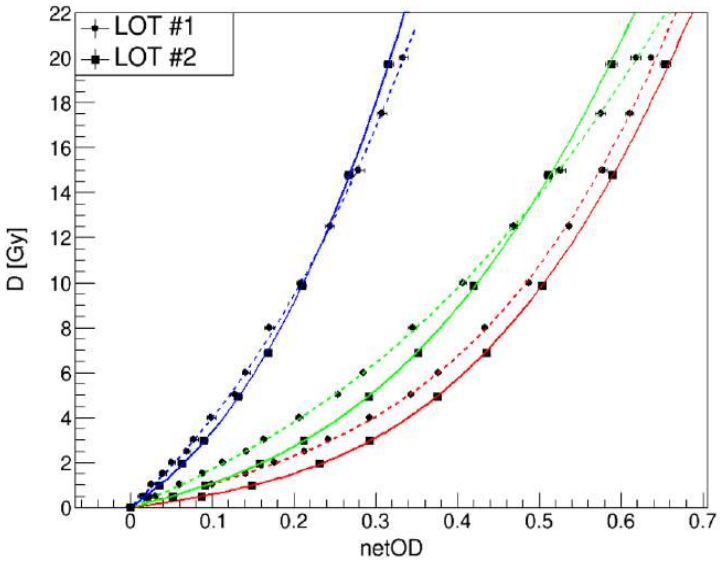

Figure 2.8: EBT3 dose-to-optical density calibration curves under 6 MV photon irradiation, for two different lots of films identified as #1 (full dots) and #2 (full squares). The measured points have been fitted with functions of the form $D = a \cdot \text{netOD} + b \cdot \text{netOD}^c$; the results of these fits are listed in Table 2.3 for the two lots (#1 full lines and #2 dotted lines) and for the three colour channels: red, green and blue.

Determination of the beam profile

After determining the energy distribution of the beam, various measurements were carried out to determine its spatial distribution, using Gafchromic EBT3 films previously calibrated under known photon doses at the "Virgen Macarena" University Hospital in Seville. A medical linear accelerator (Siemens ONCOR, Siemens Healthineers, Erlagen, Germany) in 6 MV photon mode was used for this calibration, irradiating stripes of a sheet of EBT3 film from the same lot used at the cyclotron, with doses in the range $0 - 20$ Gy, under standard conditions, i.e., $10 \times 10\,\text{cm}^2$ field size, Source to Surface Distance (SSD) equal to 10 cm and at a depth of 1.5 cm in solid water at the isocentre. Twenty-four hours after irradiation, the films were scanned with an Epson Perfection V700 photo scanner (Suwa, Nagano, Japan), and acquired images converted from colour value to net optical density (netOD). To do so, films were scanned in transmission mode with a resolution of 75 dpi, 48-bit colour mode and without any image correction, taking special attention to scan all the images in the same direction. Digitised films were saved using an uncompressed tagged image file format (tiff) to be lately analysed with ImageJ (Image processing and analysis in Java), a public domain software for image processing.

Different lots of EBT3 films might have in principle different optical properties, which

Table 2.3: Results obtained for the parameters of Equation (2.1) from the fit of the data in Figure 2.8 for the three colour channels and for the two lots used.

Film Lot	Parameter	Red Channel	Green Channel	Blue Channel
#1	a [Gy]	10.2 ± 0.2	16.0 ± 0.5	35 ± 3
	b [Gy]	61 ± 3	33 ± 2	110 ± 40
	c	3.44 ± 0.09	2.51 ± 0.13	2.4 ± 0.3
#2	a [Gy]	5.4 ± 0.2	9.6 ± 0.2	26 ± 4
	b [Gy]	57 ± 2	59 ± 4	180 ± 60
	c	3.03 ± 0.07	2.68 ± 0.10	2.4 ± 0.3

can also vary with time. Therefore, a different photon calibration curve should be applied every time a new lot is used, and should be ideally checked for a known dose and eventually corrected previously to any measurement.

During the experimental campaigns conducted at the CNA, two lots of EBT3 films were used, whose photon calibration curves are reported and compared in Figure 2.8 for the three colour channels (red, green and blue). Fit functions of the type:

$$D = a \cdot \text{netOD} + b \cdot \text{netOD}^c, \tag{2.1}$$

were used to fit the data points, as suggested in literature [108]; the results of these fits, for the different colour channels, are listed in Table 2.3. Since the irradiation of the films to obtain the calibration curves was performed in solid water, the doses reported in Figure 2.8 are intended in water.

The dose-to-optical density calibration curves obtained in the red channel (most sensible in the dose range $0 - 10$ Gy, see Section 1.5.3) were then used to convert in a first approximation the experimental netOD profiles measured at the cyclotron to dose, with the purpose of comparing them with the ones obtained from the Monte Carlo simulation. These profiles were measured in air at various distances from the exit flange (see Figure 2.9) and with various experimental configurations, listed in Table 2.4.

The average beam energy impinging on the active layer of the film ranged from 17.2 to 13.6 MeV, as reported in Table 2.4. While the EBT3 response to photon radiation is generally independent from the energy, this is not true for proton radiation, where a saturation in the darkening, or quenching effect, emerges as the LET increases [93]. Even if the application of the same calibration curve to all the configurations considered is not strictly correct, in the energy range considered the quenching effect is very small [92], and therefore the same calibration curve has been used for all the experimental configurations.

Considering the characteristics of the experimental proton beam produced, which was

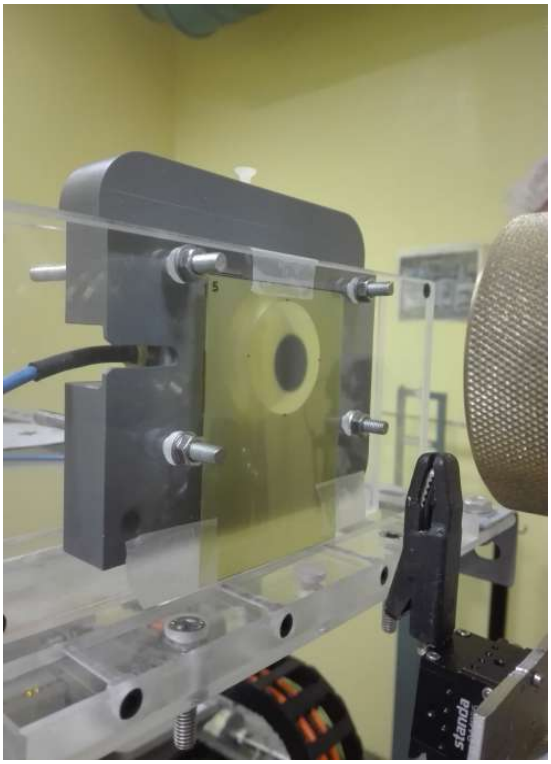

Figure 2.9: Example of a setup for the measurement of the beam profiles. A piece of EBT3 film is placed at a distance of 10.9 cm from the exit flange (configuration **B.2** in Table 2.4).

Table 2.4: Experimental configurations for the determination of the spatial characteristics of the proton beam to be compared with Monte Carlo simulations. Two different exit flanges have been used, described in Table 2.1. All these measurements were carried out without inserting the aluminium foil in the beam line; two of them (**A.3** and **A.4**) were performed attaching a thin tungsten foil to the exit flange. The distance reported was measured from the exit window to the surface of the film. Finally, the energy corresponds to the average proton kinetic energy impinging on the active layer of the film.

Configuration	Film Lot	Exit Flange	W Foil	Distance	Energy
A.1	#1	(A)	—	48 cm	15.5 MeV
A.2	#1	(A)	—	63 cm	15.0 MeV
A.3	#1	(A)	50 µm	48 cm	14.1 MeV
A.4	#1	(A)	50 µm	63 cm	13.6 MeV
B.1	#2	(B)	—	0.5 cm	17.2 MeV
B.2	#2	(B)	—	10.9 cm	16.9 MeV
B.3	#2	(B)	—	15.7 cm	16.7 MeV
B.4	#2	(B)	—	20.5 cm	16.5 MeV
B.5	#2	(B)	—	25.3 cm	16.4 MeV
B.6	#2	(B)	—	51.5 cm	15.5 MeV
B.7	#2	(B)	—	65.9 cm	15.0 MeV

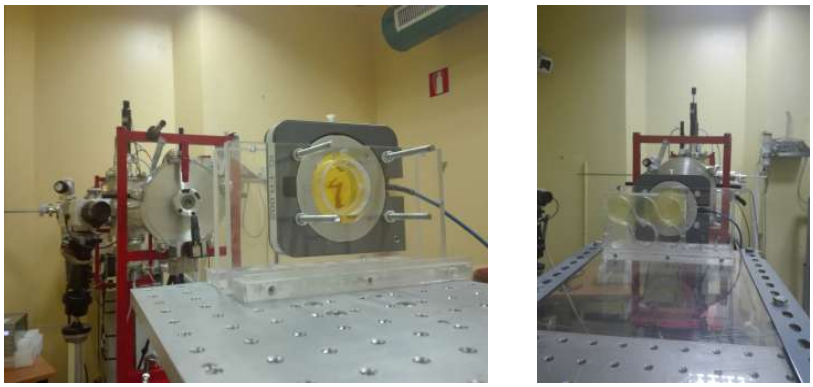

(a) (b)

Figure 2.10: Pictures of the experimental setup for dosimetry and irradiation of biological samples. The ionisation chamber is placed between two PMMA supports on a moving table on which a plastic board can be screwed to extend its length (see **(b)**). On the back of the second holder, a custom made guide can be mounted to allow for the positioning of Petri culture dishes or pieces of EBT3 film.

completely defocused and collimated with a 15 mm collimator 1.5 m upstream the exit window, two initial spatial configurations were tested in the simulation: uniform circular, with a radius of 8 mm, and Gaussian elliptical, with a sigma varying from 8 to 20 mm independently in both directions on the transversal plane.

2.2.3 Setup for the irradiation of cell samples

The experimental setup for dosimetry and for the irradiation of cell samples, shown in Figure 2.10, is similar to that used in the 3 MV tandem radiobiology beam line [106]. It consists of a Polymethylmethacrylate (PMMA) holder, made of two supports of 1 cm thickness each, mounted on a table which can be moved remotely with micrometric precision. Each side of the sample holder has a circular collimator of 35 mm diameter, coinciding with the entrance and exit windows of a parallel plate ionisation chamber inserted in between. This chamber, especially designed at the GSI-Heavy Ion Research Centre laboratory (Darmstadt, Germany) for radiobiology experiments with ions, is made of three thin parallel kapton electrodes of 7.5 µm with two air gaps of 6.75 mm thickness in between, operates at 400 V and it is connected to an electrometer (Unidos E, PTW, Freiburg, Germany) for charge readout. On the back of the holder, a custom made guide is mounted to allow for the positioning of Petri culture plates in the vertical position, with one plate aligned with the PMMA collimator and beam each time. This position can be also used to make dosimetric studies by means of Gafchromic EBT3 type films. Finally, to extend the length of the table and move the samples closer to the exit window, a rigid plastic board has

Table 2.5: Summary of the characteristics of the two configurations, preliminary and final, tested for the preparation of the radiobiology beam line.

	Preliminary	Final
Manipulator	Out	In
Foil material	—	Aluminium
Foil thickness	—	500 µm
Fixed Collimator	In	In
Collimator diameter	15 mm	15 mm
Exit Flange	(A)	(B)
External Foil	In	Out
Foil material	Tungsten	—
Foil thickness	150-220 µm	—
Window-Sample distance	50 cm	25 cm

been designed and built, which is screwed to the table and moves jointly with it.

To attain beam homogeneity over the whole sample surface, as already mentioned in previous sections, the beam had to be scattered through foils of different thicknesses and materials, and samples placed at an appropriate distance from the exit window. In the optimisation process, two different configurations were tested, whose characteristics are summarised in Table 2.5.
However, these measures alone were insufficient, since the beam needed also to be centred so that its maximum intensity reached the sample. Indeed, a slight misalignment

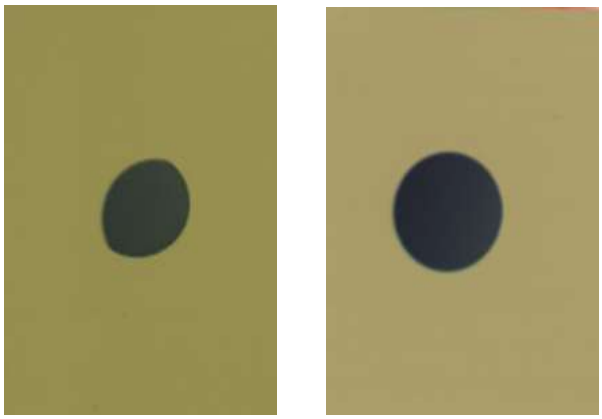

Figure 2.11: Beam spots measured by attaching a piece of EBT3 film directly on the exit flange in the **(a)** preliminary and **(b)** final configurations. A misalignment of the beam with respect to the fixed collimator is clearly visible in **(a)**, where the spot appears to be cut on one side. This effect fades away in **(b)** thanks to the insertion of the aluminium foil in vacuum, which increases beam divergence.

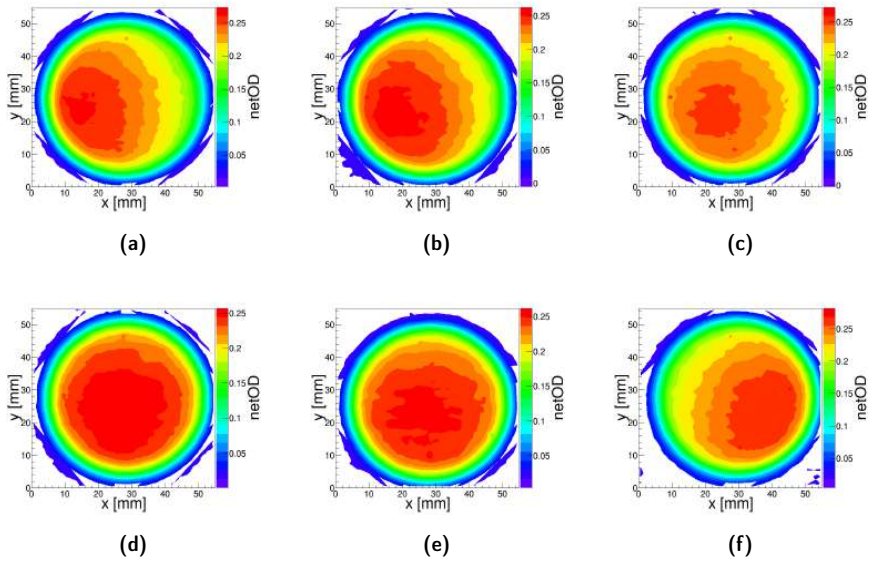

Figure 2.12: Displacement of beam maximum intensity as a function of steering magnets coordinates along x-axis. No evident displacement emerged by varying y-axis coordinates, therefore the current applied to the steering magnet along y-axis was fixed to 1.98 A while varying that applied to the x-axis magnet: **(a)** -3 A, **(b)** -2.66 A, **(c)** -2.33 A, **(d)** -2 A, **(e)** -1.66 A and **(f)** -1.33 A. In this example, configuration **(d)** was chosen for the subsequent irradiations.

of the beam with respect to the fixed collimator could be observed, especially relevant for the preliminary configuration, as shown in Figure 2.11. Therefore, previous to the calibration, different pieces of EBT3 were irradiated for approximately the same time to centre the beam, changing by small steps the current of the steering magnet coils to slightly move the beam and find the conditions that maximised beam homogeneity at the sample position. Figure 2.12 depicts the displacement of the maximum of beam intensity as a function of the steering magnets parameters, measured with the final configuration in Table 2.5.

Following the identification of the best steering magnet parameters, proton dose calibration curves were measured attaching pieces of EBT3 film to the back of the sample holder, and monitoring the fluence by means of the charge readout of the ionisation chamber. Indeed, from the charge Q collected by the ionisation chamber, the incident proton fluence ϕ can be derived as follows:

$$\phi = \frac{1}{A} \cdot \frac{Q \cdot W}{e \cdot \overline{\Delta E}_{\mathrm{IC}}}, \tag{2.2}$$

where A is the area of the collimator placed in front of the chamber, $W = 34\,\mathrm{eV}$ is the ionisation potential of the gas contained in the chamber, $\overline{\Delta E}_{\mathrm{IC}}$ is the mean energy

deposited by individual protons in the ionisation chamber and e is the elementary charge. Knowing the proton fluence, the dose deposited D can be derived with the formula:

$$D = \frac{\overline{\Delta E}_{\mathrm{mat}}}{\Delta x} \cdot f \cdot \phi \cdot \frac{1}{\rho_{\mathrm{mat}}}, \tag{2.3}$$

where $\overline{\Delta E}_{\mathrm{mat}}$ is the mean energy deposited per proton in the thickness Δx of the material considered, ρ_{mat} is its density and f is a correction factor introduced to account for the fluence loss due to the broadening of the beam inside the ionisation chamber. Since the computation of the dose is done under the assumption that the proton fluence does not vary over the sample surface, Equation (2.2) is a further proof of the importance of achieving homogeneous and uniform beam profiles. Finally, to compute $\overline{\Delta E}_{\mathrm{IC}}$, $\overline{\Delta E}_{\mathrm{mat}}$ and f the Monte Carlo simulation, previously validated as described in Section 2.2.2, was used.

2.3 Results

2.3.1 Validation of the Monte Carlo code

In this section, the results obtained for the characterisation and benchmarking of the simulated beam are presented. Firstly, the identification of the best energy distribution is discussed, focusing in particular on the determination of the energy spread of the beam. Secondly, on the other hand, is dedicated to the characterisation of the beam spatial profile.
In both cases, simulation outcomes are compared with experimental measurements, and the final result is considered as that minimising the relative differences between the two. The beam energy and spatial distributions identified from this analysis are then used in all the subsequent application of the Monte Carlo simulation of the external beam line.

Beam energy distribution

With the purpose of characterising the initial energy distribution of the beam, to be implemented in the Monte Carlo simulation, different measurements were carried out as described in Section 2.2.2 and summarised in Table 2.6.
These measurements were then reproduced in various Monte Carlo simulations, initialising the beam as a point-like source with Gaussian energy distribution. A fixed initial proton beam energy of 18 MeV was used for these simulations, changing the initial standard deviation (σ_{i}) from 0.18 MeV (nominal value) to 0.10 MeV in steps of 10 keV. The comparison between experimental and Monte Carlo results is

Table 2.6: Experimental configurations used for the determination of the spectral distribution of the beam, to be compared with the simulations. In all cases the energy was measured with a 5 mm thick calibrated silicon detector at a distance of 22 mm from the exit window, intercepting the beam path with tungsten degraders of various thicknesses. The values of the mean energy and energy spread reported and their errors have been obtained from a Gaussian fit of the experimental energy distributions.

W foil thickness [μm]	measured mean energy (E_{exp}) [MeV]	measured energy spread (σ_{exp}) [MeV]
no foil	17.463(4)	0.143(5)
50	16.135(7)	0.188(6)
100	14.861(2)	0.201(2)
150	13.441(2)	0.232(2)
220	11.201(5)	0.283(4)
270	9.563(6)	0.364(5)
320	7.533(9)	0.402(7)

shown in Figure 2.13 and Figure 2.14.
Deviations of the Monte Carlo mean energy values from experimental ones are generally below 1% and always smaller than the experimental energy spread σ_{exp}, while deviations in energy spread are mostly below 5% and up to 10% in the worst case. From Figure 2.14 it emerges that a Gaussian energy distribution with mean value of 18 MeV and σ_i of 0.14 MeV gives the best agreement between measured and simulated energy spectra.

Beam spatial distribution

After tuning the Monte Carlo simulation to reproduce the initial energy distribution of the beam, its spatial distribution could be characterised. To do so, as described in Section 2.2.2, measurements of the beam profile were performed, placing EBT3 films at different distances from the exit window and in different configurations, listed in Table 2.4. Concerning the simulation, various initial spatial configurations of the beam were considered: circular uniform, circular Gaussian and elliptical Gaussian, with radius or standard deviation varying from 8 mm to 20 mm independently in the two transverse directions.

A first comparison of Monte Carlo simulations with the measured lateral dose profiles is shown in Figure 2.15. In this Figure, the beam spot measured at a distance of 0.5 cm from the exit window (Figure 2.15a) is compared with the simulated ones, starting respectively from a circular uniform beam with radius $r_i = 8$ mm (Figure 2.15b), a circular Gaussian beam with $\sigma_i = 8$ mm (Figure 2.15c) and an elliptical Gaussian beam with $\sigma_{i,x} = 12$ mm and $\sigma_{i,y} = 20$ mm (Figure 2.15d). Figure 2.16 shows the same comparison, where the dose profiles along the two axes have been extracted

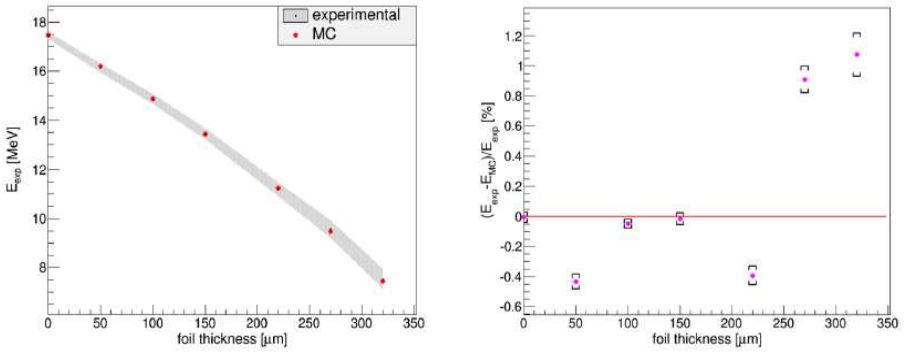

(a) **(b)**

Figure 2.13: **(a)** Comparison between experimental mean energy measured (shaded gray area and black dots) and mean energy obtained from Monte Carlo simulations (red dots) as a function of the foil thickness. The mean energy obtained at the end of the simulation, computed as the energy deposited in the silicon detector, does not depend on the initial σ_{i} of the beam. The energy width of the experimental shaded area is given by σ_{exp}. **(b)** Percentage deviation of the Monte Carlo mean energy ($\mathrm{E_{MC}}$) from the experimental one ($\mathrm{E_{exp}}$). The error bars have been computed with standard uncertainty propagation over the errors associated to the mean energies obtained from the fits.

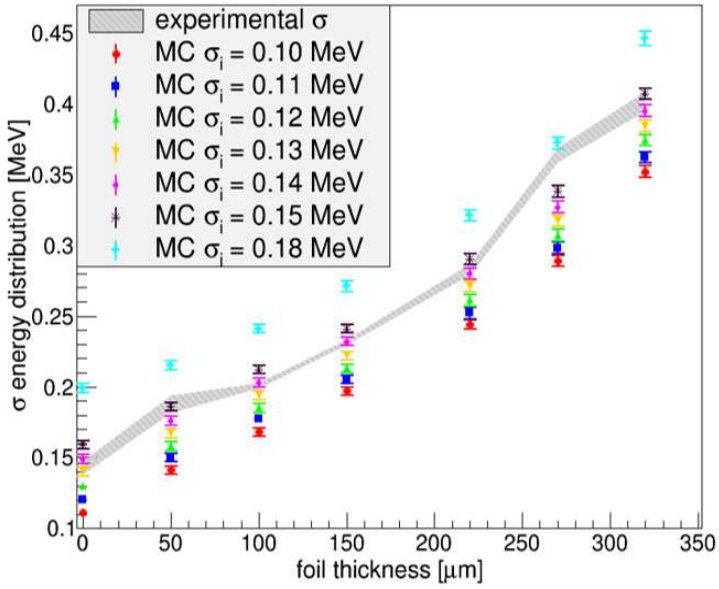

Figure 2.14: Comparison between the experimental σ measured (shaded gray area) and those obtained from the Monte Carlo code run with different initial standard deviations of the Gaussian beam σ_{i}, as a function of the foil thickness. The width of the experimental shaded area is given by the error associated to σ_{exp}.

from the two-dimensional distributions in Figure 2.15 and superimposed, to allow for a better visualisation.

From the visual comparison of measured and Monte Carlo profiles in Figure 2.16, one might conclude that the two-dimensional elliptical Gaussian beam having $\sigma_{i,x} = 12\,\text{mm}$ and $\sigma_{i,y} = 20\,\text{mm}$ is the one that best reproduces the experimental data. However, this is not necessarily the case for all the experimental configurations considered (see Table 2.1). For a better understanding of the performances of the Monte Carlo code in reproducing experimental profiles with varying initial beam spot shapes and sizes, the standard deviations of the simulated final spatial distributions were studied in comparison with the measured ones. The result of this analysis is reported in Figure 2.17 for some of the configurations listed in Table 2.4. In

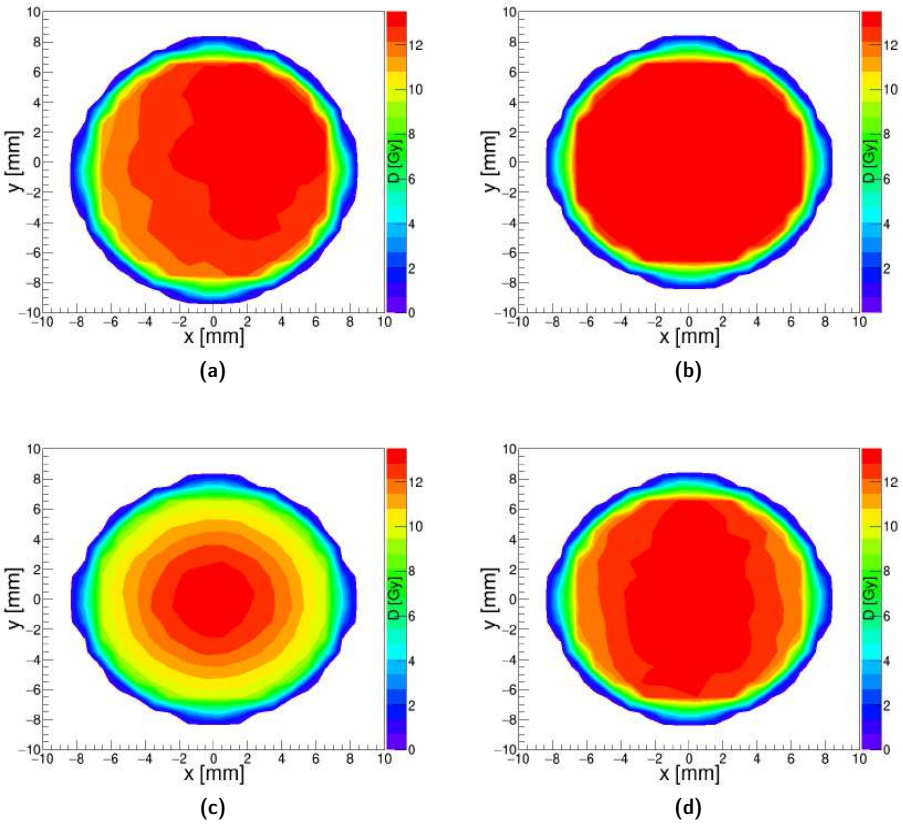

Figure 2.15: Beam spot at a distance of 0.5 cm from the exit window (configuration **B.1** of Table 2.4). The colour scale is in dose units (Gy). **(a)** Measured. **(b)** Simulated with a circular uniform distribution having a radius of 8 mm. **(c)** Simulated with a circular Gaussian distribution having $\sigma_{i,x} = \sigma_{i,y} = 8\,\text{mm}$. **(d)** Beam spot simulated with an elliptical Gaussian distribution having $\sigma_{i,x} = 12\,\text{mm}$ and $\sigma_{i,y} = 20\,\text{mm}$.

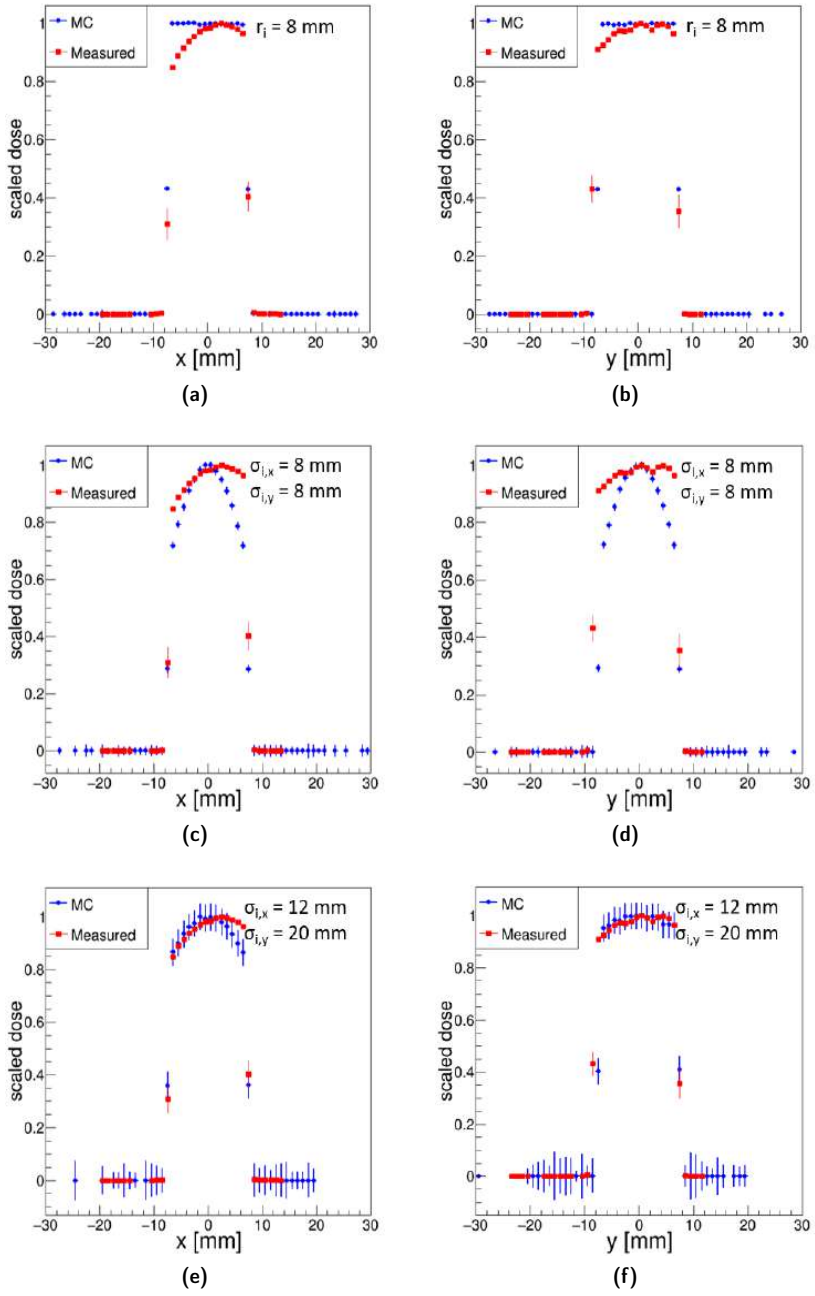

Figure 2.16: Lateral dose profiles along x (left) and y (right) directions, extracted from the measured (red) and Monte Carlo (blue) beam spots plotted in Figure 2.15: **(a)** and **(b)** beam simulated with a circular uniform distribution with radius of 8 mm; **(c)** and **(d)** beam simulated with a circular Gaussian distribution with $\sigma_{i,x} = \sigma_{i,y} = 8$ mm **(e)**, **(f)** beam simulated with a two dimensional Gaussian distribution having $\sigma_{i,x} = 12$ mm and $\sigma_{i,y} = 20$ mm.

this plot, the percentage distance of the Monte Carlo standard deviation of the dose spatial distributions from the experimental one is represented, considering the two extreme cases in terms of initial spatial distribution of the beam: circular Gaussian with $\sigma_{\mathrm{i}} = 8\,\mathrm{mm}$ and uniform with $r_{\mathrm{i}} = 8\,\mathrm{mm}$. Indeed, due to the size of the aluminium fixed collimator, whose radius is equal to 7.5 mm, an upper limit exists in the dimensions of the beam spot achievable, beyond which changes in the initial parameters of the Monte Carlo simulations would not produce any modification in the final result. For the sake of comparison, results obtained with an elliptical Gaussian spot having $\sigma_{\mathrm{i,x}} = 12\,\mathrm{mm}$ and $\sigma_{\mathrm{i,y}} = 20\,\mathrm{mm}$ are also represented, and the points lie between the two extreme cases, as expected.

From Figure 2.17 emerges that, in general, a beam with initial uniform spatial distribution performs better in reproducing measured profiles at least with respect to their standard deviations, especially for the higher proton energies, with deviations mostly below 10% and lower than 5% in the best cases. As the proton energy decreases with the increasing distance from the exit window and the introduction of degraders, the differences between the two Monte Carlo simulations become negligible, because the main contribution to the shape of the final dose profile is given by multiple Coulomb scattering in the materials traversed by the beam. In all cases, however, some small differences could be observed between the experimental and simulated profiles, which most probably were related to the initial in-homogeneity of the beam that is not reproduced in the simulations.

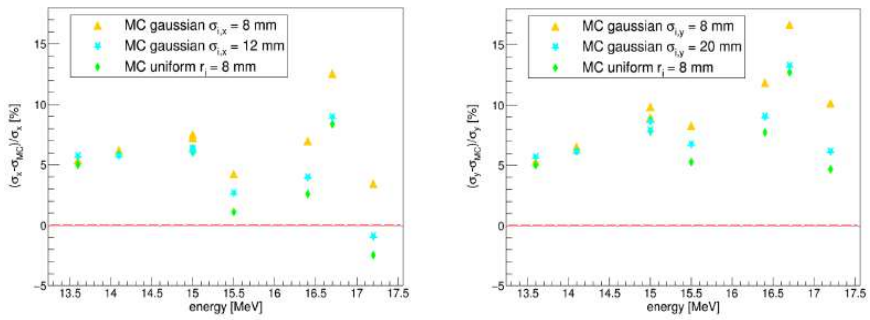

(a) (b)

Figure 2.17: **(a)** Percentage distance of the Monte Carlo standard deviation of dose profiles along the x axis (σ_{MC}) from the experimental one (σ_{x}) as a function of the proton kinetic energy in the active layer of the film. **(b)** Percentage distance of the Monte Carlo standard deviation of dose profiles along the y axis from the experimental one (σ_{y}) as a function of the proton kinetic energy in the active layer of the film. Three initial configurations of the Monte Carlo beam are compared, circular Gaussian with $\sigma_{\mathrm{i,x,y}} = 8\,\mathrm{mm}$ (yellow triangles), elliptical Gaussian with $\sigma_{\mathrm{i,x}} = 12\,\mathrm{mm}$ and $\sigma_{\mathrm{i,y}} = 20\,\mathrm{mm}$ (cyan stars) and circular uniform with $r_{\mathrm{i}} = 8\,\mathrm{mm}$ (green diamonds).

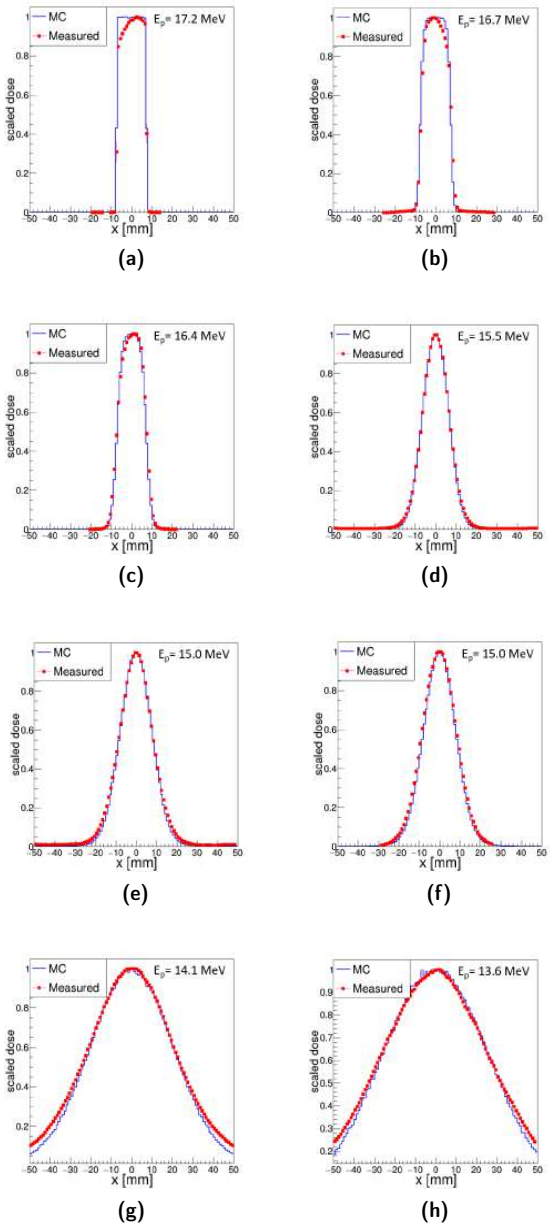

Figure 2.18: Comparison of measured (red) and Monte Carlo dose profiles (blue) along the x-axis, whose standard deviations are those used for the calculation of the percentage distance in Figure 2.17a. The energies reported in the plots refer to the kinetic energy of protons in the active layer of the EBT3 film. For this comparison, Monte Carlo simulations have been performed with an initial circular uniform beam of radius $r_{\mathrm{i}} = 8\,\mathrm{mm}$. The following experimental configurations, listed in Table 2.4, are shown: **(a)** configuration **B.1**; **(b)** configuration **B.3**; **(c)** configuration **B.5**; **(d)** configuration **A.1**; **(e)** configuration **A.2**; **(f)** configuration **B.7**; **(g)** configuration **A.3**; **(h)** configuration **A.4**.

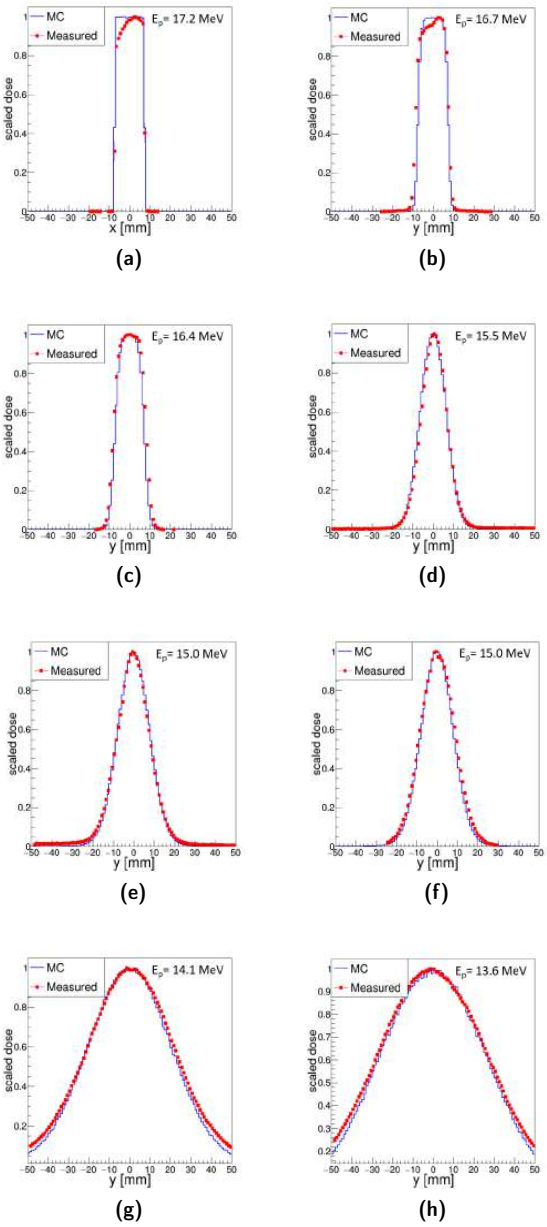

Figure 2.19: Comparison of measured (red) and Monte Carlo dose profiles (blue) along the y-axis, whose standard deviations are those used for the calculation of the percentage distance in Figure 2.17b. The energies reported in the plots refer to the kinetic energy of protons in the active layer of the EBT3 film. For this comparison, Monte Carlo simulations have been performed with an initial circular uniform beam of radius $r_{\mathrm{i}} = 8\,\mathrm{mm}$. The following experimental configurations, listed in Table 2.4, are shown: **(a)** configuration **B.1**; **(b)** configuration **B.3**; **(c)** configuration **B.5**; **(d)** configuration **A.1**; **(e)** configuration **A.2**; **(f)** configuration **B.7**; **(g)** configuration **A.3**; **(h)** configuration **A.4**.

Finally, Figure 2.18 and Figure 2.19 collect the profiles along the x-axis and y-axis, respectively, whose standard deviations are those used in Figure 2.17 for the calculation of percentage distance between experimental data and Monte Carlo simulations. In these plots, experimental profiles (red) are compared with Monte Carlo profiles (blue), obtained with an initial circular uniform beam with radius $r_{\mathrm{i}} = 8\,\mathrm{mm}$. A good agreement is generally observed, which improves as the energy of the incident proton decreases. The worse agreement observed in the tails of the two lower energies is associated to an intrinsic limit of the scanner used for the acquisition of experimental profiles from EBT3 films, whose surface was not big enough to collect the full beam spot.

2.3.2 Optimisation of the setup for the irradiation of cell samples

As described in Section 2.2.3, after the identification of the best steering magnet parameters for the achievement of beam homogeneity, EBT3 proton dose calibration curves were measured for the two configurations listed in Table 2.5, attaching pieces of film to the back of the sample holder. For the preliminary configuration, two different tungsten scattering foil thicknesses were tested:

1. 150 µm, resulting in an average kinetic energy of the proton beam in the active layer of the film of 10.6 MeV with a 0.3 MeV Gaussian standard deviation;

2. 220 µm, corresponding to an average kinetic energy in the active layer of 7.9 MeV with a 0.4 MeV Gaussian standard deviation.

However, very few points were measured with the thicker foil, as the aim of the optimisation process was to obtain the best homogeneity in the sample position while preserving as much as possible the energy of the beam. For the final configuration, on the other side, the beam was scattered with a 500 µm thick aluminium foil inserted in the manipulator of the beam line, resulting in a beam energy of 12.8 MeV with a 0.2 MeV Gaussian standard deviation.
All the irradiations presented in this section took from 10 seconds to 6 minutes maximum, resulting in an average dose rate of approximately $2 - 3\,\mathrm{Gy\,min^{-1}}$ for the preliminary setup and of approximately $5\,\mathrm{Gy\,min^{-1}}$ for the final one.

In order to calibrate EBT3 films under proton irradiation, for the different energies considered, the irradiated films were scanned and the images converted from colour value to net optical density, with the aim of extracting an average netOD value relative to the whole irradiated area. In this process, beam homogeneity played a major role. To check beam homogeneity and highlight the possible presence of gradients, maps of the relative difference of netOD values from the average ($\mathrm{netOD_\mu}$), computed pixel by pixel, were built. Some of these maps are shown in Figure 2.20.

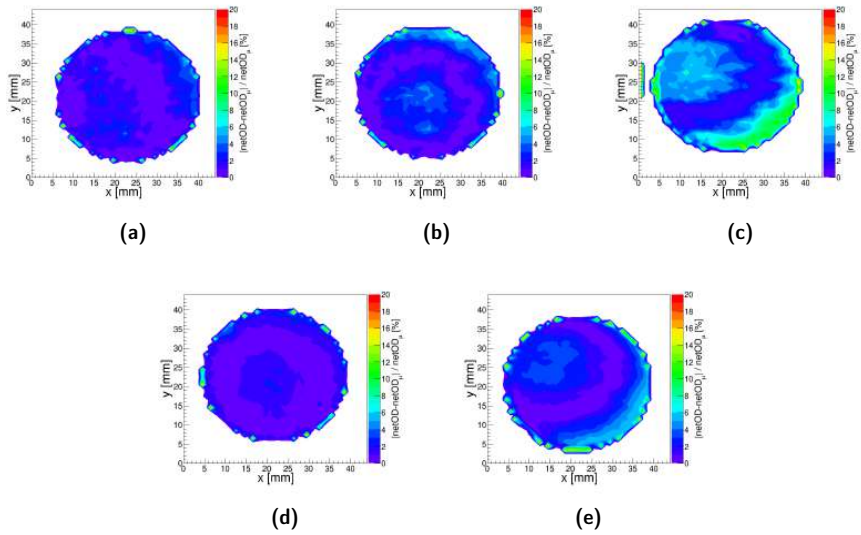

Figure 2.20: Maps of the relative percentage deviation of the netOD computed in each pixel from the average value ($|\text{netOD} - \text{netOD}_\mu|/\text{netOD}_\mu$). **(a)** Preliminary configuration with a tungsten foil of 220 µm, lot of films #1, $\text{netOD}_\mu = 0.20$. **(b)** Preliminary configuration with a tungsten foil of 150 µm, lot of films #1, $\text{netOD}_\mu = 0.19$. **(c)** Final configuration, lot of films #2, $\text{netOD}_\mu = 0.16$. **(d)** Preliminary configuration with a tungsten foil of 150 µm, lot of films #1, $\text{netOD}_\mu = 0.58$. **(e)** Final configuration, lot of films #2, $\text{netOD}_\mu = 0.58$.

In general, average relative deviations from netOD_μ lower than 4% were observed in all the samples, with localised maximum differences up to 20%, usually found in small spikes close to the edges of the irradiated area.

For the computation of the dose, the validated Monte Carlo simulation of the beam line was used to derive the mean energies deposited in the ionisation chamber ($\overline{\Delta E}_{\text{IC}}$) and in the active layer of the film ($\overline{\Delta E}_{\text{AL}}$), and the fluence fraction (f) of particles impinging on the film, to be inserted in Equation (2.2) and (2.3). Table 2.7 collects the values of these quantities for the different experimental configurations considered, extracted from the Monte Carlo distributions shown in Figure 2.21.

From the netOD_μ values measured and the computed doses, calibration curves for the three colour channels were obtained and fitted with Equation (2.1). The resulting curves are depicted in Figure 2.22 and compared to the respective photon calibration curves depending on the film lot, while fit parameters are listed in Table 2.8.

As expected [92,93], a dependence of proton calibration curves on the energy emerged. For the purpose of observing better this effect, independently from the lot of films considered, a plot of the relative difference of proton calibration curves from photon ones as a function of the netOD has been built and is shown in Figure 2.23. In this plot, for the highest incident proton kinetic energy (12.8 MeV) the relative difference

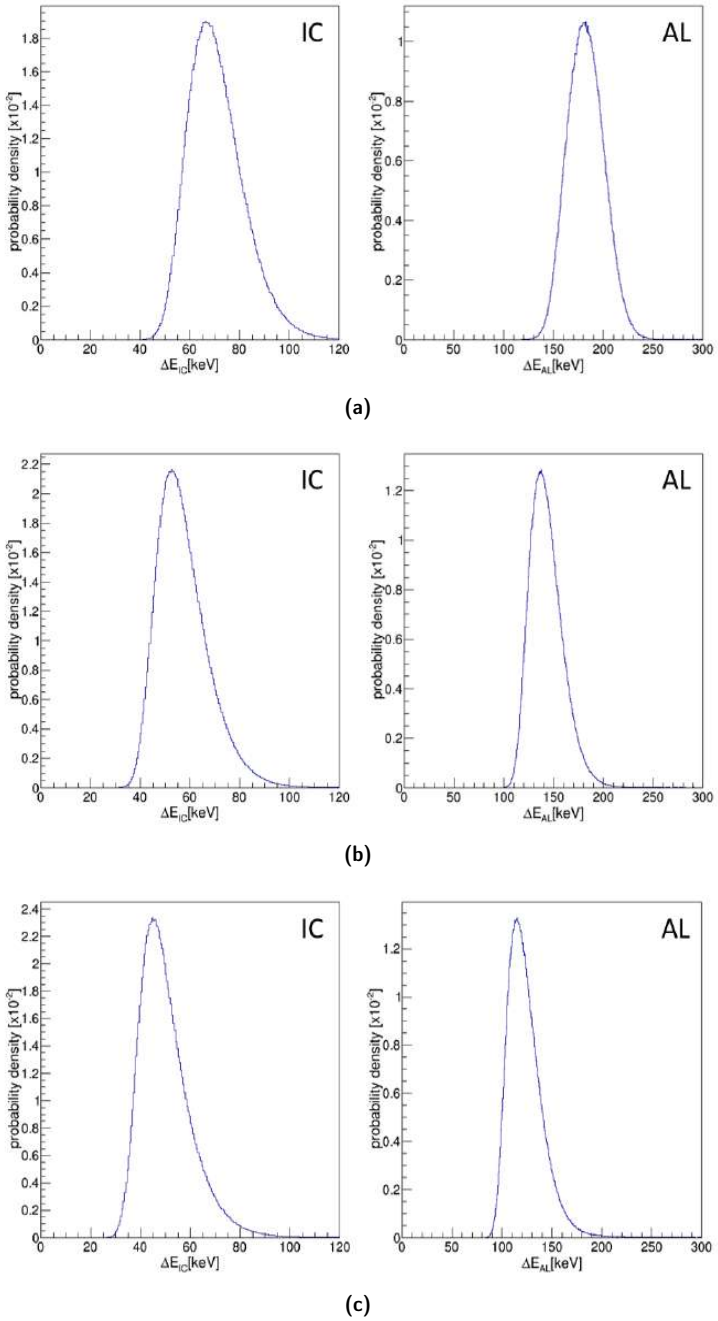

Figure 2.21: Distribution of energy deposited per individual proton track in the ionisation chamber ΔE_{IC} (left) and in the active layer of the film ΔE_{AL} (right). **(a)** Preliminary configuration with tungsten scattering foil of 220 µm; **(b)** preliminary configuration with tungsten scattering foil of 150 µm; **(c)** final configuration. Mean values and standard deviations of the distributions are listed in Table 2.7.

Table 2.7: Mean values and associated standard deviations obtained from the distributions shown in Figure 2.21. E_{kin} is the kinetic energy of the protons in the centre of the active layer of the film, $\overline{\Delta E}_{\mathrm{IC}}$ is the average energy deposited by protons in the ionisation chamber, $\overline{\Delta E}_{\mathrm{AL}}$ is the average energy deposited by protons in the active layer of the film and f is the fraction of protons that reaches the film after having crossed the ionisation chamber.

Configuration	E_{kin} [MeV]	$\overline{\Delta E}_{\mathrm{IC}}$ [keV]	$\overline{\Delta E}_{\mathrm{AL}}$ [keV]	f
Preliminary (220 µm W)	7.9 ± 0.4	70.8 ± 0.6	183.4 ± 0.7	0.93
Preliminary (150 µm W)	10.6 ± 0.3	57.3 ± 0.6	144.0 ± 0.7	0.93
Final	12.8 ± 0.2	50.4 ± 0.6	125.1 ± 0.8	0.98

increases slowly with the netOD, with values varying from 8% to 10% in the [0,0.7] netOD range. For the lower energetic protons (10.6 MeV) on the other hand, this relative difference increases steeply in the [0,0.4] netOD range, going from 15% to 30%, reaches a maximum and then decreases again.

2.4 Discussion

In this chapter, the experimental setup for the irradiation of biological samples, designed for the cyclotron experimental beam line installed at the CNA, has been presented. The main advantage of using an 18 MeV proton beam relies in the possibility of achieving energy distributions with mean values corresponding to the Bragg peak region of a clinical proton beam with a much lower energy spread. As a drawback, however, the range of applicability of such a beam is limited to experiments with mono-layer cell cultures, for which the energy and the stopping power of protons reaching the cells can be calculated accurately. Indeed, for floating cell culture experiments, beam energy degradation along the culture itself would have to be taken into account, leading to a high variability of the stopping power in depth within the sample and subsequently to higher uncertainties in the deposited dose.

In order to achieve dose homogeneity over the irradiated samples with a manageable dose rate (around 2 Gy min^{-1}), the beam intensity was decreased by lowering as much as possible the extraction current of the cyclotron and by turning off all the magnets for beam optics. A further decrease in the beam intensity, as well as a broadening of the beam profile, was obtained by intercepting the beam path with scattering foils of different materials and thicknesses, and by varying the distance between the exit flange and the position of the samples. Two different setups were tested: a preliminary one, where the beam was broadened in air by attaching tungsten foils of 150 µm or 220 µm to the exit flange; and the final one, where the beam was scattered

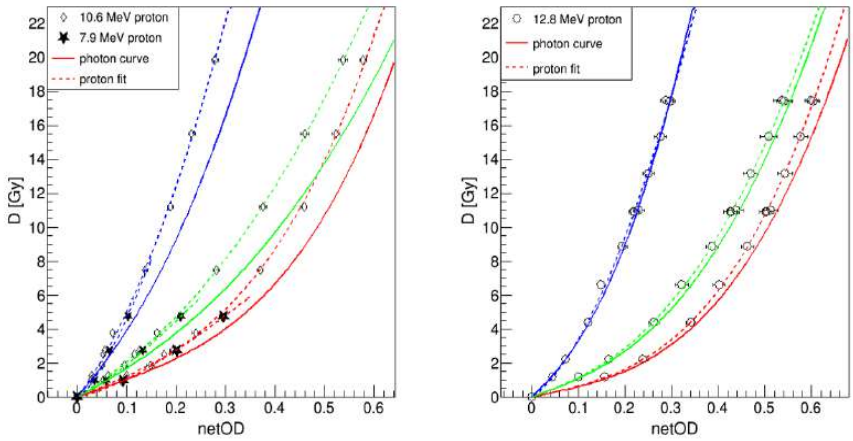

Figure 2.22: Dose-to-netOD calibration curves for the three colour channels. Experimental data are presented together with their fit (dashed line) and compared with the corresponding photon calibration curves (solid lines). Fit parameters are reported in Table 2.8. On the left experimental data obtained with both preliminary configurations (lot #1) are plot: (1) beam broadened with a 150 µm tungsten foil (empty diamonds) and (2) with a 220 µm tungsten foil (full stars). On the right the experimental data obtained with the final configuration (empty circles) are presented. The energies indicated in the legend are the same E_{kin} listed in Table 2.7

Table 2.8: Results obtained for the parameters of Equation (2.1) from the fit of the data in Figure 2.22 for the three colour channels and the different experimental configurations. Since in the range covered by the measurements performed with the 220 µm tungsten foil (stars of Figure 2.22) the dose is mostly a power of the netOD, parameter a has been set equal to zero for the three channels.

Configuration	Parameter	Red Channel	Green Channel	Blue Channel
Preliminary	a [Gy]	0	0	0
$E_{\text{kin}} = 7.9\,\text{MeV}$	b [Gy]	25 ± 2	33 ± 3	120 ± 40
(lot #1)	c	1.38 ± 0.04	1.23 ± 0.05	1.4 ± 0.1
Preliminary	a [Gy]	11.8 ± 0.4	19 ± 1	39 ± 8
$E_{\text{kin}} = 10.6\,\text{MeV}$	b [Gy]	70 ± 7	41 ± 6	120 ± 60
(lot #1)	c	3.1 ± 0.2	2.3 ± 0.3	2.0 ± 0.5
Final	a [Gy]	5.9 ± 0.9	10 ± 2	20 ± 10
$E_{\text{kin}} = 12.8\,\text{MeV}$	b [Gy]	65 ± 9	60 ± 10	110 ± 30
(lot #2)	c	3.1 ± 0.3	2.6 ± 0.3	1.8 ± 0.4

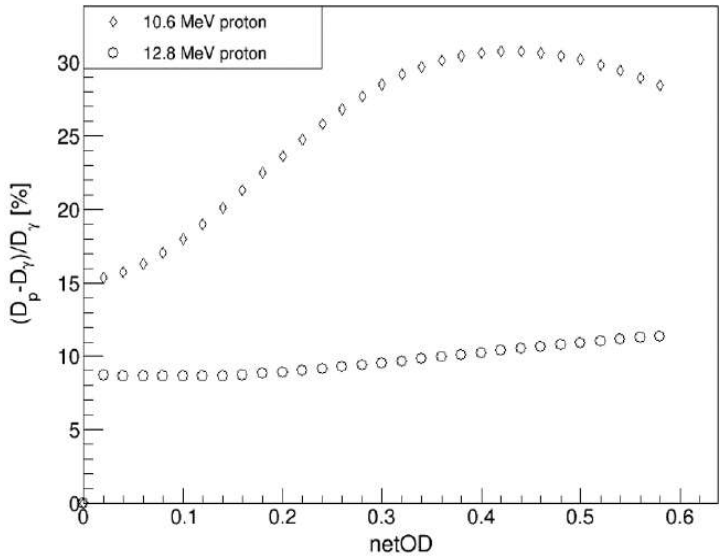

Figure 2.23: Relative difference of the proton dose (D_p) from the photon dose (D_γ), evaluated with the respective calibration curves, as a function of the netOD. For the more energetic incident protons (12.8 MeV, circles) this relative difference increases slowly and its value lays between 8% and 10%. For the 10.6 MeV, on the other hand, the relative difference increases steeply, reaches a maximum at a netOD of around 0.4, and decreases again, varying from 15% to 30%.

by means of a 500 µm thick aluminium foil inserted in the manipulator mounted 2 m upstream the exit flange. Further, for dosimetry purposes, the geometry of the beam line and the irradiation setup were implemented in Geant4, developing a dedicated Monte Carlo application which was validated and benchmarked towards comparison with experimental data.

Validation of the Monte Carlo code Measurements of beam energy and shape were performed with a lithium-drifted silicon detector and EBT3 films, to be compared with Monte Carlo simulations for the validation of the code. In order to determine the initial Monte Carlo beam characteristics, multiple simulations were run changing by small steps and one at a time different parameters, such as energy spread and shape of the spatial distribution, to find the set of parameters that better reproduced experimental data.

An initial proton beam energy of 18 MeV with a Gaussian energy spread of 0.14 MeV gave the best agreement between experimental and simulated results, with percentage deviations generally lower than 1%. The highest discordances between measurements and Monte Carlo, relatively to the energy distribution, were observed for the thicker tungsten foils used to degrade the beam, as can be seen in Figure 2.13. This result

could have been influenced by two different factors: the lower statistics collected experimentally for these points and the uncertainty associated to the thickness of the foil, reported to be up to 10% by the manufacturer.

Regarding the reproducibility of lateral dose profiles, a circular uniform Monte Carlo beam spot, having radius $r_i = 8\,\text{mm}$, gave the best agreement with the experimental profiles measured with EBT3 films. The asymmetry in some of the measured dose profiles, especially those detected at a closer distance from the exit window, was not reproduced by the Monte Carlo simulation, since it was probably related to an initial misalignment of the beam coming from the cyclotron. This effect, which could be partially corrected by resorting to the steering magnets of the beam line, fades away as the distance from the exit window increases and the broadening due to multiple Coulomb scattering in air becomes predominant. In general, differences between simulated and measured profiles were mostly below 10%, being usually Monte Carlo beam spots slightly smaller than experimental ones. These differences arose probably from the calibration curve used to scale measured netOD profiles to dose. Indeed, photon dose calibration curves were used to this purpose in the first approximation. However, since the quenching effect observed in EBT3 films under proton radiation decreases as the proton energy increases, the "true" calibration curves for the energies considered (between 13.6 and 18 MeV) are expected to lay between the 12.8 MeV proton curve and the photon one shown in Figure 2.22, and the quenching effect is expected to be negligible.

Optimisation of the setup for the irradiation of cell samples A homogeneous lateral dose profile is beneficial in cell experiments, to ensure that the dose stays constant throughout the culture dish at a given depth. With both setups tested for the irradiation of biological samples, preliminary and final, average relative deviations from homogeneity lower than 4% were observed, with some localised maximum differences up to 20% located at the edges of the irradiated area. In Figure 2.20c, a gradient exists in the netOD profile obtained with the final configuration, whose deviation from homogeneity is still below 10% and decreases as the netOD increases, as can be seen by comparing for example with Figure 2.20e. This behaviour is probably related to the fact that, without any degradation in air with tungsten foils, the residual misalignment of the beam might still be visible in the sample, as the beam undergoes less divergence (see Figure 2.11). For this reason the initial alignment with steering magnets is crucial and must be performed before every experimental campaign, since the coil parameters that give the best alignment are not always reproducible. Furthermore, some evidences emerged, depicted in Figure 2.24, suggesting that the beam suffered a small drifting in time within the same experimental campaign, as the coils of the steering magnets heated up with

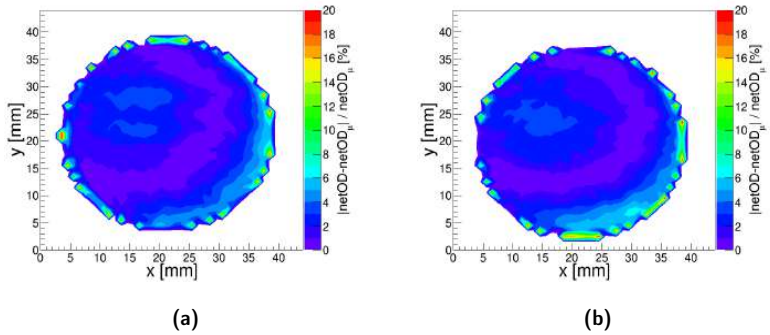

Figure 2.24: Maps of the relative percentage deviation from homogeneity of two samples having the same netOD$\mu = 0.60$, but measured at the beginning **(a)** and at the end **(b)** of the experimental campaign at a distance of approximately two hours.

use, determining a displacement of the beam maximum intensity. Even if this effect can be considered negligible for the film calibration and computation of the dose, it must be taken into account, and minimised when it comes to the irradiation of biological samples. Therefore, a check on beam homogeneity and a setting of the steering magnet parameters is strongly recommended before and after any irradiation of biological material.

After assuring the beam homogeneity over the sample, EBT3 films were calibrated under proton irradiation and the resulting curves compared with photon ones. A dependence on the proton energy emerged, resulting in a progressive distancing of proton curves from photon ones, leading to a lower darkening of the film for the same level of absorbed dose and thus to a lower sensitivity. To study the effect of the proton energy on the calibration curve, independently from the film lot considered, the relative difference of the predicted proton dose from the photon one was plotted as a function of the netOD (see Figure 2.23). While for the more energetic protons the relative distance between the curves remains almost constant, with a small increase towards higher netOD values, for the lower energetic protons this distance increases steeply up to a maximum at a netOD of around 0.4, and then decreases. This behaviour is probably related to two factors: the quenching effect triggered by the lower energetic protons of the incident kinetic energy distribution, and the saturation of the film response to high doses.

Finally, dose rates of approximately $2 - 3\,\mathrm{Gy\,min^{-1}}$ and $5\,\mathrm{Gy\,min^{-1}}$ were obtained for the preliminary and final setup, respectively. The slightly higher dose rate of the final setup was probably influenced by the material of the scattering foil used. Indeed, the atomic number of aluminium is much smaller than that of tungsten ($Z_{\mathrm{Al}} = 13$ and $Z_{\mathrm{W}} = 74$), determining a smaller multiple Coulomb scattering effect

and therefore a reduced beam loss in the different collimators constituting the beam line and the experimental setup. Furthermore, the beam settings and intensities are subject to variations from one irradiation to another, affecting the reproducibility of the dose rate.

2.5 Conclusions

A beam line diagnostic and irradiation scheme, based on a completely defocused beam, a 500 µm thick aluminium scattering foil and an ionisation chamber coupled with EBT3 radiochromic films, was identified as the best setup for the irradiation of mono-layer cell cultures at the external beam line of the CNA cyclotron facility. With this setup, a homogeneous irradiation field was achieved, with average deviations from homogeneity lower than 4% in the whole sample area (3.5 cm diameter) for a beam energy of 12.8 MeV and a dose rate of about $5 - 6\,\mathrm{Gy\,min^{-1}}$.

A specific Monte Carlo simulation was built and developed to reproduce the beam line and the experimental setup, using the Geant4 Monte Carlo code. Simulations were tested towards experimental measurements and reproduced experimental data in what concerned the beam energy distribution and dose profiles with differences lower than 1% and 10%, respectively.

From the setup just described, in principle, lower proton energies with higher levels of homogeneity over the sample surface and lower dose rates could be easily achieved, by further degrading the beam with scattering foils of different materials and thicknesses and by changing the exit window to sample distance. On the other side, a proton beam energy distribution with a higher average value ($12.8\,\mathrm{MeV} < E_{\mathrm{kin}} < 18\,\mathrm{MeV}$) could probably be obtained by increasing the atomic number of the scattering foil material in the manipulator while decreasing its thickness.

Finally, in Chapter 4, the first irradiations of mono-layer cell cultures performed in the cyclotron radiobiology beam line will be presented.

Chapter 3

Microdosimetry-based dose-averaged linear energy transfer calculation for mono-energetic proton beams: a Monte Carlo study with GEANT4-DNA

3.1 Introduction

Many radiobiological effects of ionising radiation can be traced back to the microscopic spatial distribution of energy deposition in irradiated media, whose stochastic nature is described quantitatively with the formalism of microdosimetry. Consequently, in recent years several studies have turned to the framework of microdosimetry to approach problems such as the characterisation of LET distributions for radiotherapy beams and the determination of their RBE.

In view of the growing awareness of the variations or proton RBE with increasing LET at the distal Bragg peak region [109–111], recent studies aim at including LET and/or dose-averaged LET (L_{D}) objective functions in treatment planning optimisation [112, 113], taking advantage of the monotonic dependence of the RBE on LET for clinical proton beams.

Microdosimetry, on one hand, permits the calculation of RBE from a microscopic approach by means of the Microdosimetric-Kinetic Model (MKM) [69–71] and, on the other hand, provides physical concepts and computational tools to calculate

macroscopic L_{D} distributions. The microscopic analogue of the LET is called lineal energy (y, see Chapter 1), which is a stochastic quantity that accounts for the energy imparted per unit length to a certain sensitive volume, called site, by an incident particle and all its secondary products. Macroscopic distributions of LET and microscopic distributions of y can be biologically characterised by their dose-weighted averages, $\overline{L}_{\mathrm{D}}$ and $\overline{y}_{\mathrm{D}}$, which are especially relevant when the incident beam is composed by particles of different LET. The difference between these two distributions is given by the straggling, which can be accounted for by considering the weighted average δ_2 of the energy imparted per collision ε_{c} of the traversing beam (see Section 3.2). The mathematical description of this relation was given by Kellerer, and can be used to extract the macroscopic dose-averaged LET of a beam from its microdosimetric distributions [66–68].

The calculation of microdosimetric distributions and their moments can be carried out both analytically or by means of Monte Carlo simulations. In this chapter, a track structure Monte Carlo application, developed for the computation of microdosimetric distributions of protons in liquid water, is presented. This application, based on Geant4-DNA, provides two sampling methods, *uniform* and *weighted*, for the computation of the microdosimetric quantities of interest in spherical sites, with diameters ranging from 1 to 10 µm. Besides the distribution of energy imparted per single event, the code computes also the distribution of the energy imparted to the site per electronic collision of the proton, which has never been included in any of the microdosimetry examples in the official release of Geant4.
Following the description of the geometry and the sampling algorithm implemented, results obtained for microdosimetric distributions for different site sizes and energies are presented. Finally, the code is tested and benchmarked by computing the dose-averaged LET with the formula proposed by Kellerer and comparing it with the macroscopic one.

3.2 Theoretical Framework

There are often serious limitations to the use of LET for the description of the biological effect of different radiation qualities. Firstly, particles with different charges and different energies can have the same LET. However, the particle energy, mass and charge are what determine the spectral distribution of delta rays, which play a major role in the spatial distribution of the energy. Secondly, the LET does not take into account the length of the track relative to a finite target structure, which is especially relevant for low energies or large sites. Finally and more importantly, the LET does not consider the random nature of energy loss along the track. Consequently, the LET, which is defined as the *mean* energy lost by a charged particle per unit path

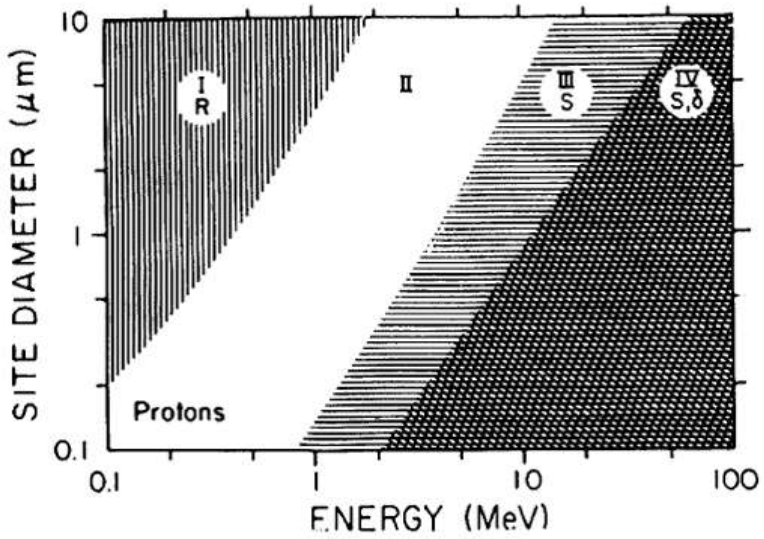

Figure 3.1: Ranges of site diameters and proton energies in which other factors in addition to LET influence the energy deposition. The symbols R, S and δ identify, respectively, the domains where limited particle range, energy-loss straggling and δ-ray escape or influx are relevant. In the remaining region (II), the deposition of energy is approximately proportional to the (unrestricted) LET [114].

length and, therefore, accounts for a large number of electronic collisions, cannot express the features of a given distribution of energy imparted per event to a small sensitive volume, which frequently arises form a small number of collisions [65].

The effects of these limitations, and the ranges of proton energies and diameter sites (in the hypothesis of traversal or partial traversal of a microscopic spherical site) in which they are relevant to energy deposition, were illustrated by Kellerer and Chmelevsky [114] and are summarised in Figure 3.1. This Figure shows that in a substantial range of site diameters and particle energies (region II), the LET concept is appropriate and can be applied without consideration of additional factors. However, moving to larger site diameters or smaller particle energies (region I), the limited range of particles strongly influences the energy deposition, since the LET may change significantly along the path through the site and the track might even begin or end in the site. On the other hand, moving to small site diameters and larger particle energies, energy straggling (regions III and IV) and eventually δ-rays influx and escape (region IV) play an important role.

The interplay of the various factors affecting the energy deposition in cellular or sub-cellular regions and their contribution to the macroscopic dose-averaged LET (L_{D}) are discussed in the following sections. The reason for using $\overline{L}_{\mathrm{D}}$, according to dual radiation action theory, is that biological damage is related to the amount of

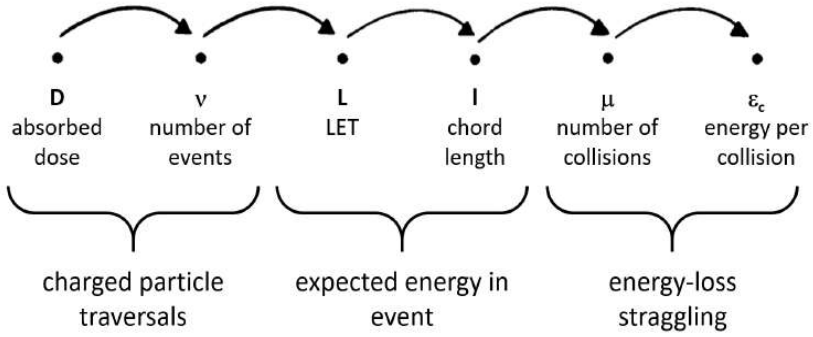

Figure 3.2: Chain or random factors that determine the energy deposition in a site [68].

energy imparted and the spatial concentration of this energy, being $\overline{L}_{\mathrm{D}}$ simultaneously representative of both [115].

3.2.1 Obtaining dose-averaged LET from microdosimetry

As mentioned above, if the medium is exposed to an absorbed dose D the energy imparted to a specified site is determined by a chain or random factors. In the specific case of short track segments, i.e., site dimensions considerably smaller than the particle range so that the LET can be considered constant, these factors are represented in Figure 3.2. The first random variable, ν, is the number of events, i.e., the number of independent charged particles traversing the region, which follow a Poisson distribution. The second random variable, L, is the LET of the ionising particle in the medium, which, if the range of the most energetic δ-rays is comparable to or greater than the size of the region, is to be considered as restricted. Looking at the problem microscopically, an ionising particle can traverse the site from a random direction. The length of the particle track within the site is the fourth random variable, l, called chord length. In the case of straight tracks within the site, the mean chord length is defined as the mean length of randomly oriented chords in the site [65].

The expected energy imparted by an event to a site is the product of the frequency-averaged LET, $\overline{L}_{\mathrm{F}}$, of the particle and the mean chord length $\bar{l}_{\mathrm{F}}$ in the site, $\bar{\epsilon}_{\mathrm{F}} = \overline{L}_{\mathrm{F}} \cdot \bar{l}_{F}$, where the subscript s used in Section 1.3.3 to indicate the single event distribution has been omitted to ease the notation. Due to the energy-loss straggling, the actual energy imparted to the site of interest deviates from the product of the chord length and the restricted LET, and it is influenced by the two last random factors: the number μ of collisions along the chord and the energy lost in each collision ε_{c}.

The influence of the different random factors on the single-event distribution can

be considered in terms of the relative variance of the different quantities, i.e., the variance divided by the square of the mean:

$$V_x = \frac{\sigma_x^2}{\overline{x}^2} = \frac{\overline{x^2} - \overline{x}^2}{\overline{x}^2} = \frac{\overline{x}_\mathrm{D}}{\overline{x}_\mathrm{F}} - 1, \tag{3.1}$$

where

$$\overline{x}_\mathrm{F} = \int x f(x)\,\mathrm{d}x \tag{3.2}$$

is the frequency average of the quantity x and

$$\overline{x}_\mathrm{D} = \int x d(x)\,\mathrm{d}x = \frac{1}{\overline{x}_\mathrm{F}} \int x^2 f(x)\,\mathrm{d}x \tag{3.3}$$

is its weighted average. Under the condition of short track segments, the variance of the single-event spectrum (V_ϵ) is given by [67]:

$$V_\epsilon = V_\mathrm{LET} + V_\mathrm{l} + V_\mathrm{l} \cdot V_\mathrm{LET} + V_\mathrm{S}, \tag{3.4}$$

where V_LET, V_l and V_S are the relative variances of the distributions of LET, chord length and energy straggling, respectively. While LET and chord length distributions present no particular difficulties in the calculation of the single-event spectrum, the straggling problem is complicated in microdosimetry by the fact that the interest rotates around the distribution of energy deposition by a particle and not around the distribution of energy loss. The escape and influx of δ-rays from and into the region of interest presents considerable theoretical difficulties, and the problem needs to be studied by Monte Carlo simulations of δ-ray tracks [67]. The straggling distribution reflects the succession of statistically independent collision events of varying size and is therefore the solution of a compound Poisson process:

$$s(\varepsilon_\mathrm{c}; \overline{\epsilon}_\mathrm{F}) = \sum_{\mu=0}^{\infty} \mathrm{e}^{-n} \frac{n^\mu}{\mu!} \cdot w^{*\mu}(\varepsilon_\mathrm{c}), \tag{3.5}$$

where $n = \overline{\epsilon}_\mathrm{F}/\overline{\varepsilon}_\mathrm{c}$ and $w^{*\mu}(\varepsilon_\mathrm{c})$ is the μ-fold convolution product of $w(\varepsilon_\mathrm{c})$, the probability distribution of energy transfers in the collisions encountered by the charged particles. Defining the weighted average of the $w(\varepsilon_\mathrm{c})$ distribution as:

$$\delta_2 = \overline{\varepsilon}_\mathrm{c} \left(1 + \frac{\sigma_{\varepsilon_\mathrm{c}}^2}{\overline{\varepsilon}_\mathrm{c}^2}\right), \tag{3.6}$$

the relative variance of the straggling distribution can be demonstrated to be equal to [66]:

$$V_{\mathrm{S}} = \frac{\delta_2}{\bar{\epsilon}_{\mathrm{F}}}. \tag{3.7}$$

Consequently, from Equation (3.4), the following formula can be obtained:

$$\frac{\bar{\epsilon}_{\mathrm{D}}}{\bar{\epsilon}_{\mathrm{F}}} = \left(\frac{\overline{L}_{\mathrm{D}}}{\overline{L}_{\mathrm{F}}} - 1\right)\left(\frac{\bar{l}_{\mathrm{D}}}{\bar{l}_{\mathrm{F}}}\right) + \frac{\bar{l}_{\mathrm{D}}}{\bar{l}_{\mathrm{F}}} + \frac{\delta_2}{\bar{\epsilon}_{\mathrm{F}}}. \tag{3.8}$$

According to the definition of lineal energy y, the frequency-averaged lineal energy and the frequency-averaged LET coincide as long as the short track segment condition is met: $\overline{y}_{\mathrm{F}} = \overline{\epsilon_{\mathrm{F}}}/\bar{l}_{\mathrm{F}} = \overline{L}_{\mathrm{F}}$. By using the previous relations, and considering that $\overline{y}_{\mathrm{D}} = \bar{\epsilon}_{\mathrm{D}}/\bar{l}_{\mathrm{F}}$, the derivation of the subsequent relation for the dose-averaged LET is straightforward:

$$\overline{L}_{\mathrm{D}} = \overline{y}_{\mathrm{D}}\frac{\bar{l}_{\mathrm{F}}}{\bar{l}_{\mathrm{D}}} - \frac{\delta_2}{\bar{l}_{\mathrm{D}}}. \tag{3.9}$$

From Equation (3.9) emerges the link between macroscopic and microscopic quantities in the short track segment approximation. Therefore, to obtain the dose-averaged LET of a particular composite beam the microdosimetric quantities $\overline{y}_{\mathrm{D}}$, δ_2 and the chord length distributions must be evaluated, operation that can be carried out by means of Monte Carlo track structure simulations.

3.2.2 Sampling methods and their influence on chord length distributions

In order to calculate the various microdosimetric quantities in Equation (3.9) through Monte Carlo track structure simulations, a particle track needs to be simulated and sampled, i.e., a site must be placed in such a way that at least one energy deposit is produced inside it. There are different types of randomness for the interception of a convex body by straight lines; in the following two types will be distinguished [116]:

isotropic uniform randomness , that results when the body is exposed to a uniform isotropic fluence of infinite straight lines;

weighted randomness , that results when a uniformly distributed random point is chosen in the body and that point is traversed by a straight line with uniform random direction.

From a computational point of view, uniform sampling consists in randomly selecting a position for the center of the site within the region of interest, while weighted sampling consists in selecting an energy transfer point and then placing a site randomly around it. While the first method can be computationally inefficient, as

the chances of selecting areas with no energy imparted to them are really high, the second ensures the occurrence of at least one energy transfer within the site and is more suitable for Monte Carlo track structure calculations. The term *weighted* in this context refers to the fact that the probability of selecting a point centred at a certain elementary volume dV is not uniform but weighted by a factor, determined by the fact that in a particle track the density of transfer points is not uniform. Therefore, in order to obtain the correct frequency single-event distributions a compensation factor must be applied, which is in general inversely proportional to the probability of selecting a certain transfer point, as explained in Section 3.3.2.

The chord length is a stochastic quantity that depends on the geometry of the site and on its position with respect to the particle track core. Therefore, the chord length distributions are influenced by the sampling method chosen. In the case of spherical sites and straight particle tracks, following the short track segment condition, the chord length distributions are well known [116].

The situation in which a particle traverses the site in a completely random way is known as μ-randomness and, in this case, the frequency chord length distribution is given by $f_\mu(l) = 2l/d^2$, where d is the site diameter. This kind of randomness applies in experimental microdosimetry and clinical radiation therapy, where targets are uniformly irradiated from the exterior.

However, when the same track is sampled through weighted sampling, it is set to pass through a specific point inside the site and is not coming from a random point in the exterior anymore. This kind of randomness is known as ν-randomness and its frequency chord length distribution is given by $f_\nu(l) = 3l^2/d^3$. Table 3.1 collects the relations of interest for the chord lengths distributions for both types of randomness.

Table 3.1: Relations of interest for the chord length distributions depending on the type of randomness.

μ-randomness	ν-randomness
$f_\mu(l) = 2l/d^2$	$f_\nu(l) = 3l^2/d^3$
$l_{\mathrm{F}}^{\mu} = 2d/3$	$l_{\mathrm{F}}^{\nu} = 3d/4$
$l_{\mathrm{D}}^{\mu} = 3d/4$	$l_{\mathrm{D}}^{\nu} = 4d/5$

Following the previous considerations, the relation between $\overline{L}_{\mathrm{D}}$ and $\overline{y}_{\mathrm{D}}$ is also affected by the type of randomness, and the formula in Equation (3.9) assumes the form

$$\overline{L}_{\mathrm{D}} = \frac{8}{9}\overline{y}_{\mathrm{D}} - \frac{4\delta_2}{3d} \tag{3.10}$$

for μ-randomness, and

$$\overline{L}_{\mathrm{D}} = \frac{15}{16}\overline{y}_{\mathrm{D}} - \frac{5\delta_2}{4d} \tag{3.11}$$

for ν-randomness, where $\overline{y}_{\mathrm{D}}$ is defined with the mean chord length of the respective randomness type. Straggling, on its side, is an independent factor from LET and chord length, and its distribution should not be affected by them and by the sampling method considered.

3.2.3 Macroscopic dose-averaged LET calculation method

From a macroscopic point of view, the calculation of restricted and unrestricted dose-averaged LET distributions in clinical proton beams can be carried out either by means of analytical models or by Monte Carlo simulations. In both cases, calculations are usually based on the spectral fluence evaluation of primary and, sometimes, secondary particles composing the beam.

In the case of Monte Carlo simulations, a step-by-step approach can be followed in the computation of LET, using the true step length and the electronic energy loss at that step. Different Monte Carlo algorithms for the computation of L_{D}, based on a condensed history method, were compared by Cortés-Giraldo and Carabe [117] using Geant4, to test their robustness towards the variation of different parameters. The following method:

$$\overline{L}_{\mathrm{D}} = \frac{\sum_{n=1}^{N}\sum_{s=1}^{S_n}\omega_n L_{sn}\varepsilon_{sn}}{\sum_{n=1}^{N}\sum_{s=1}^{S_n}\omega_n\varepsilon_{sn}} \tag{3.12}$$

was identified as the one giving the most consistent performances, being n and s the event and step index respectively of the primary proton track simulated, L_{sn} the mean energy loss per unit path length in the material, ε_{sn} the energy deposited by the primary proton along the step and ω_n the statistical weight of the primary proton. In this calculation, L_{sn} was obtained with the Geant4 method *ComputeElectronicDEDX()* of the *G4EmCalculator* class, which computes the LET from electronic stopping power tables, provided the particle type, kinetic energy and material traversed; while ε_{sn} was obtained by summing up the continuous part of the energy deposition due to the passage of the primary proton and the kinetic energy of the δ-rays released in the medium by the incident proton in the step considered.

In the present work, Equation (3.12) was used to calculate macroscopically the dose-averaged LET in the simulations, to be compared with the results of the microdosimetric calculations.

3.3 Materials and Methods

In this section, the main features of the Monte Carlo application developed for the computation of the microdosimetric quantities in Equation (3.9) are presented.

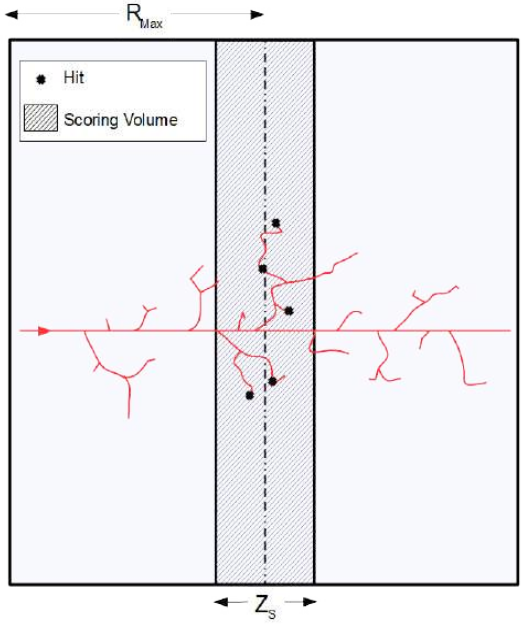

Figure 3.3: Scheme of the geometry used for microdosimetry simulations (2D projection). The primary proton (red track) is generated at the surface of a cubic water volume (world volume) and travels along the Z axis. The energy transfer points (hits) are then scored in the middle of the volume (shaded area), in a slab whose thickness (Z_S) varies depending on the dimension of the site. The spherical sites are not physically simulated, as they are virtually selected in the scoring volume with an algorithm that depends on the type of randomness considered. Finally, the half-dimension of the world volume (R_{max}) varies according to the maximum energy of the incident protons, and is slightly greater than the maximum range of the δ-rays emitted.

All the simulations were carried out with the Geant4 toolkit, by using our computing cluster hosted at Centro Informático Científico de Andalucía (CICA, Seville, Spain), consisting of 24 computational nodes, each with 2 × 12C AMD Abu Dhabi 6344 (2.6 GHz/6 MB) L3. The Geant4-DNA package, available within Geant4, was used to this purpose, as it makes possible to carry track structure simulations and tracking of electrons down to ≈ 10 eV.

3.3.1 Geometry

The geometry of the microdosimetry application is really simple, as shown in Figure 3.3. The *world volume*, i.e., the volume that represents the experimental area and contains all the other components, consists of a water cubic box having half dimension R_{max} slightly greater than the maximum range of the δ-rays emitted by the incident protons $R_{\delta,max}$. This range is calculated with Equation (1.4), and the

condition $R_{\max} \geq R_{\delta,\max}$ is necessary to ensure intra-track electronic equilibrium.
The scoring volume, i.e., the volume in which the energy transfer points (*hits*) are detected and stored, is a water slab positioned in the centre of the world volume with same transversal dimensions and variable thickness Z_{S}, depending on the dimension of the site chosen. The beam (red track in Figure 3.3) originates at the surface of the cubic volume and travels along the z-axis. The physical quantities of interest are scored in randomly-placed spherical sites, with diameters ranging from 1 to 10 µm. These sites are not simulated as physical volumes, but are virtually identified as regions in the scoring volume thanks to specific algorithms for the selection of their centres. For the site positioning, two sampling methods have been implemented, uniform and weighted random sampling, whose detailed description is given in Section 3.3.2.

In order to study the performance of the code, simulations were initially carried out with mono-energetic proton beams with energies ranging from 10 to 90 MeV, for spherical sites with diameters of 1 and 10 µm. The upper energy limit was imposed by the physics list employed for the simulations, as Geant4-DNA only allows calculations for proton energies lower than 100 MeV. On the other side, the lower energy limit was chosen to ensure that the short track segment condition was valid for all the energies and site dimensions considered.
Furthermore, to understand the dependence of the simulation results on the longitudinal dimensions of the scoring slab, a preliminary study was performed by varying the size of the scoring volume for the two extreme energies and site diameters. As a general rule, to allow for the correct functioning of the scoring algorithms (see Section 3.3.2) the relation $Z_{\mathrm{S}} > 2d$ must hold, where d is the site diameter. Therefore the formula $Z_{\mathrm{S}} = 2d + \eta$ was used, choosing for η the values $0.1d$, d, $2d$ and $10d$ (the latest only for the 1 µm diameter site). Since for the lowest energy and biggest site dimensions the maximum δ-ray range is smaller than half of the scoring volume thickness, $R_{\delta,\max} < Z_{\mathrm{S}}/2$, and in order to have the same proton kinetic energy distribution at the centre of the world volume for both site diameters, the decision to set $R_{\max} = R_{\delta,\max} + (Z_{\mathrm{S,max}}/2)$ for all the simulations was taken, with $Z_{\mathrm{S,max}} = 40\,\mu\mathrm{m}$.

3.3.2 Scoring algorithms

The most intuitive way of scoring energy deposition events in micrometric sites along a proton track would be to randomly select a point $\overrightarrow{P}_{\mathrm{C}}$ in the region of interest with a uniform probability and consider all the energy transfer points (hits) $\overrightarrow{P}_{\mathrm{h}_i}$ within a distance $|\overrightarrow{P}_{\mathrm{h}_i} - \overrightarrow{P}_{\mathrm{C}}| \leq d/2$ from it. This sampling method, known as μ-randomness, is very robust and is not subject to any bias. However, this technique

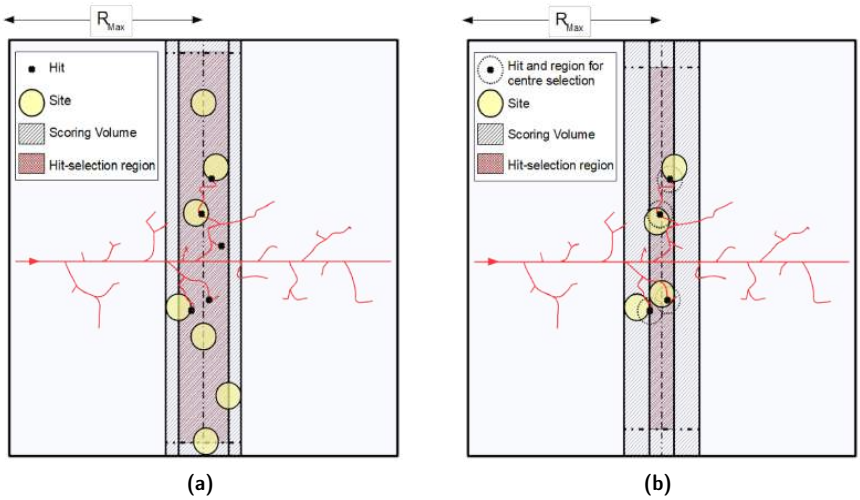

Figure 3.4: Graphical representation of the working principle of the two sampling algorithms: **(a)** uniform sampling (μ-randomness) and **(b)** weighted sampling (ν-randomness). In both cases, a hit selection region (maroon shaded area) is identified, where the centres of the sites (yellow circles) are sorted. The dimensions of this region depend on the sampling algorithm used and on the diameter of the site, as lateral margins must be left to ensure that the site is always fully included in the scoring volume. For uniform sampling this margin must be set equal to the site radius, while for weighted sampling the margin is equal to the site diameter.

is likely to be highly inefficient, as the probability of selecting volumes with no hits is really high and increases for the smaller sites and higher energies.

To increase the sampling efficiency, ν-randomness can be used instead. In this case, an energy transfer point $\overrightarrow{P}_{\mathrm{H}}$ is randomly chosen with uniform probability among the hits of the simulated track. Then, the centre of the site $\overrightarrow{P}_{\mathrm{C}}$ is sampled with uniform probability in a sphere of radius $d/2$ around $\overrightarrow{P}_{\mathrm{H}}$, i.e at a distance $|\overrightarrow{P}_{\mathrm{C}} - \overrightarrow{P}_{\mathrm{H}}| \leq d/2$. Finally, all the energy transfer points $\overrightarrow{P}_{\mathrm{h}_i}$ within a distance $|\overrightarrow{P}_{\mathrm{h}_i} - \overrightarrow{P}_{\mathrm{C}}| \leq d/2$ are considered for the computation of microdosimetric quantities in the site. In this way, the presence of a at least one energy transfer point $\overrightarrow{P}_{\mathrm{H}}$ in the site is always ensured, and a 100% sampling efficiency can be achieved. As a drawback, however, this method is spatially biased towards regions of high density of hits, and a compensation factor must be introduced to account for it. As suggested in other works [118, 119], this factor should be equal to the ratio of the number of hits that can be selected to the number of hits located in the randomly placed site.

Both methods were implemented in our Monte Carlo code developed for the computation of microdosimetric quantities, and their working principle is graphically represented in Figure 3.4. In order to increase the sampling efficiency of the uniform random method, a *while loop* controlled by a *flag* to a maximum of 1000 loops was

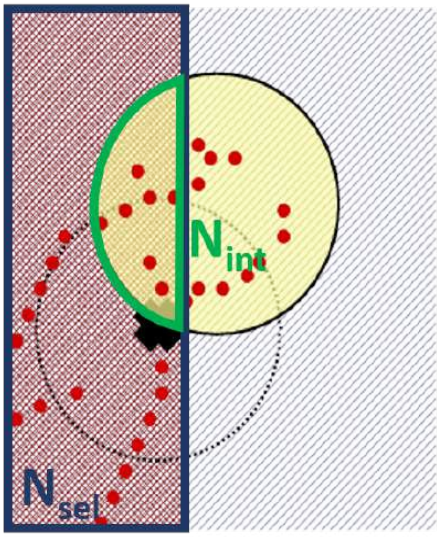

Figure 3.5: Detail of the working principle of the weighted sampling method in Figure 3.4b. The compensation factor is computed as the ratio between the number of selectable hits (with deposited energy different from zero) in the hit selection region (N_{sel}) and the number of hits in the intersection volume of the site with the hit selection region (N_{int}).

introduced to repeat the sorting procedure on the same track until one good event was found to the expenses of computational time. In both cases a hit selection region (maroon shaded area in Figure 3.4) must be identified, in which $\overrightarrow{P}_{\mathrm{C}}$ and $\overrightarrow{P}_{\mathrm{H}}$ are sorted. The dimensions of this region depend on the sampling algorithm used and on the diameter of the site. The general rule is that a margin must be left, both in the longitudinal and transverse dimensions, in order to ensure that all the randomly selected sites are always fully included in the scoring volume. For the uniform random sampling, this margin must be set equal to the site radius, while for weighted sampling it is equal to the site diameter.

Following the previous considerations, in the case of weighted sampling, the compensation factor must be set equal to $N_{\mathrm{sel}}/N_{\mathrm{int}}$, as shown in Figure 3.5, where N_{sel} is the number of hits (with energy deposited different from zero) in the hit selection region that can be randomly selected, and N_{int} is the number of hits in the intersection volume of the site and the hit selection region.

After sorting the position of the site, three main quantities are computed: the total energy deposited in the site per event (ϵ), the total energy deposited for a single proton collision (ε_{c}) and the chord length (l) of the proton traversing the site. While the computation of ϵ is straightforward, i.e., the sum of the energies deposited by each hit happening within the site, the computation of ε_{c} and l cannot be done directly and will be discussed in the following paragraphs.

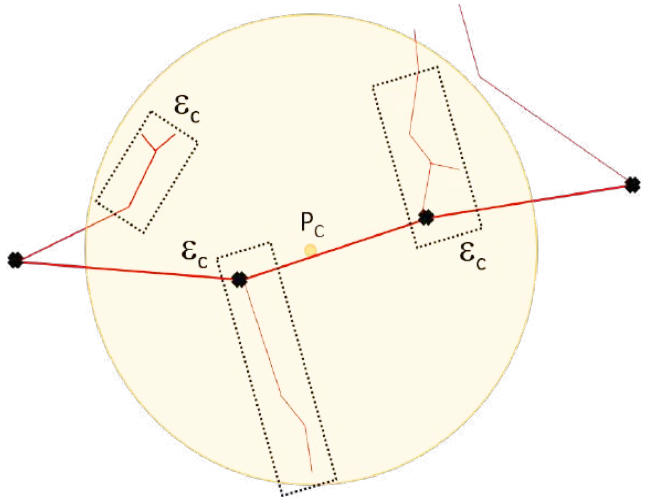

Figure 3.6: Schematic representation of the scoring method for the evaluation of the energy deposited per single proton collision in the site, ε_c. The primary δ-ray generated by the proton collision is identified and assigned one distinctive tag, that is then inherited by all the secondary electrons in the shower. Only the energy deposition events happening within the site are accounted for in the calculation of ε_c, including δ-ray influx from outside the site.

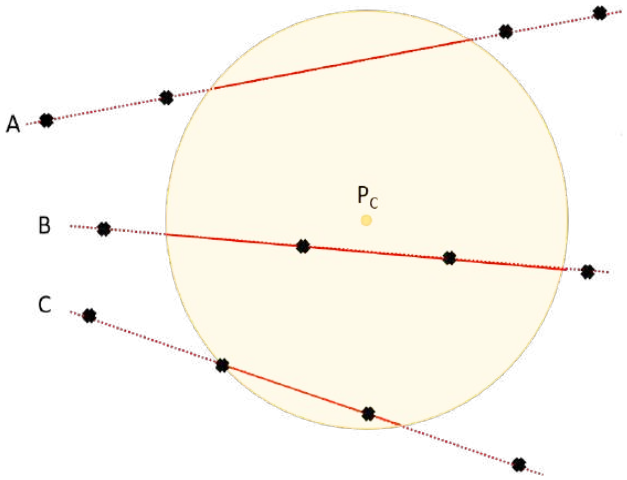

Figure 3.7: Graphical representation of the possible configurations in which proton tracks (red lines) can cross a site. The black points identify the position of the proton hits, for which the spatial coordinates are known and stored. The track segment between two hits identifies a step. The solid red lines are the proton track segments to be considered for the computation of the chord length distribution. Depending on the position of the site with respect to the proton track, a step can start and end outside the site (A), have one or both ends included in the site (B), or originate (or end) at the surface of the site (C).

Computation of energy deposited per individual proton collision In order to compute the energy imparted to the sensitive volume per each individual proton collision, the electronic showers generated by each collision must be uniquely identified. This was done by means of a *Sensitive Detector* class coded for this purpose, by identifying the primary electrons set in motion by a proton collision and assigning them a distinctive tag equal to their track identification number during the Geant4 simulation. By doing so, and thanks to the structure of the tracking algorithm of Geant4, all the subsequent secondary electrons created by further collisions of the electron originating the shower can be assigned the same tag. In this way, the energy deposited in the site by each δ-ray shower originating in the site or entering the site can be scored independently, as graphically represented in Figure 3.6.

Computation of chord length For the computation of the chord length distribution, the length of the segments of the primary proton trajectories intercepting the site must be evaluated. If the sites were built as physical volumes in the Geant4 application, this procedure would be straightforward, as track steps are always forced to end at the interface between two volumes. This, however, does not apply in the case under consideration, as the randomly placed sites do not have a physical interface and track steps can cross the volume surface. Therefore, proton chord lengths had to be computed manually from geometric considerations, taking into account all the possible configurations in Figure 3.7.

3.3.3 Output

Once the site is positioned, the different microdosimetric quantities can be computed and stored. The Monte Carlo code developed provides two ways of storing and saving the results, both in ROOT format: histograms containing the distributions of the physical quantities of interest and *trees* containing detailed information of each track. The ROOT tree format offers the advantage of being more flexible, as it allows to analyse the proton tracks on an event by event base after having run the simulation. To do so, a ROOT macro was developed implementing the same site positioning algorithms just described. However, the size of the outputs produced in this way might be of several GB and they are not always easy to handle. ROOT histograms, on the other side, provide a compact and more manageable output, at the expense of the information about the single events.

When considering the histogram output format, the best way of representing microdosimetric distributions is to use the semi-logarithmic scale, since the energy deposited in each event has a variability of different orders of magnitude. By definition, the probability densities of the single event distributions are normalised to one.

This normalisation must remain unchanged when $f(\epsilon)$ is plotted on a logarithmic scale of ϵ, therefore a proper normalisation factor must be applied.
Let the logarithmic scale of ϵ be subdivided in B increments per decade, such that the i-th value of ϵ is:

$$\epsilon = \epsilon_0 \cdot 10^{\frac{i}{B}}, \tag{3.13}$$

where ϵ_0 is the lowest value of ϵ to be considered in the histogram. In this case, the logarithmic increment of ϵ is $\mathrm{d}\log\epsilon \sim 1/B$. Therefore, the content of the i-th bin of the histogram distribution becomes:

$$n\left(\epsilon_{i+\frac{1}{2}}\right) = \int_{\epsilon_i}^{\epsilon_{i+\frac{1}{2}}} f(\epsilon)\,\mathrm{d}\epsilon = \ln 10 \int_{\epsilon_i}^{\epsilon_{i+\frac{1}{2}}} \epsilon f(\epsilon)\,\mathrm{d}\log\epsilon \sim \frac{\ln 10}{B}\epsilon_{i+\frac{1}{2}} f\left(\epsilon_{i+\frac{1}{2}}\right), \tag{3.14}$$

where $\epsilon_{i+1/2} = \sqrt{\epsilon_{i+1}\cdot\epsilon_i}$ is the central value of the i-th bin.
Finally, for the computation of the uncertainties associated to the averaged values extracted from the Monte Carlo simulation, an event by event approach can be used [120]:

$$\sigma_{\overline{X}} = \sqrt{\frac{1}{N-1}\left[\frac{\sum_{i=1}^{N} X_i^2}{N} - \left(\frac{\sum_{i=1}^{N} X_i}{N}\right)^2\right]}, \tag{3.15}$$

where N is the number of independent events and X is the quantity under study.

3.3.4 Simulation of mono-energetic proton beams

Our Monte Carlo code developed accepts as input proton beams with any energy distribution, thanks to a *PrimaryGeneratorAction* class able to import spectral fluence distributions in ROOT format and to use them as a beam generator. For the sake of testing the code performances, however, simulations were performed with mono-energetic proton beams having energies of 10, 20, 40, 70 and 90 MeV, for site sizes of 1 and 10 µm diameter.
For all the cases considered, simulations were run both with uniform and with weighted random sampling, the first serving as reference. A number of 250 000 proton tracks was simulated for every case, divided in 250 parallel jobs, and the efficiency of each sampling method was evaluated and compared, measuring also the time required by an individual job to complete the simulation.
Finally, $\overline{L}_{\mathrm{D}}$ values were computed with Equation (3.9) from the microdosimetric quantities, and compared to the macroscopic $\overline{L}_{\mathrm{D}}$ computed with Equation (3.12). Furthermore, since in the case of mono-energetic proton beams the LET distribution

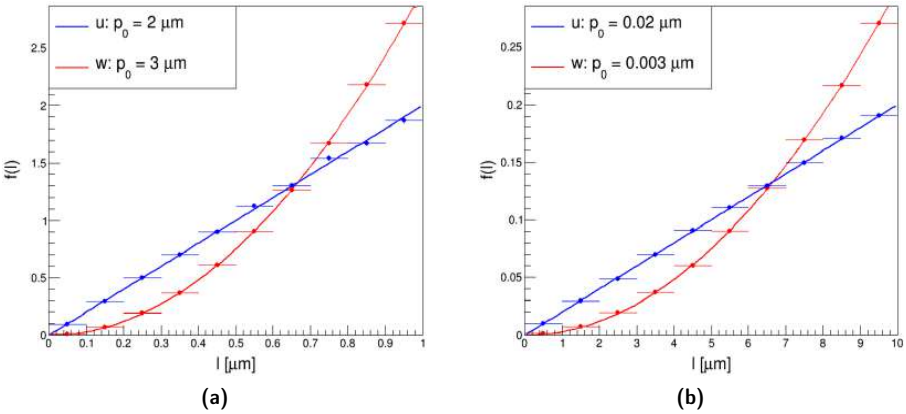

Figure 3.8: Chord length distributions obtained for 10 MeV protons impinging on sites of 1 **(a)** and 10 µm **(b)** diameter. The distributions obtained with uniform (blue, u) and weighted random sampling (red, w) have been fitted with functions of the form $f_{\mathrm{u}}(l) = p_0 l$ and $f_{\mathrm{w}}(l) = p_0 l^2$ according to Table 3.1. The values obtained for the fit parameters (see Table 3.2) are in perfect agreement with the theoretical ones.

can be considered as a delta function, centred at the LET of the particle for the specific energy considered, the relation $\overline{L}_{\mathrm{D}} = \overline{L}_{\mathrm{F}} = \overline{y}_{\mathrm{F}}$ should hold and was used for an extra validation.

3.4 Results

The easiest way to check for the correct functioning of the sampling methods implemented in the code is to analyse the chord length distributions obtained, and compare their mean values with the theoretical ones listed in Table 3.1. An example of this comparison is shown in Figure 3.8 for sites of 1 and 10 µm diameter.
The chord length distributions computed with the simulations were then fitted with the corresponding functions for uniform (μ-randomness) and weighted (ν-randomness) random sampling, and the obtained parameters compared with the theoretical values.

Table 3.2: Fit functions and resulting parameters (p_0) obtained from the fit of the chord length distributions in Figure 3.8, compared with the expected parameter for the type of randomness considered.

d[µm]	fit function	p_0	expected p_0
1	$f_{\mathrm{u}}(l) = p_0 l$	$2.00(1)\,\mu\mathrm{m}^{-2}$	$2/d^2 = 2\,\mu\mathrm{m}^{-2}$
	$f_{\mathrm{w}}(l) = p_0 l^2$	$3.006(6)\,\mu\mathrm{m}^{-3}$	$3/d^3 = 3\,\mu\mathrm{m}^{-3}$
10	$f_{\mathrm{u}}(l) = p_0 l$	$2.000(4) \times 10^{-2}\,\mu\mathrm{m}^{-2}$	$2/d^2 = 0.02\,\mu\mathrm{m}^{-2}$
	$f_{\mathrm{w}}(l) = p_0 l^2$	$3.006(6) \times 10^{-3}\,\mu\mathrm{m}^{-3}$	$3/d^3 = 0.003\,\mu\mathrm{m}^{-3}$

Table 3.3: Values of the longitudinal dimensions assigned to the world volume and the scoring volume to study the dependence of the simulation results on the geometrical parameters. The longitudinal half dimension of the world volume $R_{\max}$ is equal to $R_{\delta,\max} + Z_{S,\max}/2$, where $R_{\delta,\max}$ is the maximum range of the δ-rays emitted by the incident protons and $Z_{S,\max}$ is the maximum thickness of the scoring volume among the ones considered. Indeed, the thickness Z_S of the scoring volume is variable and must be chosen according to the size of the site and the energy of the incident particle, in such a way that the short track segment condition is always preserved; however, the condition $Z_S > 2d$ must hold. In this study Z_S was set equal to $2d + \eta$, assigning to η the values $0.1d$, d, $2d$ and $10d$.

Energy	d	$R_{\delta,\max}$	$R_{\max}$	$Z_{S,\max}$	Z_S	η
10 MeV	1 µm	8.3 µm	28.3 µm	40 µm	2.1 µm	$0.1d$
					3 µm	d
					4 µm	$2d$
					12 µm	$10d$
10 MeV	10 µm	8.3 µm	28.3 µm	40 µm	21 µm	$0.1d$
					30 µm	d
					40 µm	$2d$
90 MeV	1 µm	410 µm	430 µm	40 µm	2.1 µm	$0.1d$
					3 µm	d
					4 µm	$2d$
					12 µm	$10d$
90 MeV	10 µm	410 µm	430 µm	40 µm	21 µm	$0.1d$
					30 µm	d
					40 µm	$2d$

A perfect agreement emerged, as reported in Table 3.2.

As described in Section 3.3.1, a preliminary study was performed to assess the influence of the longitudinal dimension of the scoring volume (Z_S) on the simulation output. To do so, simulations were carried out with mono-energetic proton beams of 10 and 90 MeV on spherical sites of 1 and 10 µm diameter, assigning to Z_S the values listed in Table 3.3, both with uniform and weighted random sampling.

For the uniform random sampling method no differences were observed in the resulting distributions of energy imparted $f(\epsilon)$ and energy imparted per collision $f(\varepsilon_c)$; on the contrary, the weighted sampling method showed a clear dependence of the results on the Z_S selected, as emerges from Figure 3.9. In this figure, the normalised distributions of $\epsilon f(\epsilon)$, represented in the semi-logarithmic scale, obtained for the different Z_S with weighted sampling (w), are plotted together and compared with the distribution obtained with uniform random sampling (u).

While distributions obtained by uniform sampling are not affected by Z_S, they are strongly affected by statistics, as the efficiency of the method drastically decreases for higher energies and smaller site sizes, as can be seen in Figure 3.9c. On the other

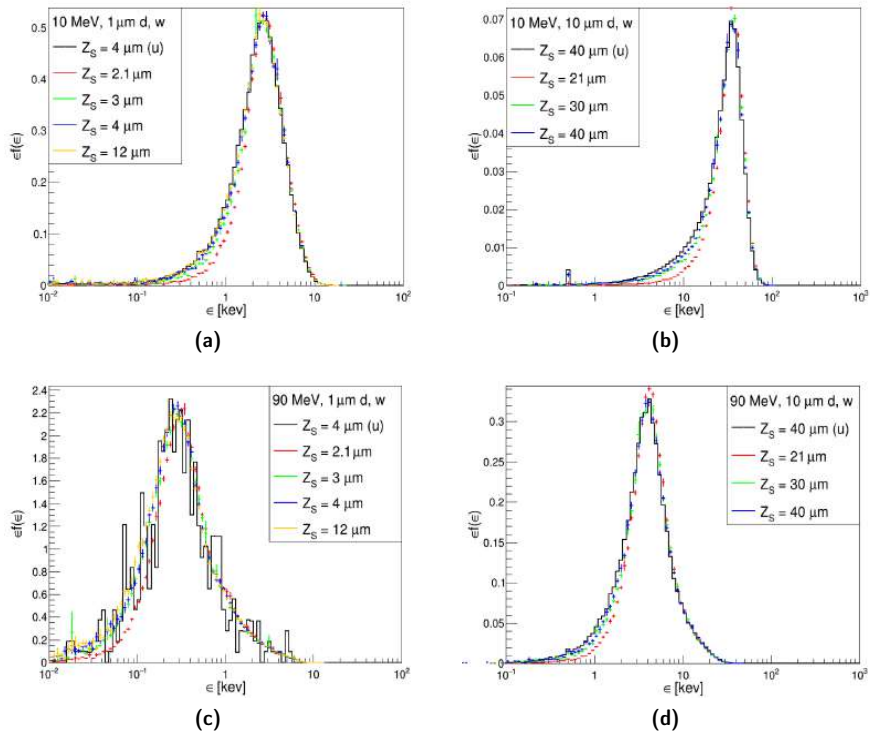

Figure 3.9: Variation of the distribution of energy imparted $\epsilon f(\epsilon)$ with the thickness of the scoring volume Z_S. Simulations were done with 10 MeV protons on sites of 1 **(a)** and 10 µm diameter **(b)**, and with 90 MeV protons on sites of 1 **(c)** and 10 µm diameter **(d)**. The distributions of energy imparted obtained with the uniform random sampling method (u) are not affected by Z_S, and are represented here as a reference (black solid lines).

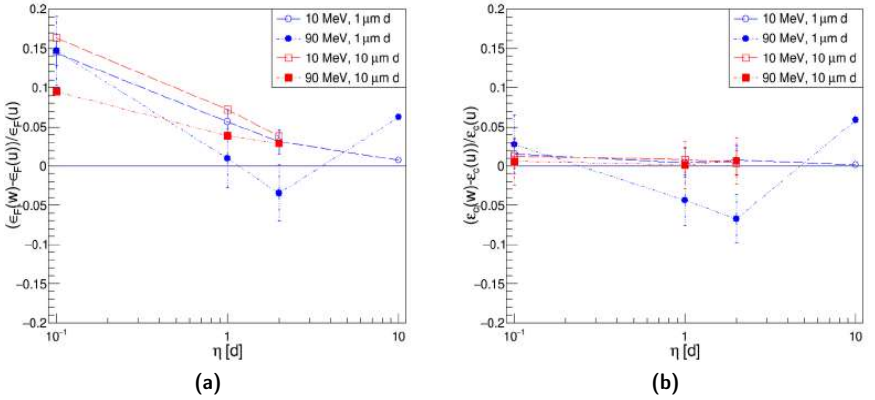

Figure 3.10: Relative difference of the average values of the distributions of energy imparted **(a)**, and energy imparted per collision **(b)** obtained with the weighted and uniform random sampling methods, as a function of η.

hand, the distributions obtained with weighted random sampling (w) vary strongly with the thickness of the scoring volume, resulting in a general underestimation of the low energy tail of the distributions. The difference between the shape of uniform and weighted distributions decreases as Z_S increases, and tends to disappear for $\eta >> 2d$.

This is shown more clearly in Figure 3.10a, where the relative difference between the mean values of $\epsilon f(\epsilon)$, or $\bar{\epsilon}_F$, for weighted and uniform sampling is plotted as a function of η. The absolute values of $\bar{\epsilon}_F$ for the different cases are listed in Table 3.4. Maximum deviations from the mean value of the uniform distributions of about 15% were observed in the worse cases; but this percentage decreased below 5% for $\eta \geq 2d$. The exception in the behaviour shown by the 90 MeV case for the site of 1 µm is related to the low statistics achieved with uniform random sampling. At this energy, indeed, the density of hits in the scoring volume decreases drastically and so does the efficiency of the uniform random sampling method.

Figure 3.10b, on the other hand, shows the relative difference between the mean values of the $\varepsilon_c f(\varepsilon_c)$ distributions, $\bar{\varepsilon}_c$, obtained with weighted and uniform random sampling, which are listed in Table 3.5. In this case, no evident dependence on η emerges, and the difference between the two sampling methods is almost constant and lower than 2% for most cases. In view of the outcomes of this preliminary analysis, the decision of setting $Z_S = 4d$ (corresponding to $\eta = 2d$) for all the subsequent simulations was taken, and results obtained with weighted random sampling were treated equivalently to uniform ones, applying Equation (3.10) for both methods.

Following the identification of the best Z_S, various simulations were carried out with beams of 10, 20, 40, 70 and 90 MeV on sites of 1 and 10 µm diameter to derive the values of $\overline{L}_D$ from Equation (3.10) and compare them with the macroscopic $\overline{L}_D$ obtained from the Monte Carlo with Equation (3.12). Figure 3.11 shows the dependence on the impinging proton energy of the frequency-averaged energy imparted per event ($\bar{\epsilon}_F$). Here, the results obtained with weighted and uniform random sampling are plotted together and compared: relative deviations lower than 5%, between the values obtained with weighted and uniform random sampling, emerged for all the energies considered.

As briefly stated in Section 3.2.2, the energy deposited per single proton collision, that reflects the effects of energy straggling and δ-ray influx and escape, is an independent random factor from LET and chord length, and its distribution should not be affected by them. Therefore, when calculating L_D with Equation (3.10), the variance of LET and the variability of the chord length should not be included in the computation of the second moment of the distribution of energy imparted per single proton collision, δ_2. In other words, only the distribution of energy imparted per single proton collision

Table 3.4: Values of the frequency-averaged energy imparted per event as a function of η for the different sampling methods and energies considered.

	$\overline{\epsilon}_{\mathrm{F}}$ [keV]			
	$d = 1\,\mu\mathrm{m}$			
η	10 MeV		90 MeV	
	u	w	u	w
$0.1d$	2.62(1)	2.995(3)	0.46(2)	0.522(2)
$1d$	2.62(1)	2.770(3)	0.47(2)	0.474(1)
$2d$	2.63(1)	2.707(3)	0.48(2)	0.464(1)
$10d$	2.62(1)	2.640(3)	0.43(2)	0.452(1)
	$d = 10\,\mu\mathrm{m}$			
η	10 MeV		90 MeV	
	u	w	u	w
$0.1d$	28.86(3)	33.55(2)	4.53(2)	4.95(1)
$1d$	28.85(3)	30.92(3)	4.55(2)	4.73(1)
$2d$	28.99(3)	30.09(3)	4.54(2)	4.67(1)

Table 3.5: Values of the first moment of the energy deposited per collision as a function of η for the different sampling methods and energies considered.

	$\overline{\varepsilon}_{\mathrm{c}}$ [keV]			
	$d = 1\,\mu\mathrm{m}$			
η	10 MeV		90 MeV	
	u	w	u	w
$0.1d$	0.0491(6)	0.0499(4)	0.044(5)	0.0454(4)
$1d$	0.0491(6)	0.0493(4)	0.048(7)	0.0455(3)
$2d$	0.0491(6)	0.0494(3)	0.048(6)	0.0447(3)
$10d$	0.0492(6)	0.0493(3)	0.042(4)	0.0445(3)
	$d = 10\,\mu\mathrm{m}$			
η	10 MeV		90 MeV	
	u	w	u	w
$0.1d$	0.0578(6)	0.0585(7)	0.053(1)	0.0532(6)
$1d$	0.0579(6)	0.0583(6)	0.053(1)	0.0528(6)
$2d$	0.0580(6)	0.0582(6)	0.052(1)	0.0528(6)

corresponding exactly to a frequency-averaged energy imparted per event $\bar{\epsilon}_F$ and a chord length $\bar{l}_F$ should be considered to calculate δ_2. This was firstly done by a dedicated simulation, positioning the site in such a way that the particle traversed it with a path length equal to $\bar{l}_F$ [115]. Later on, a new approach was introduced in our Monte Carlo code, to extract the value of δ_2 directly from the main simulation results, consisting of a two dimensional plot of the distribution $\varepsilon_c^2 f(\varepsilon_c)$ as a function of the primary proton trajectory length l. From this plot, projections were taken for intervals of l with size $0.1d$, and a graph of δ_2 values as a function of l was extracted, as shown in Figure 3.12.

For values of $l < d/2$, the main contribution to δ_2 is given by the δ-ray influx, whose influence decreases quickly as l increases up to a point in which, for $l > d/2$, the value of δ_2 can be considered as constant. Since $\bar{l}_F > d/2$, the final values of δ_2 were extracted from the average of the points in the range $l > d/2$ weighted by their uncertainty, as depicted in Figure 3.12.

Finally, in Figure 3.13 results of δ_2 obtained with weighted and uniform random sampling are plotted together as a function of the energy, being the relative difference of the first from the second always lower than 6%, as expected. From this figure

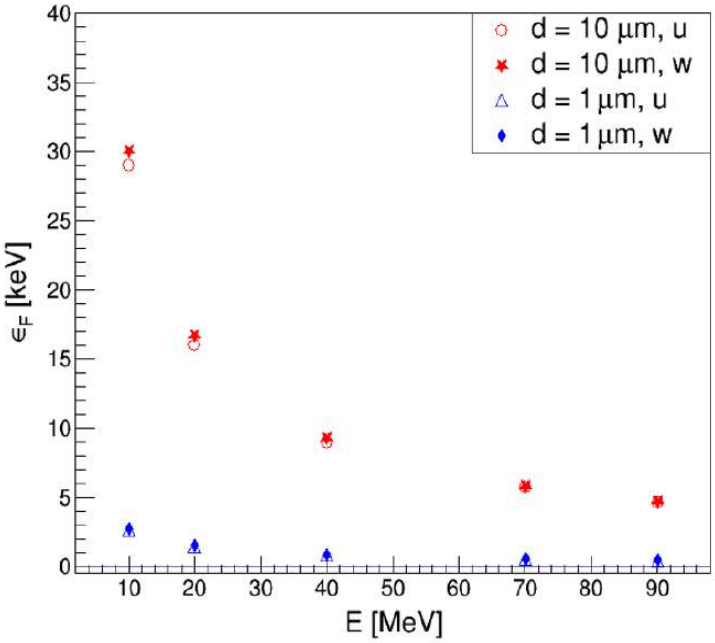

Figure 3.11: frequency-averaged energy imparted per collision $\bar{\epsilon}_F$ as a function of the proton energy. Uniform (open markers) and weighted (full markers) random sampling results are plot together and compared for sites of 1 (blue triangles and diamonds) and 10 µm (red circles and stars).

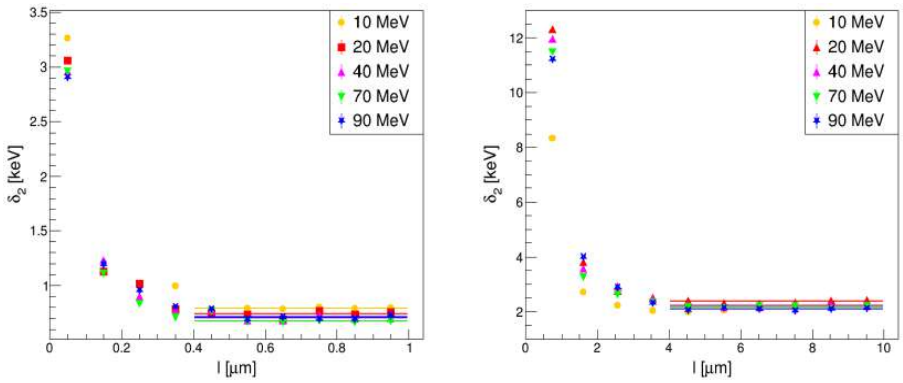

Figure 3.12: Variation of δ_2 as a function of the proton trajectory length l for the different energies and sites of **(a)** 1 µm and **(b)** 10 µm diameter obtained with weighted random sampling. For the lower l values, the main contribution to δ_2 is given by the δ-ray influx, whose influence decreases quickly as l increases. For $l > d/2$, the value of δ_2 can be considered as constant. Since $\bar{l}_F > d/2$, the final values of δ_2 were extracted by averaging the points (weighted by their uncertainties) in the range $l > d/2$ (solid lines).

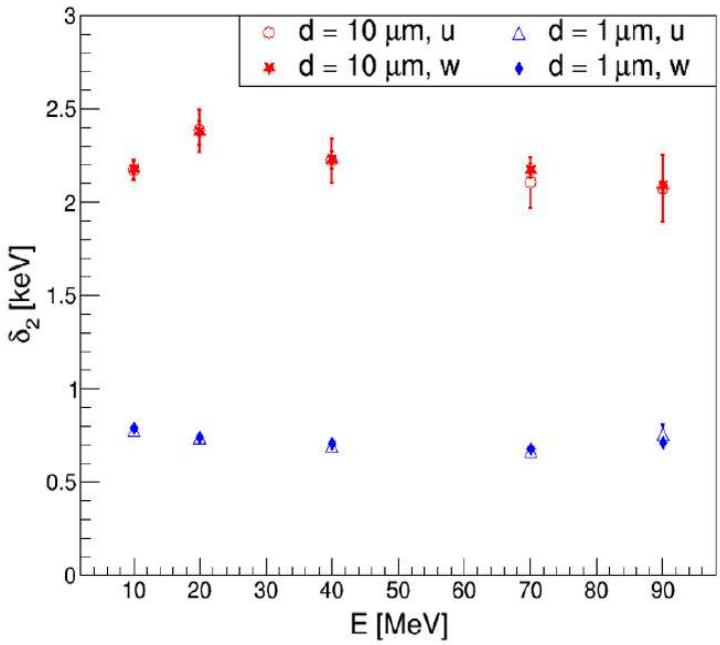

Figure 3.13: Second moment of the energy imparted per individual proton collision δ_2 as a function of the proton kinetic energy. Uniform (open markers) and weighted (full markers) random sampling results are plotted together and compared for sites of 1 (blue triangles and diamonds) and 10 µm (red circles and stars).

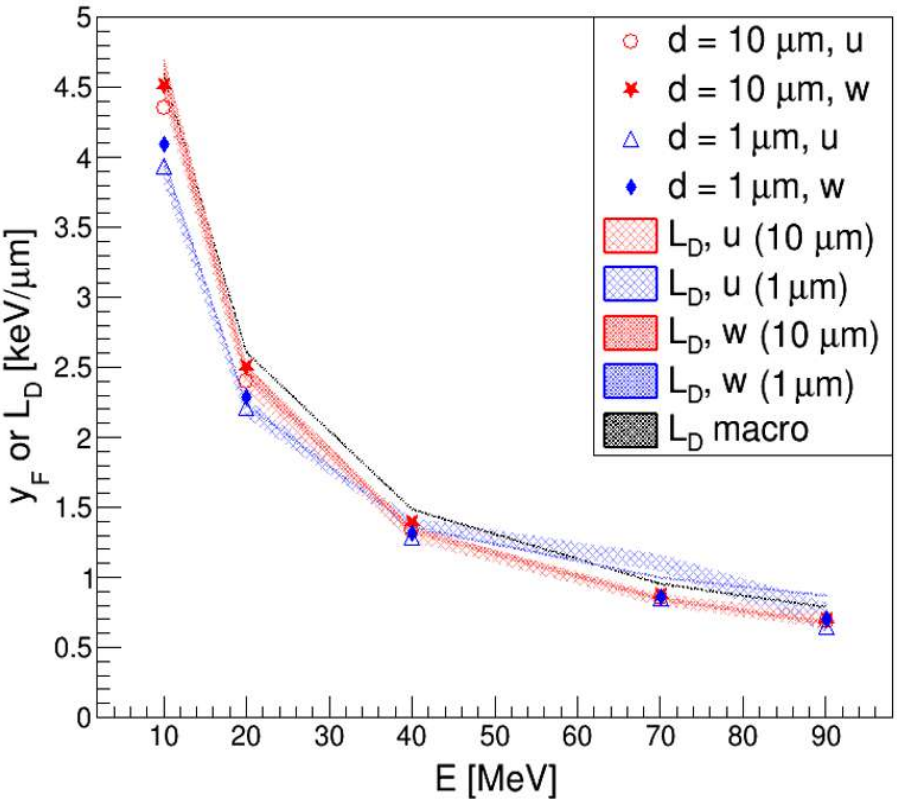

Figure 3.14: Frequency-averaged lineal energy $\overline{y}_{\mathrm{F}}$ as a function of the incident proton kinetic energy. Values obtained for uniform (open markers) and weighted (full markers) random sampling methods are plotted together for sites of 1 (blue triangles and diamonds) and 10 µm (red circles and stars) diameter. For mono-energetic proton beams the relation $\overline{L}_{\mathrm{D}} = \overline{y}_{\mathrm{F}}$ should hold (see Section 3.3.4), therefore $\overline{y}_{\mathrm{F}}$ values are reported superimposed to the respective L_{D} values derived from Equation (3.10), represented as shaded areas whose thickness is given by the error associated to $\overline{L}_{\mathrm{D}}$ for each diameter site. The macroscopic $\overline{L}_{\mathrm{D}}$ computed with Equation (3.12) (black shaded area) is also reported as a reference.

emerges slightly the relative impact of the straggling distribution on the value of $\overline{L}_{\mathrm{D}}$, graphically justified in Figure 3.1, as a function of the energy: for sites of 1 µm diameter, the effect of straggling is mostly relevant in the range of proton energies $4-12$ MeV, while for higher energies δ-ray influx and escape become predominant; for sites of 10 µm diameter, on the other hand, the effect of straggling becomes relevant from 14 MeV up to ~ 70 MeV. This is the reason why the value of δ_2 decreases for the 10 µm site at proton energies lower than 20 MeV.

The results obtained for the frequency-averaged lineal energy $\overline{y}_{\mathrm{F}}$ with both sampling methods are presented in Figure 3.14. In this figure, $\overline{y}_{\mathrm{F}}$ values are reported as a function of the incident proton energy, and superimposed to the $\overline{L}_{\mathrm{D}}$ values derived

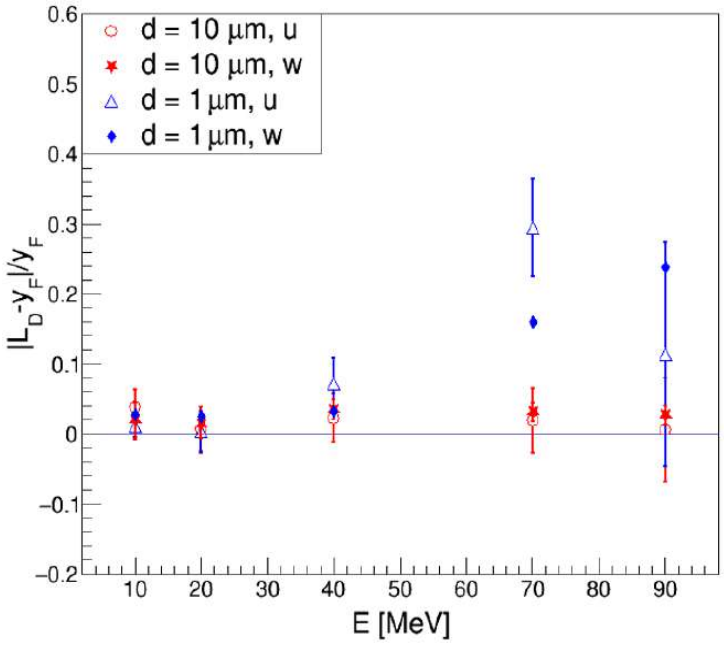

Figure 3.15: Relative difference of $\overline{L}_{\mathrm{D}}$ from $\overline{y}_{\mathrm{F}}$ for the different site diameters (blue markers for 1 µm and red markers for 10 µm) and sampling methods considered (open markers for uniform sampling and full markers for weighted sampling).

from Equation 3.10. As stated in Section 3.3.4, for mono-energetic proton beams the relation $\overline{y}_{\mathrm{F}} = \overline{L}_{\mathrm{D}}$ should hold. In this context, this relation is used as a further test of the code performances, and $\overline{L}_{\mathrm{D}}$ values are represented in Figure 3.14 as shaded areas whose width is given by the uncertainty associated to them.

Figure 3.15 represents the relative difference of $\overline{L}_{\mathrm{D}}$ from $\overline{y}_{\mathrm{F}}$ for the different site diameters and sampling methods considered. While for the 10 µm diameter site these differences are always lower than 6%, for the 1 µm site the difference increases with energy, reaching values of 30%. This effect is especially evident looking at the weighted random sampling points, which are not affected by the lack of statistics that characterises the uniform sampling method at higher energies. Moreover, this increasing difference between $\overline{L}_{\mathrm{D}}$ and $\overline{y}_{\mathrm{F}}$ for the 1 µm site results in an anomalous behaviour of $\overline{L}_{\mathrm{D}}$ if compared to the macroscopic dose-averaged LET obtained from Equation (3.12), represented as a black shaded area in Figure 3.14. Indeed, as stated in Section 3.2.1, the $\overline{L}_{\mathrm{D}}$ computed with Equation (3.10) is restricted, being this statement especially true for the 1 µm site, and should never be higher than the dose-averaged LET computed macroscopically, as it happens instead in Figure 3.14.

To solve this problem, the concepts of *effective mean chord length* $\overline{l}^{*}_{\mathrm{F}}$ and *effective frequency- and dose-averaged lineal energy* $\overline{y}^{*}_{\mathrm{F,D}}$ were introduced. As done for the

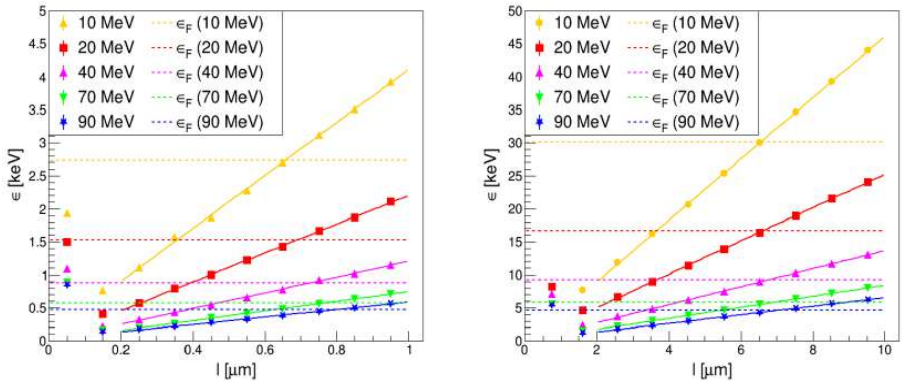

Figure 3.16: Variation of the mean energy imparted per event, ϵ, as a function of l for the different energies and sites of **(a)** 1 µm and **(b)** 10 µm diameter obtained with weighted random sampling. For $l \sim 0$, i.e proton tracks that don't cross the site or pass tangent to it, the only contribution to ϵ is given by the δ-ray influx. Then, for higher l, ϵ increases linearly with the chord length, as can be observed from the linear fit of the data (solid line). The overall frequency-averaged energies imparted per event, $\bar{\epsilon}_F$ obtained for each simulation considering the full data set, are reported as horizontal dashed lines, each colour corresponding to one proton energy. The intersection point of the linear fit of ϵ as a function of l and the value of $\bar{\epsilon}_F$ corresponds to the effective $\bar{l}^*_F$.

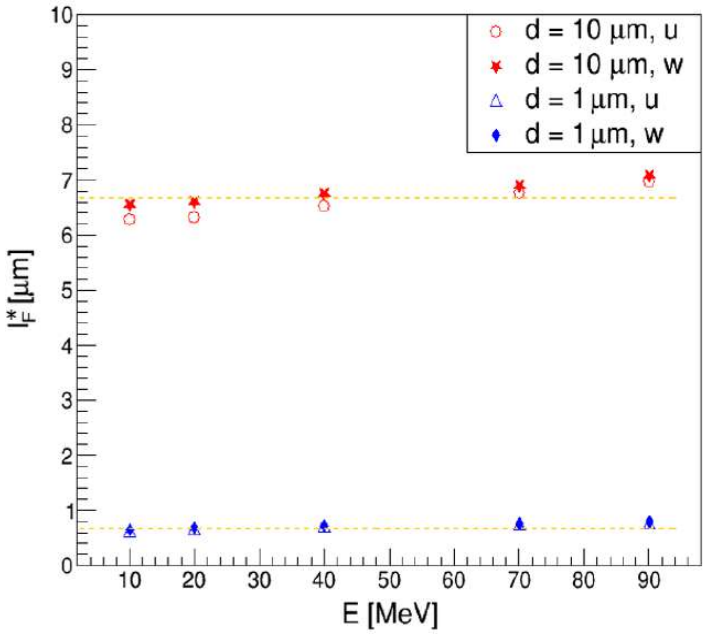

Figure 3.17: Effective mean chord length $\bar{l}^*_F$ as a function of the proton energy, obtained with uniform (open markers) and weighted (full markers) random sampling for sites of 1 µm (blue triangles and diamonds) and 10 µm (red circles and stars). The true mean chord length $\bar{l}_F = 2d/3$ is reported as a yellow horizontal dashed line for each site dimension.

energy imparted per single proton collision, a two dimensional plot of $\epsilon f(\epsilon)$ as a function of l was implemented in the simulation, and projections were extracted for intervals of l with width $0.1d$. In this way, plots of the mean energy imparted per event, ϵ as a function of the chord length could be built, as shown in Figure 3.16. For $l \sim 0$, i.e proton tracks that don't cross the site or pass tangent to it, the only contribution to ϵ is given by the δ-ray influx. Then, for higher l, ϵ increases linearly with the chord length. Comparing the overall frequency-averaged energies imparted per event, $\bar{\epsilon}_{\mathrm{F}}$ obtained for each simulation considering the full data set, and the linear fits of ϵ as a function of l, the values of l corresponding exactly to an energy imparted per event equal to $\bar{\epsilon}_{\mathrm{F}}$ could be obtained. This value, defined as effective mean chord length $\bar{l}^{*}_{\mathrm{F}}$ should in principle be equal to $\bar{l}_{\mathrm{F}}$. However, this is not the case as emerges from Figure 3.17, and $\bar{l}^{*}_{\mathrm{F}}$ differs from the true value of $\bar{l}_{\mathrm{F}} = 2d/3$ and varies with the proton energy.

Using the effective chord lengths corresponding to each energy, for the computation of frequency- and dose-averaged lineal energies, the results shown in Figure 3.18 could be obtained. In this figure, a general better agreement between uniform and weighted random sampling methods emerges, if compared to Figure 3.14. Furthermore, as shown in Figure 3.19 relative differences of $\overline{L}_{\mathrm{D}}$ from $\overline{y}_{\mathrm{F}}$ lower than 6% could be observed for both site dimensions and all energies, being the only exception the points obtained for the two highest energies and 1 µm diameter with uniform sampling, due to the lack of statistics. Finally, all the values of $\overline{L}_{\mathrm{D}}$ obtained with Equation (3.10) lay below the macroscopic unrestricted dose-averaged LET, as expected.

The lower efficiency of uniform random sampling has emerged numerous times along this section, being its effects especially evident for sites of 1 µm diameter and proton kinetic energies above 70 MeV. In order to quantify this effect, Table 3.6 collects the sampling efficiencies and computational times of the simulations performed with sites of 1 µm diameter with both sampling methods.

While the difference in computational time is not critical when comparing the time needed to generate 1000 events, the loss in statistics is dramatic and the efficiency drops to less than 40% for the best case. Considering that with the uniform random sampling algorithm each track is sampled to a maximum of 1000 times until one event is "detected", i.e., at least one energy deposition is found inside the site, the actual efficiency of the method is even lower. To give a clearer idea of the computational cost, the time needed to achieve the same statistics (i.e. 250 000 detected events) with uniform random sampling has been extrapolated in the last column t_{E} of Table 3.6. As emerges from these data, the time needed to achieve an equivalent statistical level with uniform random sampling grows exponentially with the energy of the incident proton energy, being more than 5 years for a beam of 90 MeV.

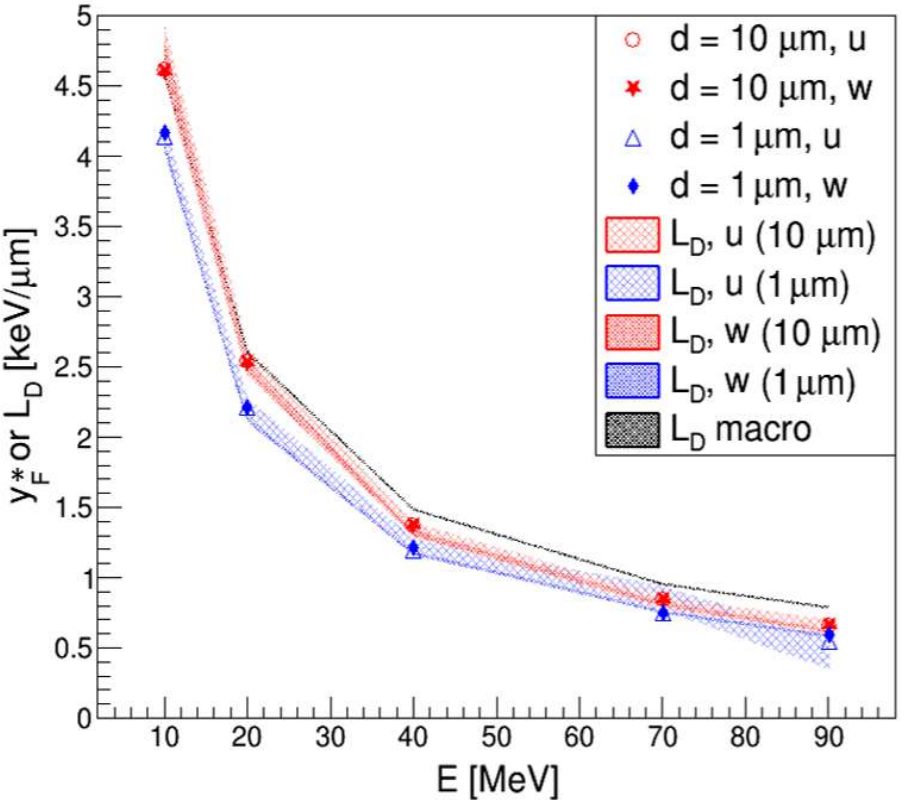

Figure 3.18: Effective frequency-averaged lineal energy $\overline{y}_{\mathrm{F}}^{*}$ as a function of the incident proton kinetic energy. Values obtained for uniform (open markers) and weighted (full markers) random sampling methods are plotted together for sites of 1 (blue triangles and diamonds) and 10 µm (red circles and stars) diameter. Values of $\overline{y}_{\mathrm{F}}^{*}$ are reported superimposed to the respective L_{D} values derived from Equation (3.10), represented as shaded areas whose thickness is given by the error associated to $\overline{L}_{\mathrm{D}}$ for each diameter site. The macroscopic $\overline{L}_{\mathrm{D}}$ computed with Equation (3.12) (black shaded area) is also reported as a reference.

3.5 Discussion

In this chapter, a novel Monte Carlo code for the computation of microdosimetric distributions generated by proton track segments in liquid water was presented. Two different algorithms were implemented for the scoring of the quantities of interest: uniform random sampling and weighted random sampling. While the first is ideally better as it is not subject to any bias, it is also very inefficient due to the high chances of selecting sites with no energy depositions within. On the contrary, weighted random sampling has a 100% efficiency, but might be subject to biases related to the choice of the size of the scoring volume and of the weighting factor.

One of the main elements of novelty of our code is the inclusion of an algorithm for the computation of the distribution of energy imparted per individual proton collision,

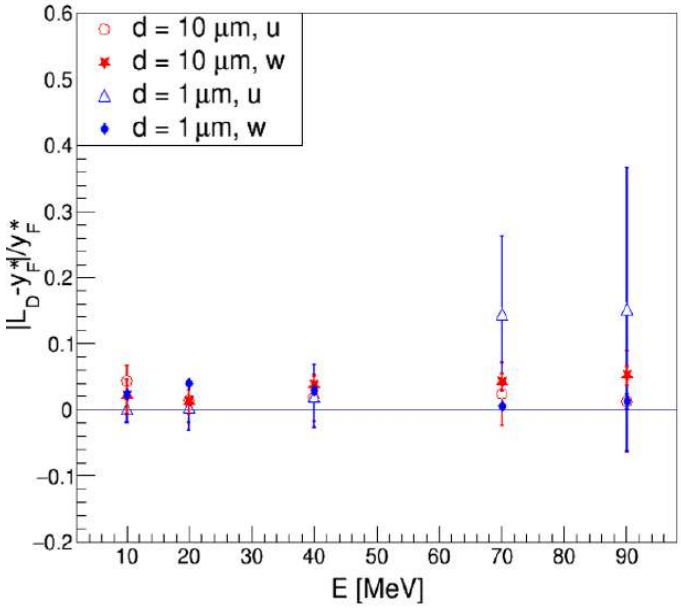

Figure 3.19: Relative difference of $\overline{L}_{\mathrm{D}}$ from $\overline{y}_{\mathrm{F}}^{*}$ for the different site diameters (blue markers for 1 µm and red markers for 10 µm) and sampling methods considered (open markers for uniform sampling and full markers for weighted sampling).

which has never been included in any of the Geant4-DNA examples of the official release of Geant4. This distribution, which is not easy to measure experimentally, reflects the action of energy straggling and δ-ray influx and escape on the energy deposited in the site, and it is fundamental for the computation of dose-averaged LET from microdosimetric quantities with Equation (3.9).

In this study, our weighted random sampling algorithm was optimised and the dimensions of the scoring volume were chosen accordingly, so that the results obtained could be considered equivalent to uniform ones, with relative differences generally lower than 6%.

Once optimised, the code was used to run various simulations with mono-energetic proton beams, with energies in the range $10 - 90$ MeV impinging on spherical sites of 1 µm and 10 µm diameter. The lower limit of the energy range was chosen to ensure that the short track segment condition, necessary to apply Equation (3.9), held for all the cases considered; while the upper limit of the energy range was determined by the Geant4-DNA physics list, which only allows calculations for proton energies lower than 100 MeV.

Since for mono-energetic proton beams the relation $\overline{L}_{\mathrm{D}} = \overline{y}_{\mathrm{F}}$ holds, frequency-averaged lineal energy values obtained with both sampling methods were used as a reference for the validation of the code and the comparison with dose-averaged

Table 3.6: Sampling efficiencies and computational times of the simulations performed with sites of 1 µm diameter. A total of 250 000 events (N_{sim}) in batches of 1000 were generated. The sampling efficiency has been computed as the ratio between the detected events (N_{det}, at least one energy deposition in the site) and the generated ones. The times reported refer to the simulation of one batch of 1000 events, where t_{R} is the actual time taken for the simulation and t_{E} is the extrapolated time that would be necessary to achieve the same statistics with uniform random sampling.

	Efficiency $N_{\mathrm{det}}/N_{\mathrm{sim}}$ [%]		Computational time per batch		
	weighted	uniform	weighted	uniform	
Energy [MeV]			t_{R}	t_{R}	t_{E}
10	100	38.4	1 h 31 min	3 h 46 min	$>$ 9 h
20	100	14.9	1 h 30 min	2 h 51 min	$>$ 19 h
40	100	2.6	2 h 5 min	2 h 43 min	$>$ 4 d
70	100	0.5	3 h 13 min	3 h 27 min	$>$ 30 d
90	100	0.2	3 d 15 h	3 d 15 h	$>$ 5 y

LET values obtained with Equation (3.9). Since the site dimensions considered were generally smaller than the maximum range of δ-rays emitted by the incident proton, the dose-averaged LET obtained with this equation was expected to be restricted. To prove this concept, microscopic $\overline{L}_{\mathrm{D}}$ values were compared with macroscopic ones, unrestricted, obtained with Equation (3.12).

While generally no evident problems emerged in the results obtained with the 10 µm diameter site, the 1 µm diameter site arose questions about the validity of Kellerer's formula, due to the fact that the $\overline{L}_{\mathrm{D}}$ curve obtained intersected the macroscopic unrestricted dose-averaged LET curve. This apparent contradiction was solved introducing the concept of *effective mean chord length* $\overline{l}^{*}_{\mathrm{F}}$, i.e., the mean chord length corresponding exactly to an energy imparted per event to the site equal to $\bar{\epsilon}_{\mathrm{F}}$. In general, $\overline{l}^{*}_{\mathrm{F}}$ should be equal to the true value $\overline{l}_{\mathrm{F}} = 2d/3$. However, this is not true in the simulations considered, and the effective value of the mean chord length not only differs slightly from the expected one, but varies with the impinging proton energy. This behaviour is probably related to the action of δ-ray influx, which affects the distribution of energy imparted to the site per event, slightly increasing the actual value of $\bar{\epsilon}_{\mathrm{F}}$ with respect to what would be obtained only by considering direct traversals of proton tracks through the site, especially for the highest energies.

By using the effective mean chord length values for the computation of frequency- and dose-averaged effective lineal energies, a general better agreement was observed, both between uniform and weighted random sampling results, and between $\overline{L}_{\mathrm{D}}$ and $\overline{y}^{*}_{\mathrm{F}}$ curves. Furthermore, the nature of restricted LET emerged clearly in this case, being all the $\overline{L}_{\mathrm{D}}$ values computed with Kellerer's formula below the macroscopic $\overline{L}_{\mathrm{D}}$ and generally lower for the 1 µm diameter site compared to the 10 µm one. Indeed,

the difference between the restricted dose-averaged LET values computed in the two site dimensions decreases as the energy increases, due to the fact that for the 10 µm diameter site the maximum range of δ-rays is comparable to the site dimensions for proton energies below 20 MeV. Therefore, the microscopic $\overline{L}_{\mathrm{D}}$ is initially unrestricted for the 10 µm diameter site, and approaches the curve of restricted dose-average LET obtained with the 1 µm diameter site as the energy increases.

3.6 Conclusions

A Monte Carlo code for the computation of microdosimetric distributions generated by proton track segments in liquid water was presented. Apart from the distribution of energy imparted per event, our code computes also the distribution of energy imparted per single proton collision, a feature that is foreseen to be included in an example of one of the next official releases of Geant4.
Two different sampling algorithms were implemented, uniform and weighted, the first serving as reference for the second, with the aim of obtaining an efficient and unbiased algorithm for the fast computation of microdosimetric distributions. By choosing appropriately the dimensions of the scoring volume, weighted sampling results could be considered as equivalent to uniform ones. However, the effect of the scoring volume thickness on the distribution of energy imparted per event obtained with weighted random sampling needs to be study more accurately, as the underlying mechanisms are not yet clear.

Various simulations were run to test the performances of the code, and to benchmark it, by comparing dose-averaged lineal energy results with dose-averaged LET values computed with Kellerer's formula, given by Equation (3.9). In this context, the concept of effective mean chord length was introduced, defined as the value of chord length corresponding exactly to an energy imparted to the site per event equal to $\overline{\epsilon}_{\mathrm{F}}$. A very good agreement between simulation results and theoretical expectations was met, with relative percentage differences always lower than 6%.
In the future, more studies are foreseen to test the robustness of the code against variations of site dimensions and shape. Indeed, the implementation of cylindrical sites would be highly interesting as many microdosimeters have this shape. Furthermore, the validity of Kellerer's formula and the performances of the code should be tested for higher proton energies, at least comparable to the ones used in clinical applications.

The results obtained with our code were used as a base for the definition of analytical microdosimetric models, whose description is given in [121, 122]. Finally, an application of the code is presented in Chapter 4, where it is used for the theoretical derivation of the RBE by means of the Microdosimetric Kinetic model.

Chapter 4

Irradiation of mono-layer cell cultures at the cyclotron radiobiology beam line

4.1 Introduction

In Chapter 2 the preparation of a radiobiology beam line at the cyclotron external beam line of the CNA was presented. This chapter, on its side, will focus on the first irradiation of cell samples carried out to test the performance of this beam line.

To this end, a collaboration was established with a research group of the Andalusian Molecular Biology and Regenerative Medicine Centre (Centro Andaluz de Biología Molecular y Medicina Regenerativa-CABIMER), who made available their cell lines, laboratories and expertise to carry out a parallel irradiation of cell cultures with protons and photons using the cyclotron radiobiology beam line and a ^{137}Cs irradiator, respectively.

During this experiment, Human Bone Osteosarcoma (U2OS) cells were irradiated with two doses (6 and 10 Gy), and the response to irradiation was studied in terms of DNA damage induction, through the analysis of γH2AX and RPA foci with immunofluorescence microscopy.

The most common way to study and compare the effects of different radiation qualities on cell cultures and tissues is to derive the RBE for a particular biological endpoint, usually chosen to be the 10% clonogenic survival, RBE_{10} [54]. Clonogenic essays, and the respective cell survival curves, are performed by irradiating a controlled number of cells ($\simeq 100$) with different doses and incubating them after irradiation for some time (approximately one week) to count for the remaining colonies. Then, cells are designated as survivors if they preserve their reproductive integrity after

irradiation, i.e., are able to form a colony with more than at least 50 cells.
With the irradiation setup proposed in Chapter 2, however, it was not possible to measure a proton cell survival curve, since the brief exposure of cells to air and the subsequent loss of sterile conditions enhanced the probabilities of bacterial infections, that could be propagated to other cultures in the incubator. In view of these considerations, and with the perspective of improving the setup to allow for the irradiation of cell cultures in a sterile environment, a theoretical derivation of the RBE was done, taking advantage of the microdosimetry code presented in Chapter 3 and of the Microdosimetric Kinetic Model (MKM) [69–71].

4.2 Materials and Methods

In this section, the main characteristics of the experiments and analysis carried out for the first irradiation of cell cultures at the cyclotron radiobiolgy beam line are presented. The U2OS cell line, which exhibits optimal characteristics for immunofluorescence microscopy [123], was used to study and compare the effects of different radiation qualities in the induction of γH2AX and RPA foci, indicators of specific damage and repair pathways of the DNA molecule.
In order to understand the experiments and the analysis performed in this chapter, a brief explanation of the main aspects of DNA structure and of the mechanisms of damage induction and repair are first given. Then the experimental setups for the irradiation of cell cultures, both with protons and photons, are described, followed by the procedures and protocols for the subsequent treatment and manipulation of the samples.
Finally, the steps followed for the theoretical derivation of the RBE of U2OS cells at 10% survival are described.

4.2.1 DNA damage induction and repair

The DNA is the main repository of the genetic information in the cells [124]. This macromolecule consists of two opposing strands of nucleotides linked by hydrogen bonds forming a double helical structure. Each strand is a linear chain of four bases, adenine (A), thymine (T), guanine (G) and cytosine (C), connected by sugar molecules and a phosphate group. Genetic information is encoded in the sequence of these bases, that can only bond in pairs: A with T and G with C. The two strands are therefore complementary. The DNA double helix is wrapped at regular intervals around some specific proteins called histones, forming the nucleosomes (see Figure 4.1). Other proteins are also linked to the DNA, and the ensemble of the DNA and its associated proteins is called chromatin. Finally, further levels of folding

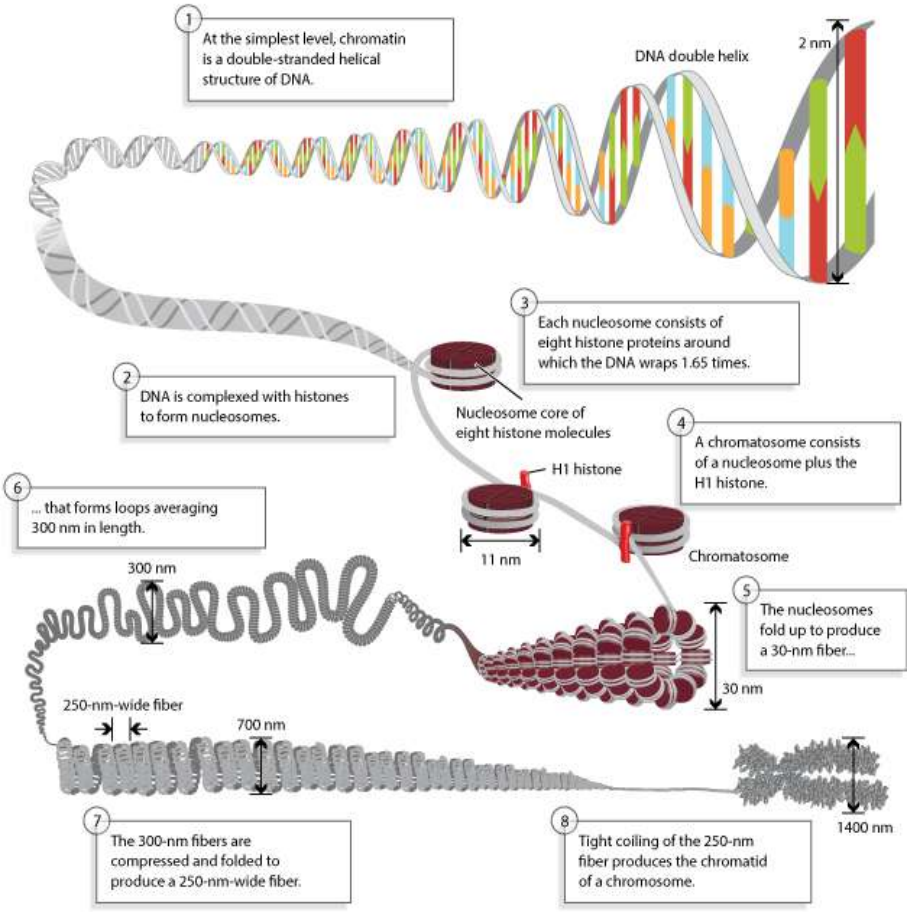

Figure 4.1: DNA packaging and structure of chromosomes (taken from [125]).

and looping make up the structure of the chromosomes.

Since the DNA is the largest molecule of the cell and is central to all cellular functions, it is also the principal target for radiation induced cell killing. Because of its importance, cells and organisms have developed a complex series of processes and pathways to ensure that the DNA remains intact and unaltered, including specialised repair systems detecting and repairing damages to bases, single strand breaks (SSBs) and double-strand breaks (DSBs).

The DNA damage response is a complex and coordinated system determining the cellular outcome following DNA damage, as that induced by ionising radiation. This response is characterised by various signalling pathways, each of them controlling a different effect on the cell, and can be divided into two parts: the sensors of DNA damage and the effectors of damage response. The sensors consist of a group

of proteins that actively survey the genome for the presence of damage. These proteins then signal this damage to three main effector pathways that together determine the outcome for the cell: (1) programmed cell death, (2) DNA repair or (3) temporary or permanent block in the progress of the cells through the cell cycle [46]. In the following, the main aspects of the response and repair pathways for DSBs are described.

The initial cellular response to DSBs is characterised by the gathering of a large number of different proteins to the sites of DNA damage, which can be visualised microscopically by staining these proteins with their antibodies. These clusters of proteins appear as subnuclear regions commonly referred to as ionising radiation induced *foci*. One of the earliest events known to occur in the DNA damage response is the phosphorylation of the H2AX histone, which takes place within 5-30 min after DSB induction [46]. This histone is distributed throughout the entire nucleus and becomes phosphorylated in a region that extends around the site of unrepaired DSBs. Its phosphorylated form, known as γH2AX, acts as a signal for the recruitment of the other proteins involved in damage repair. Therefore, the presence of γH2AX foci, which can be detected using microscopy, is a highly sensitive method for detecting the presence of individual DSBs in irradiated cells.

Once detected by the cell, two are the main repair pathways for DSBs:

1. the **Homologous Recombination (HR)**, which uses homologous undamaged DNA as the template to repair the DNA with the DSBs in it;

2. the **Non Homologous End Joining (NHEJ)**, which joins two DNA DSB ends together without requiring homologous DNA sequences.

The two pathways are quite different in the genes involved, the position in the cell cycle where they primarily act and in the speed and accuracy of repair. The rejoining of DNA ends by NHEJ is a fast and error-prone process and can occur at every stage of the cell cycle. On the contrary, HR requires the presence of a reference homologous DNA sequence to occur, being therefore more precise, but can only take place during the replication phases of the cell cycle (late S-phase and G_2-phase). In the process of HR, the Replication Protein A (RPA) plays a central role, being an universal response of the cell to any single-stranded region of the DNA. The RPA binds to the single-strand, starting a chain of events that eventually leads to HR [46]. Foci of the RPA protein can be stained and visualised microscopically with the immunofluorescence technique; co-localisation of RPA foci over γH2AX ones can be then studied as a marker for HR.

Table 4.1: Material and thickness of the components of the experimental setup traversed by the proton beam.

Element	Material	Thickness
Scattering foil	Aluminium	500 µm
Exit window	Mylar	100 µm
Window-IC distance	Air	26.3 cm
IC electrodes	Kapton	3×7.5 µm
IC active volumes	Air	2×6.75 mm
IC-sample distance	Air	2.5 cm
Cell layer	Water	11 µm

4.2.2 Experimental setup

The setup for the irradiation of cell cultures was the same as described in Section 2.2.3. A six-well plate was inserted in the sample holder, aligning the well hosting the cell culture with the ionisation chamber collimator. In order to monitor the dose delivered to the cell cultures, a charge-to-dose calibration curve was built using the measurements performed for the calibration of the EBT3 films in Section 2.3.2. To do so, a dedicated Monte Carlo simulation was run to derive the energy deposited in the layer of cells irradiated, assuming water as the cell material. A thickness of 11 µm was considered for the layer of U2OS cells, corresponding to the mean value of the thicknesses of cells in different phases of their cycle, measured with a confocal microscope. The different distances and materials traversed by the proton beam before impinging on the samples are listed in Table 4.1.

The charge-to-dose calibration curve obtained is reported in Figure 4.2, where a linear function has been fitted to the points.

Under these experimental conditions, protons reached the sample with an average kinetic energy of 13.2 MeV and 0.2 MeV standard deviation, resulting in a frequency-averaged LET in water of $\approx 3.8\,\mathrm{keV\,\mu m^{-1}}$. This energy was the highest achievable with a proper dose homogeneity over the sample surface (relative deviations lower than 4%), as described in Chapter 2.

Previous to irradiation, U2OS were grown over coverslips in a 6-well plate with Dulbecco's modified Eagle's (DMEM) medium (Sigma Aldrich, Merck KGaA, Darmstadt, Germany) supplemented with 10% fetal bovine serum (FBS, Sigma Aldrich, Merck KGaA, Darmstadt, Germany), 100 units $\mathrm{ml^{-1}}$ penicillin, 100 µg $\mathrm{ml^{-1}}$ streptomycin and 2 mmol $\mathrm{l^{-1}}$ L-glutamine at 37 °C in 5% CO_2.

Due to the low proton energy impinging on the target (residual range in water of ~ 2 mm), samples had to be irradiated without growth medium. Therefore, in order to limit as much as possible the time of exposure to air, only one well was used for

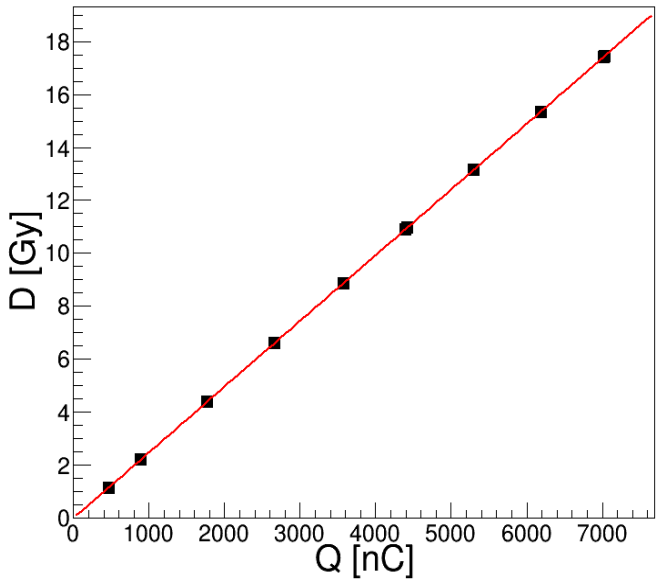

Figure 4.2: Charge-to-dose calibration curve. Experimental points have been fitted with a linear function of the form $y = p_0 + p_1 \cdot x$, where $p_0 = 2(1) \times 10^{-3}$ Gy and $p_1 = 2.48(1) \times 10^{-3}\,\mathrm{Gy\,nC^{-1}}$.

each plate, hosting 2 cell culture coverslips. Immediately before the irradiation with protons, the growth medium was removed; furthermore, the temperatures of the control room and of the experimental room were set to an average of 22 °C to limit the thermal shock.

Under these conditions, two samples of cell cultures were irradiated with approximately 6 and 10 Gy respectively. A third sample was kept as a control, undergoing the same manipulation as the other two but receiving no dose. Table 4.2 collects the charge readout of the ionisation chamber, the final absorbed dose and the overall time of exposure to air for each sample. The actual doses received by the samples, indeed, were slightly higher than the planned ones, due to the difficulties associated

Table 4.2: Experimental parameters of the cell culture irradiation with protons at the cyclotron radiobiology beam line. Absorbed doses are different from planned ones due to the manual stopping of beam irradiation.

Planned dose	Charge readout	Absorbed Dose	Air exposure time
0 Gy (control)	0 nC	0 Gy	5 min
6 Gy	2640 nC	6.56(3) Gy	7.7 min
10 Gy	4400 nC	10.93(5) Gy	8.3 min

to manually stop proton irradiation at an exact amount of charged collected in the ionisation chamber.

After the irradiation campaign, that took a total time of approximately 30 min, 1 ml of PBS was added to the samples to preserve them, before proceeding with the cell fixation and the preparation of samples for immunofluorescence analysis.

4.2.3 Irradiation of cells at the ^{137}Cs irradiator

Concomitant with the irradiation of the cell cultures with protons at the cyclotron radiobiology beam line, a parallel irradiation with photons was performed. To this end, a ^{137}Cs calibrated gamma irradiator (Biobeam GM 8000, Gamma-Service Medical GmbH, Leipzig, Germany), i.e., a fully protected irradiation device providing an optimum dose distribution, was used. This irradiator is hosted at the CABIMER building, and cells can be irradiated with their growth medium, avoiding extra stress related to transport and exposure to air. As for the irradiation with protons, 3 dose points were acquired: controls (0 Gy), 6 Gy and 10 Gy.

Different photon energies are subject to different LET values, defined via the respective secondary electrons. In the case of the ^{137}Cs irradiator, a γ-ray of 662 keV is emitted by the ^{137m}Ba generated from the β decay of ^{137}Cs, resulting in a LET in water of approximately 0.35 keV µm^{-1} [126].

4.2.4 Immunofluorescence microscopy

Immunofluorescence is a technique used for light microscopy with a fluorescence microscope. This technique uses the specificity of antibodies to their antigen to attach fluorescent dyes to specific biomolecules targets within a cell, therefore allowing the visualisation of the distribution of these molecules through the sample.

In order to allow for the passage of large molecules such as antibodies into intracellular structures, and to be able to visualize them under the microscope, the subsequent protocol was followed.

Pre-extraction with buffer After irradiation, coverslips were washed once with cold PBS and transferred to a 24-well plate. Then, 500 µl of freshly prepared cold pre-extraction buffer (25 mmol l^{-1} Tris-HCl pH 6.8, 50 mmol l^{-1} NaCl, 1 mmol l^{-1} $MgCl_2$, 300 mmol l^{-1} sucrose and 0.5% Triton X-100) were added to each well and removed after 5 min on ice. Antibody proteins are too large to pass through cell membranes without prior permeabilisation; Triton X-100 is a widely used detergent that efficiently dissolves cell membranes without disrupting protein-protein interactions, granting access to the nuclear interior.

Table 4.3: Primary and secondary antibodies used for immunofluorescence analysis in this study.

Protein	Antibody	Concentration	Supplier	Reference
		Primary		
γH2AX	rabbit	1:1000	Cell Signaling Technologies (Leiden, NL)	2555L
RPA	mouse	1:500	Abcam (Cambridge, UK)	ab2175
		Secondary		
γH2AX	Alexa Fluor 488 goat anti-rabbit (green)	1:500	Invitrogen ThermoFisher (Waltham, MA, USA)	A11034
RPA	Alexa Fluor 594 goat anti-mouse (red)	1:500	Invitrogen ThermoFisher (Waltham, MA, USA)	A11034

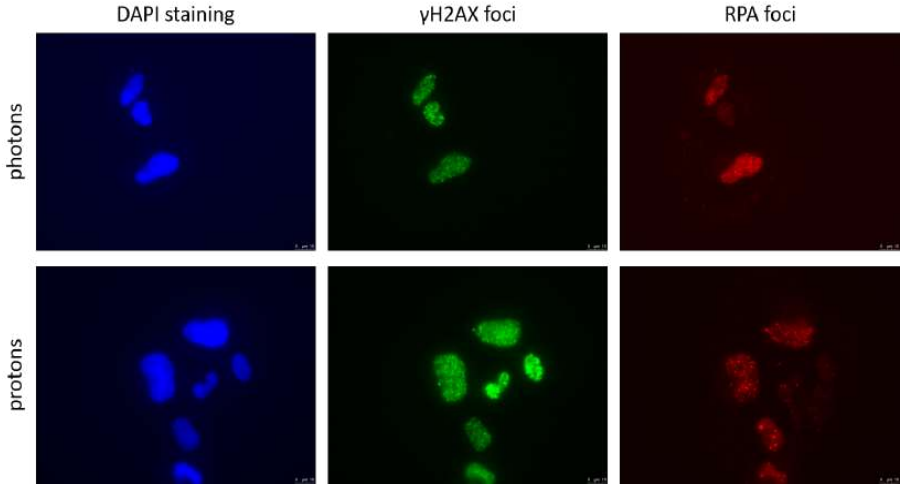

Figure 4.3: Representative pictures of the images used for the γH2AX and RPA foci quantitative analysis. Cells irradiated with photons (top) and protons (bottom) with a dose of 10 Gy and 10.93 Gy respectively. DAPI staining images (on the left) identify the cell nucleus contour, where γH2AX foci (centre) and RPA foci (right) accumulate after irradiation in correspondence to DNA DSBs.

Cell fixation The goal of fixation is to preserve cell morphology as close as possible to its native state during immunostaining protocols. After pre-extraction, the wells were washed again with cold PBS and then fixed, filling them with 4% paraformaldehyde (Santa Cruz Biotechnology, Dallas, Texas, USA) for 15 min on ice.

Blocking Following fixation, blocking prevents primary and secondary antibodies from binding to non-specifical proteins, by masking potential sites of generic interaction. A blocking solution of 5% FBS in PBS was used to this purpose, leaving the samples for 1 h at room temperature.

Antibodies For the purpose of this experiment, an indirect immunofluorescence technique was used. This technique uses two antibodies: a primary unlabelled antibody that specifically binds to the target molecule and a secondary antibody, which carries the fluorophore, recognises the primary antibody and binds to it. The primary and secondary antibodies used for γH2AX and RPA foci detection are listed in Table 4.3. A self-adhesive film was glued to the microplate to host drops of primary antibody solution. Then coverslips were placed on the antibody solution drops upside down, so that cells got in touch with the antibodies. The microplates with the coverslips were incubated overnight at 4 °C, then the coverslips were washed with PBS and incubated again with secondary antibodies for 1 h at room temperature in the dark, following the same procedure. Excess reagents and antibodies need to be removed following each incubation. Therefore, cells were washed with PBS and dehydrated with successive washes of 70% and 100% ethanol.

Mounting Finally, coverslips were mounted on microscope slides using Vectashiled mounting medium (Vector Laboratories, Burlingame, California, USA) containing DAPI, a fluorescent marker that attaches to regions with DNA, thus permitting the visualisation of nuclei borders.

To visualise and acquire images, a Leica DM600 microscope (Leica microsystems, Wetzlar, Germany) was used, with a HCX PL APO 63x/1.4 OIL objective. Images of at least 200 cells were taken for every experimental condition: an example of these images is shown in Figure 4.3. Later on, images were processed and analysed with the MetaMorph Microscopy and Image Analysis Software (Molecular Devices LLC, San Jose, California, USA), which enables background subtraction, the selection of fluorescent regions and the quantification of foci thanks to a number of built-in applications.

Table 4.4: Parameters for the identification of foci with the built-in application *Granularity* implemented in the MetaMorph software.

Image	Intensity above background		Dimension [min–max] pixels	
	Foci	Nucleus	Foci	Nucleus
γH2AX	300	300	[4–20]	[80–300]
RPA	800	300	[4–20]	[80–300]

Analysis with MetaMorph Software

For the quantitative analysis of the images acquired with the microscope, the subsequent procedure was followed in the MetaMorph software.

1. First, two images were opened at a time, the γH2AX- or RPA-stained image and the corresponding DAPI-stained one.

2. Both images were then converted to black and white (16 bit format) and their background subtracted.

3. A threshold was then selected in the DAPI-stained image to identify the contour of the nuclei and their inner region, where γH2AX and RPA foci are located. Once the threshold was selected, a binary image was created highlighting the nuclei regions.

4. The binary image created from the DAPI-stained image was then used as a mask, superimposing it to the γH2AX- or RPA-stained image with subtracted background.

5. Finally the foci were identified from the masked image with the built-in application *Granularity*, by selecting their intensity above background and their pixel size.

Once established, the parameters for the identification of foci were kept fixed for all the different series of images. Their values are collected in Table 4.4.
Finally, a spreadsheet file was generated, listing the information for every cell nucleus identified in the images, i.e., number of foci, total area occupied by foci, foci average and total intensity, nuclear area and nuclear average and total intensity.

4.2.5 Theoretical computation of RBE from microdosimetry

As described in Section 1.3.3, the MK model assumes that the α parameter of the Linear Quadratic model for low-LET radiation is proportional to the dose mean lineal energy $\overline{y}_{\mathrm{D}}$, and inversely proportional to the squared radius of the

site considered, called domain. Therefore, in principle, once determined the linear quadratic parameters for a reference radiation and the characteristic dimension of the domain for a specific cell line, it should be possible to derive the LQ parameters for proton irradiation at a given $\overline{y}_{\mathrm{D}}$ value.

This concept was applied to the U2OS cell line used for the first radiobiology experiments at the cyclotron facility to derive the theoretical survival curve under proton irradiation. In order to do so, U2OS clonogenic survival data under photon irradiation, collected by different groups of the CABIMER, were used to build a photon survival curve and extract the reference α_γ and β_γ parameters. Then, assuming the radius of the domain $r_{\mathrm{d}} = 0.42\,\mu\mathrm{m}$, equal to that of HSG cells [75], a commonly used cell line for radiobiological studies derived from a human cervix carcinoma, and using the microdosimetry code described in Chapter 3 to calculate the value of $\overline{y}_{\mathrm{D}}$, it was possible to derive a rough estimation of the expected cell survival curve under proton irradiation.

Photon survival curve

Clonogenic survival data for U2OS cells, collected by different research groups of the CABIMER, were used to build a cell survival curve and extract the α_γ and β_γ of the linear quadratic model under photon irradiation.

The data were fitted separately depending on the operator that collected them, as shown in Figure 4.4a, and final values of α_γ and β_γ were obtained computing the average and standard deviation of the respective parameters obtained from the different fits.

Figure 4.4b shows the linear quadratic curve (solid line) obtained with the average α and β parameters, whose values are $\alpha_\gamma = 0.20 \pm 0.03\,\mathrm{Gy}^{-1}$ and $\beta_\gamma = 0.06 \pm 0.03\,\mathrm{Gy}^{-2}$, with an α/β ratio of $3.3 \pm 1.7\,\mathrm{Gy}$. In this figure, the dashed lines correspond to the maximum range of variation of the α and β parameters, and were obtained with $(\alpha_\gamma - \sigma_\alpha, \beta_\gamma - \sigma_\beta)$ for the upper curve and $(\alpha_\gamma + \sigma_\alpha, \beta_\gamma + \sigma_\beta)$ for the lower curve. The α and β parameters obtained for U2OS cells are compatible, within the error, with HSG ones ($\alpha_{\mathrm{X}}(\mathrm{HSG}) = 0.19\,\mathrm{Gy}^{-1}, \beta_{\mathrm{X}}(\mathrm{HSG}) = 0.05\,\mathrm{Gy}^{-1}$ [75]), being both cell lines made of epithelial adherent cells. Therefore, the assumption of the same domain size $r_{\mathrm{d}} = 0.42\,\mu\mathrm{m}$ for U2OS seemed to be reasonable.

Once known the dimension of the domain and the $(\alpha_\gamma, \beta_\gamma)$ parameters, it is possible to extract the value of the parameter α_0 of the MK model. To do so, however, information about the dose-averaged lineal energy for the radiation type considered is also necessary. Figure 4.5 reports the dose-averaged lineal energy distribution for 662 keV photons emitted by ^{137}Cs measured with a tissue equivalent proportional counter, whose average value is $\overline{y}_{\mathrm{D},\gamma} = 1.85\,\mathrm{keV}\,\mu\mathrm{m}^{-1}$ [127].

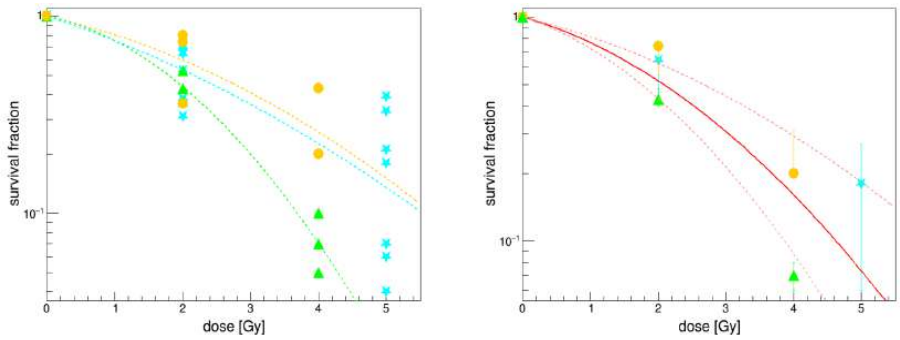

Figure 4.4: **(a)** Clonogenic survival data for U2OS irradiated with the ^{137}Cs-irradiator, collected by different research groups from CABIMER. The colours and marker shapes distinguish the different sets of data, separated according to the operator that collected them. Each set of data was fitted separately (dashed lines) and final values of α_γ and β_γ parameters were computed as average values of the parameters obtained from these fits. **(b)** Cell survival curve (solid line) obtained with the average α_γ and β_γ parameters resulting from the fit of the experimental data. The dashed lines correspond to the maximum range of variation of α and β, and are obtained with $(\alpha_\gamma - \sigma_\alpha, \beta_\gamma - \sigma_\beta)$ for the upper curve and $(\alpha_\gamma + \sigma_\alpha, \beta_\gamma + \sigma_\beta)$ for the lower curve. In this plot, the experimental data are summarised by reporting the median value for each set, with the 25th (lower) and 75th (upper) percentiles as asymmetric error bars.

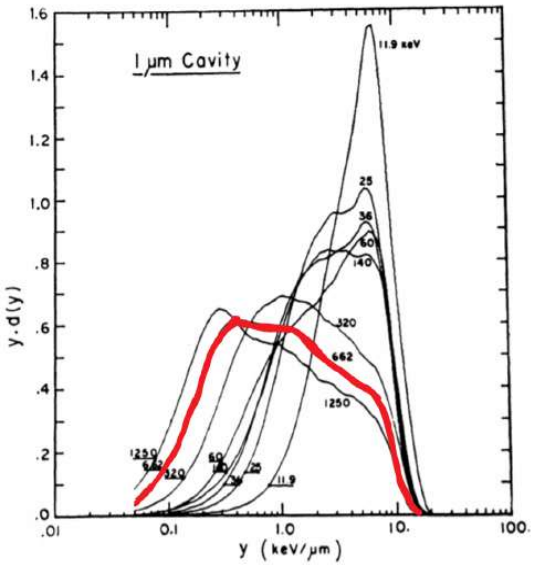

Figure 4.5: Distribution of $y\,d(y)$ as a function of y for a 1 µm diameter site at eight photon energies [127]. The highlighted curve represents the distribution for 662 keV photons emitted by ^{137}Cs.

Gathering all this information, and knowing that $\beta_0 = \beta_\gamma$ the value of α_0 could be computed from Equation (1.36) as follows:

$$\alpha_0 = \alpha_\gamma - \beta_\gamma \frac{\overline{y}_{\mathrm{D},\gamma}}{\rho \pi r_{\mathrm{d}}^2} = 0.16 \pm 0.03\,\mathrm{Gy}^{-1}. \tag{4.1}$$

Dose-averaged lineal energy computation from the Monte Carlo code

The microdosimetry code described in Chapter 3 allows for the computation of microdosimetric quantities in water for any incident energy distribution and for spherical sites with various sizes. In order to reproduce the experimental conditions presented in Section 4.2 as realistically as possible, a simulation was run using as incident energy distribution the fluence spectrum of protons coming out from the ionisation chamber, and converting the air distance between the chamber and the cell layer (2.5 cm) into a water equivalent thickness. To do so, the following formula was applied [128]:

$$t_{\mathrm{w}} = t_{\mathrm{m}} \frac{\rho_{\mathrm{m}} \overline{S}_{\mathrm{m}}}{\rho_{\mathrm{w}} \overline{S}_{\mathrm{w}}}, \tag{4.2}$$

where $t_{\mathrm{m/w}}$, $\rho_{\mathrm{m/w}}$, and $\overline{S}_{\mathrm{m/w}}$ identify the thickness, mass density and average mass stopping power of the target material and water respectively. The mean energy of protons coming out from the ionisation chamber is 13.3 MeV, and corresponds to a mass stopping power of approximately $31.9\,\mathrm{MeV\,cm^2\,mg^{-1}}$ in air ($\overline{S}_{\mathrm{m}}$) and $36.3\,\mathrm{MeV\,cm^2\,mg^{-1}}$ in water ($\overline{S}_{\mathrm{w}}$), resulting in a water equivalent thickness $t_{\mathrm{w}} = 26.5\,\mu\mathrm{m}$. Following these considerations, a simulation was run setting $Z_{\mathrm{S}} = 11\,\mu\mathrm{m}$ and $R_{\max} = t_{\mathrm{w}} + Z_{\mathrm{S}}/2 = 32\,\mu\mathrm{m}$, with a site diameter of 0.84 µm.

4.3 Results

4.3.1 Irradiation of U2OS cell cultures

Before proceeding with the actual analysis of nuclear foci with the MetaMorph software, a preliminary visual analysis was performed to derive the percentage of positive cells for the different irradiation conditions, where *positive* means with a number of clearly distinguishable foci equal or greater than 10. The same analysis was then performed with the results extracted from MetaMorph, to check for the proper identification of foci by the software.

The results of this analysis and the comparison between visual and automated counting are collected in Table 4.5. For the sake of simplicity, in the following the labels 0 Gy, 6 Gy and 10 Gy will be used to identify the different irradiations performed both with photons and with protons, keeping in mind that the actual

Table 4.5: Percentage of positive cells after proton and photon irradiation. Results obtained from the visual analysis of immunofluorescence images are compared with the results extracted from the analysis of the images with MetaMorph.

Dose [Gy]	photons	protons	photons	protons
Visual	γH2AX		RPA	
0	0%	0%	13%	7%
6	100%	100%	11%	36%
10	97%	100%	50%	48%
MetaMorph	γH2AX		RPA	
0	1.4%	4%	35%	17%
6	98%	97%	17%	24%
10	91%	97%	48%	40%

dose received by the samples irradiated with protons was slightly higher (6.56 Gy and 10.93 Gy respectively, see Table 4.2 and related explanation).
In general, the visual and the automated analysis with MetaMorph gave compatible results in what concerned the recognition of positive cells. The only anomalous result was the one associated with RPA foci in the controls for the photon irradiation, which were in higher number than what could be normally expected for non-irradiated cells.

When comparing the different effects of proton and photon irradiation in what respects damage induction and response in terms of γH2AX and RPA foci, various parameters can be taken into account. First, the number of foci per nucleus, which in principle is expected to increase for increasing doses for both radiation qualities. However, the higher LET of the 13.2 MeV protons with respect to photons could result in a more clustered damage, possibly leading to an overlapping of foci, which could decrease their absolute number. Therefore, the pixel average size and the total intensity of foci per nucleus could give additional information to highlight the differences in energy deposition patterns between photon and proton radiation. In Figure 4.6 and Figure 4.7 the distributions of γH2AX and RPA foci number, average size and intensity are plotted, respectively, for the different radiation qualities.
In Figure 4.8 and Figure 4.9 the median values of the distributions shown in Figure 4.6 and Figure 4.7 are plotted as a function of the dose together with their uncertainties, considering only positive cells. For the computation of the uncertainties associated to the median values, their distances to the 25th and 75th percentile of the corresponding distributions were computed. The data relative to the irradiations with 6 Gy and 10 Gy were normalised to their controls in order to directly compare proton and photon results independently from the initial foci background.

No evident differences between the two radiation qualities emerged from the compari-

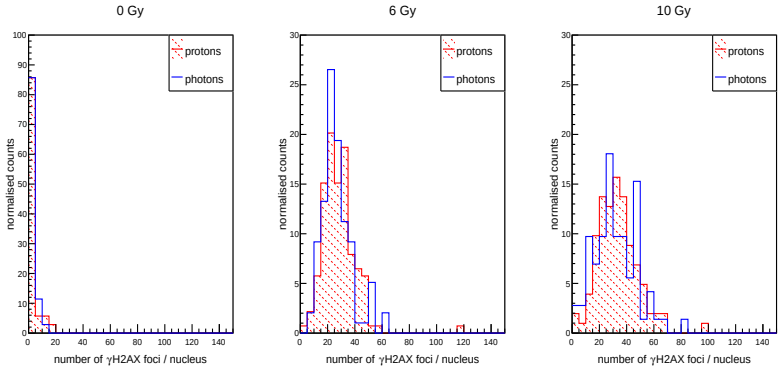

(a) Distribution of the **number of γH2AX foci per nucleus**

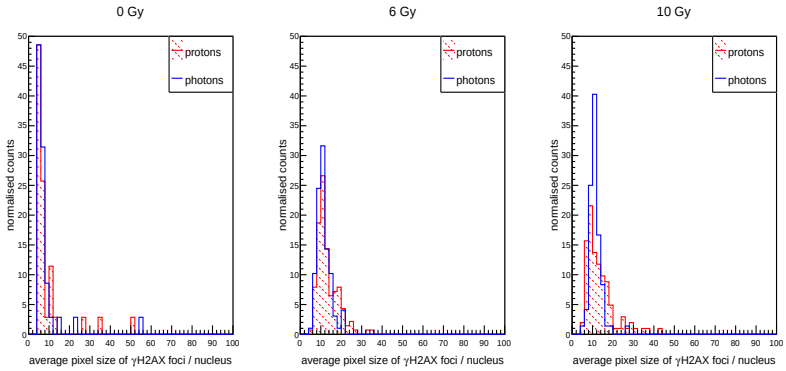

(b) Distribution of the **average pixel size of γH2AX foci per nucleus**

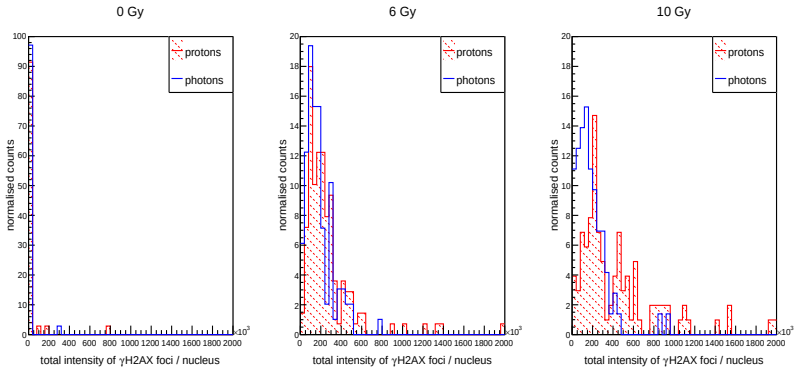

(c) Distribution of the **total intensity of γH2AX foci per nucleus**

Figure 4.6: Distribution of γH2AX foci number **(a)**, average size **(b)** and total intensity **(c)** after irradiation with photons (blue) and protons (shaded red).

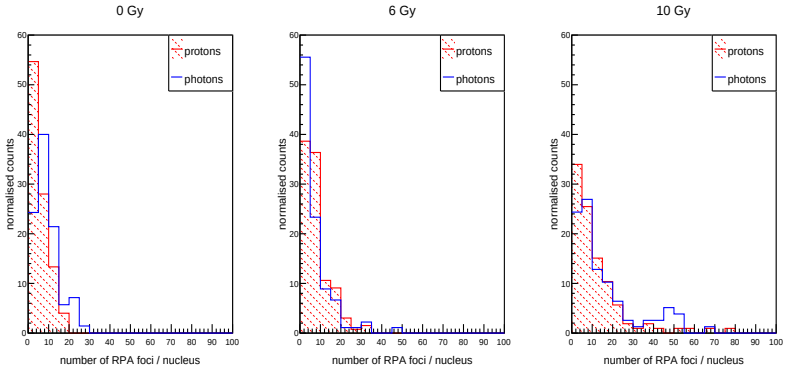

(a) Distribution of the **number of RPA foci per nucleus**

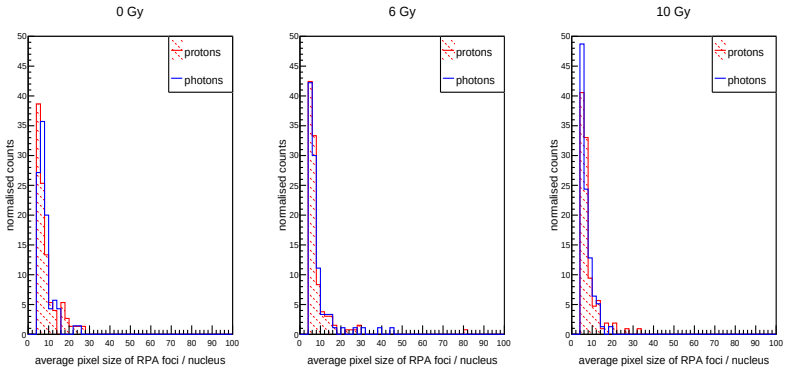

(b) Distribution of the **average pixel size of RPA foci per nucleus**

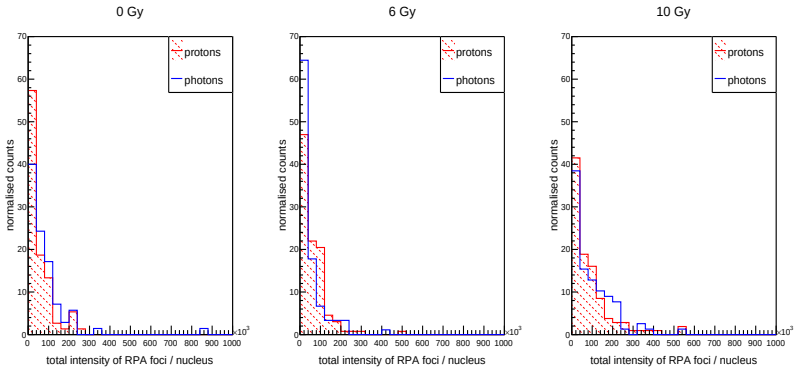

(c) Distribution of the **total intensity of RPA foci per nucleus**

Figure 4.7: Distribution of RPA foci number **(a)**, average size **(b)** and total intensity **(c)** after irradiation with photons (blue) and protons (shaded red).

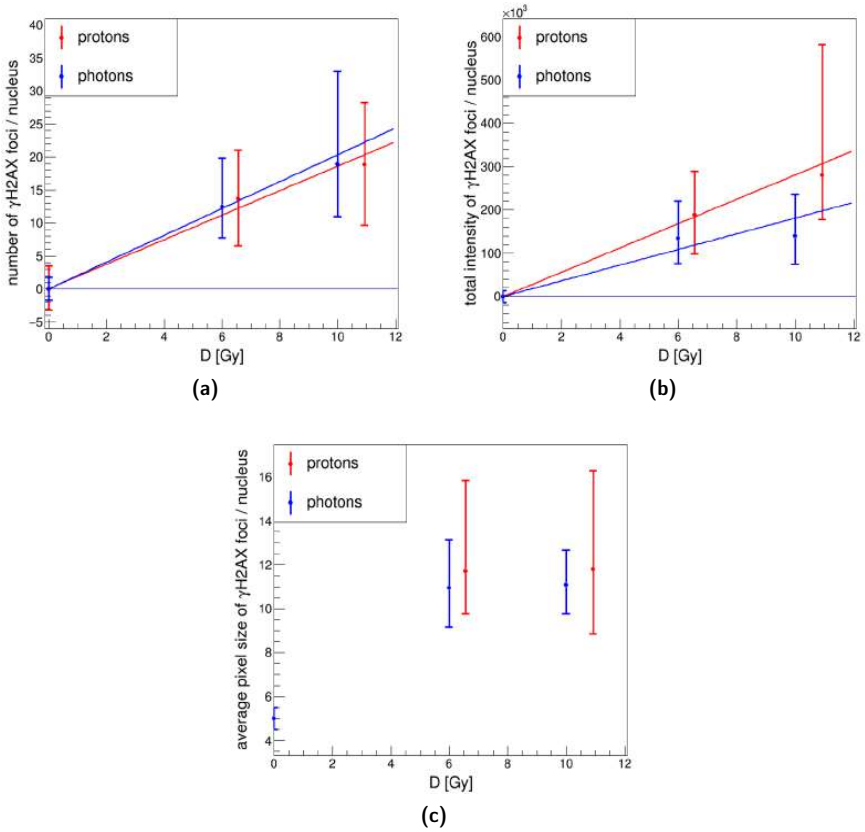

Figure 4.8: Median **(a)** number of γH2AX foci, **(b)** total foci intensity and **(c)** average foci pixel size per positive nucleus (more than 10 foci), as a function of the dose after proton (red) and photon (blue) irradiation. The asymmetric uncertainty intervals associated to the experimental points correspond to the 25th (lower) and 75th (upper) percentile of the distributions in Figure 4.6. The experimental points for the number of foci and total intensity are reported normalised to their controls and fitted with a linear function.

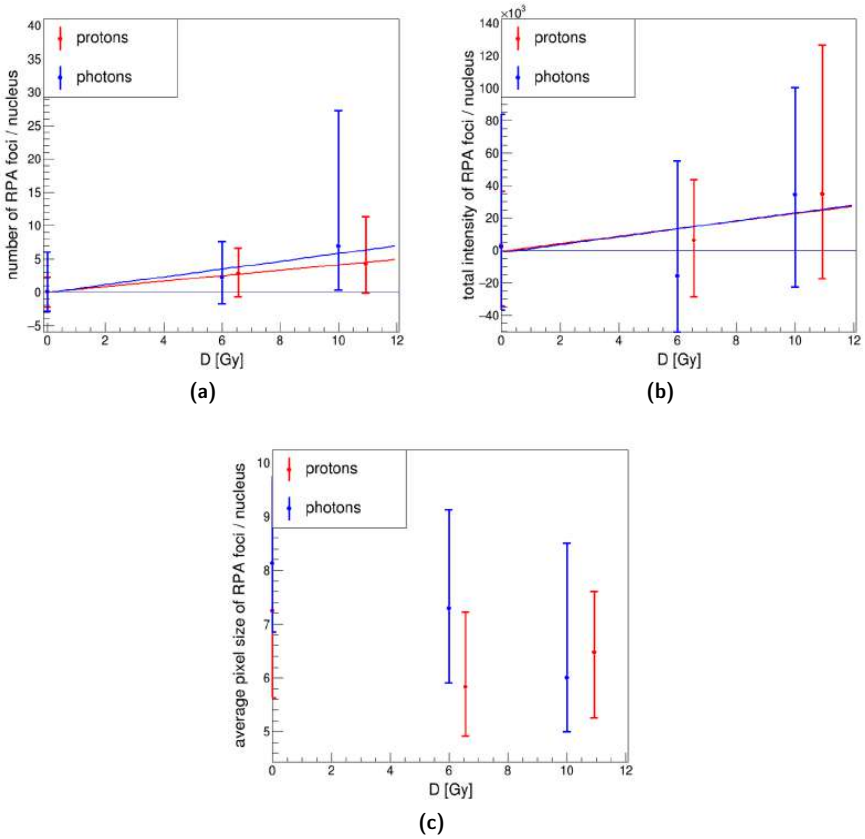

Figure 4.9: Median **(a)** number of RPA foci, **(b)** total foci intensity and **(c)** average foci pixel size per positive nucleus (more than 10 foci), as a function of the dose after proton (red) and photon (blue) irradiation. The asymmetric uncertainty intervals associated to the experimental points correspond to the 25th (lower) and 75th (upper) percentile of the distributions in Figure 4.6. The experimental points for the number of foci and total intensity are reported normalised to their controls and fitted with a linear function.

son of the number of γH2AX foci per nucleus. However, the results obtained seemed to indicate a slight dependence on the incident particle of the total intensity and average size of foci per nucleus, which was anyway smaller than the errors associated to the individual points. On the other side, none of the RPA foci distributions showed any dependence on the radiation type, and the increase in the number, total intensity and average size of foci per nucleus with dose was less pronounced.

4.3.2 Derivation of RBE_{10} from the MKM

The distributions of energy deposited in the cell layer per event, $\epsilon^2 f(\epsilon)$, obtained both with uniform and weighted random sampling are plotted in Figure 4.10.

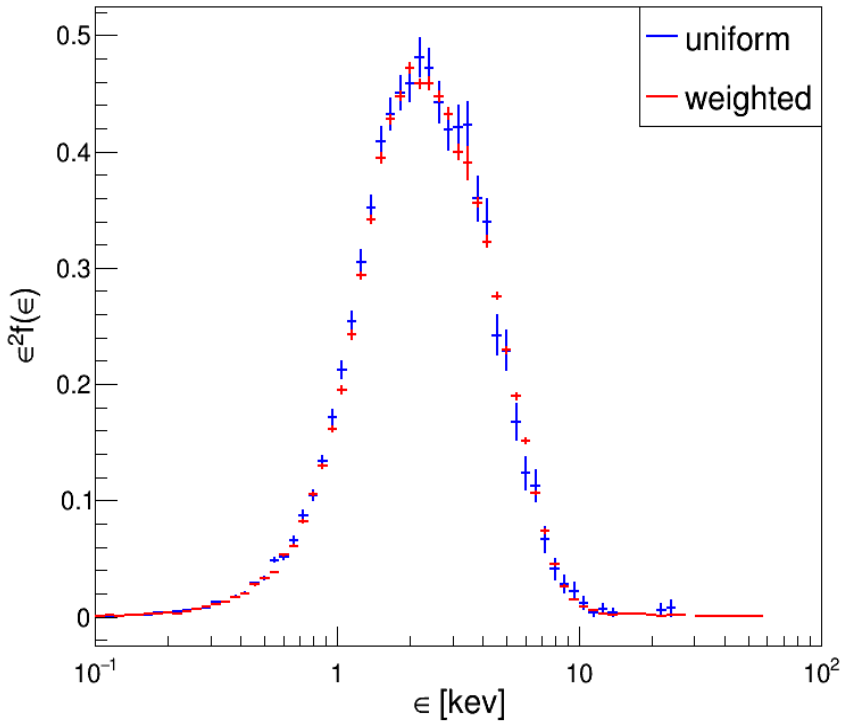

Figure 4.10: Distribution of $\epsilon^2 f(\epsilon)$ as a function of ϵ for a 0.84 µm diameter site at a proton energy of 13.2 MeV.

The values of the dose-averaged energy deposited per collision, effective mean chord length and resulting dose-averaged lineal energy transfer, for the two sampling methods, are listed in Table 4.6.

Table 4.6: Dose-averaged energy deposited per event, effective mean chord length and dose-averaged lineal energy computed with the microdosimetry Monte Carlo code (see Chapter 2) for the U2OS cell layer with uniform and weighted random sampling.

	$\bar{\epsilon}_D$ [keV]	$\bar{l}_F^*$ [µm]	$\bar{y}_D$ [keV µm^{-1}]
uniform	2.67 ± 0.08	0.521 ± 0.009	5.1 ± 0.2
weighted	2.709 ± 0.006	0.5243 ± 0.0005	5.17 ± 0.01

Since $Z_S >> 2d$ the results obtained with the two sampling methods were completely equivalent, and only weighted random sampling results are presented in the following discussion. Once obtained the value of the dose-averaged lineal energy of protons in the site, $\bar{y}_{D,p} = 5.17\,\text{keV}\,\mu\text{m}^{-1}$, the parameter α_p of the theoretical proton survival curve could be obtained with Equation 1.36 as follows:

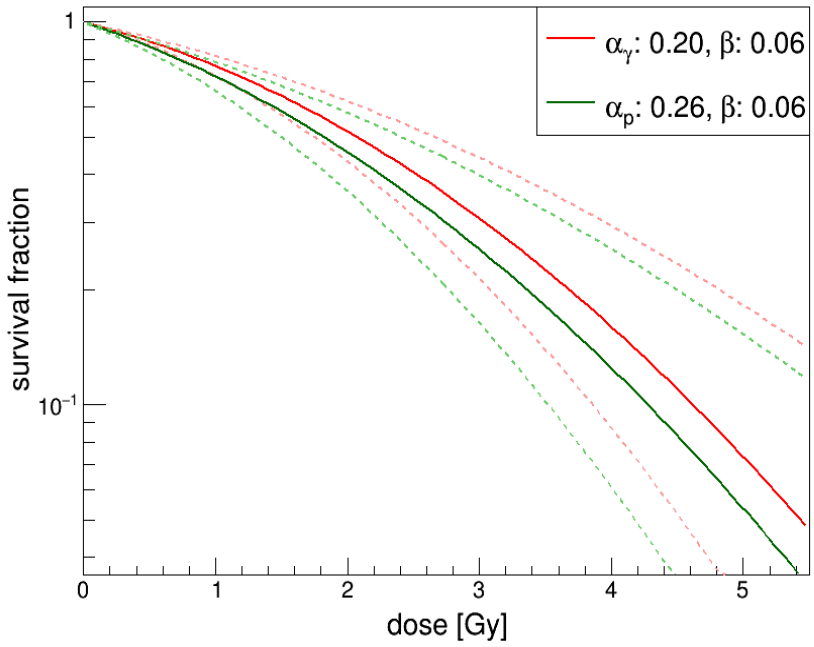

Figure 4.11: Theoretical U2OS cell survival curve for proton irradiation (green solid line) derived from the MK model and compared with the experimental survival curve for photon irradiation (red solid line). The dashed lines correspond to the maximum range of variation of the α and β parameters for each of the radiation qualities considered.

$$\alpha_{\mathrm{p}} = \alpha_0 + \beta_0 \left(\frac{\overline{y}_{\mathrm{D,p}}}{\rho \pi r_{\mathrm{d}}^2} \right) = 0.26 \pm 0.06\,\mathrm{Gy}^{-1}, \tag{4.3}$$

where $\alpha_0 = 0.16 \pm 0.03\,\mathrm{Gy}^{-1}$ and $\beta_0 = 0.06 \pm 0.03\,\mathrm{Gy}^{-2}$ (see Section 4.2.5).

Figure 4.11 shows the theoretical proton survival curve derived from the MK model (green solid line), with its respective maximum range of variation (green dashed lines), compared to the experimental photon survival curve (red lines). From the comparison between the photon and proton survival curves it was possible to extract the expected RBE value at 10% survival, or RBE_{10}:

$$\mathrm{RBE}_{10} = \frac{-\alpha_\gamma + \sqrt{\alpha_\gamma^2 - 4\beta_\gamma \ln 0.1}}{-\alpha_{\mathrm{p}} + \sqrt{\alpha_{\mathrm{p}}^2 - 4\beta_{\mathrm{p}} \ln 0.1}} = 1.1 \pm 0.5, \tag{4.4}$$

which was ~ 1.1, as expected for the proton energy considered and in agreement with the results obtained from the comparison of γH2AX and RPA foci distributions for photon and proton irradiation.

4.4 Discussion

The study presented in this chapter showed the potential of performing cell irradiations for exploring the RBE of protons, and presented the feasibility of the setup proposed in Chapter 2 to produce proton beams for radiobiology experiments. To test the performance of this setup, a preliminary irradiation of U2OS cell cultures was performed, with the aim of investigating the differences in damage response of this cell line to 13.2 MeV proton and photon irradiation (LET of $\approx 3.8\,\mathrm{keV\,\mu m^{-1}}$ and $\approx 0.35\,\mathrm{keV\,\mu m^{-1}}$, respectively).

No significant differences in the response to the two radiation qualities emerged in terms of the percentage of γH2AX and RPA positive cells; and comparable results were obtained by the visual and software analysis of immunofluorescence images.

The distributions of the number of γH2AX and RPA foci per nucleus in Figure 4.6a and Figure 4.7a did not differ significantly after proton and photon irradiation for the doses considered. However, a slight difference emerged in the total intensity of γH2AX foci per nucleus, being the intensity of foci higher for protons at the same level of absorbed dose (see Figure 4.8b), probably indicating a higher and more localised concentration of DSBs per incident particle. This difference, nevertheless, was in any case smaller than the error associated to the individual points, being necessary more measurements and data to confirm the tendency observed. On the contrary, no dependence on the radiation quality was observed for RPA foci.

The pixel size of γH2AX foci seemed to increase significantly after irradiation, but its median value remained approximately constant, within the error bars, independently on the dose. Proton induced foci appeared to be generally larger, but no definite conclusion could be made due to the uncertainties observed. Finally, the pixel size of RPA foci was almost constant for both radiation qualities and for all doses, showing a decreasing tendency for higher doses. Some works suggest that proton irradiation is more likely to activate the HR repair pathway than photon irradiation [129–132], due to the higher severity of the DNA damage induced. As explained in Section 4.2.1, the RPA is an universal response to any single-stranded region of the DNA and activates a chain of events that eventually leads to HR. Therefore, some extra information about the different outcomes of the irradiation could be obtained from the study of the co-localisation of γH2AX over RPA foci, which is a marker for HR. Even if foreseen, this study could not be accomplished due to the extraordinary measures introduced with the lockdown associated to COVID-19 and the subsequent limited access to laboratories, but it is planned as a next step.

The results just presented were, in general, not unexpected, since in the range of LET considered for this preliminary experiment, no major differences have been reported in the dependence of the biological effect on the LET [47]. Furthermore, to

extract significant conclusions from this comparison, other experimental data should be collected, considering more dose points, increasing the statistics and comparing different cell lines. In this context, the dependence of radiobiological effects on the LET could also be explored with our setup, by further degrading the incident beam energy.

In order to compute a rough estimation of the expected RBE for the cell line and proton LET considered in this experiment, the MK model was applied to derive the theoretical proton survival curve. With this purpose, a reference photon survival curve in the dose range $0 - 5\,\mathrm{Gy}$ was built, taking advantage of clonogenic survival data provided by different research groups of the CABIMER. Due to the various operators involved and the difficulties in counting survivor colonies for the higher doses, these data showed a large variability. Therefore, the set of data were fitted separately and final α_γ and β_γ parameters were computed as the average of the resulting fit parameters, accounting for the dispersion of data by considering their maximum range of variability. Knowing the LQ model parameters for photon irradiation and assuming $r_\mathrm{d} = 0.42\,\mu\mathrm{m}$, it was possible to extract the α_0 and β_0 values of the MK model, to be used for the derivation of α_p and β_p for proton irradiation. To do so, the Monte Carlo code developed for the computation of microdosimetric quantities, described in Chapter 3, was used to extract the value of $\overline{y}_{\mathrm{D,p}}$ in the cell layer. A proton survival curve with $\alpha_\mathrm{p} = 0.26 \pm 0.06\,\mathrm{Gy}^{-1}$ and $\beta_\mathrm{p} = 0.06 \pm 0.03\,\mathrm{Gy}^{-1}$ was obtained, resulting in an RBE at 10% survival approximately equal to the value of 1.1 used in clinical proton therapy. This result agrees with the experimental observation that the number of γH2AX and RPA foci does not vary with the radiation type, for the proton energy considered.

4.5 Conclusions

To test the performance of the cyclotron radiobiology beam line, a preliminary irradiation of U2OS cell cultures was conducted, with success. A concomitant irradiation with photons and protons was carried out, to compare the damage response of the cell cultures to the two radiation qualities.

At the proton LET considered ($3.8\,\mathrm{keV}\,\mu\mathrm{m}^{-1}$ in water) no major differences were expected in terms of damage response, since the RBE of protons at those energies is close to 1, as emerged also from the theoretical estimation of the RBE_{10} with the MK model. The results obtained for the distributions of γH2AX and RPA foci confirmed the expectations and, apart from a slight increase of the total intensity of γH2AX foci per nucleus after proton irradiation, no significant differences were observed between the two radiation qualities. This result, however, served as a proof of the validity of the cyclotron beam line for radiobiology experiments, since the

irradiation conditions did not alter the outcome of the experiment and the cells did not suffer from the stress of transportation, temperature variations and exposure to air.

Furthermore, a system to irradiate the cell cultures without the necessity of removing their growth medium before the irradiation is currently under study. Indeed, this would allow to investigate the kinetics of repair and to build clonogenic survival curves. One possible solution would be to grow the cell cultures on wells with a very thin bottom, in order to allow for the irradiation from behind with minimum energy loss. In this way, cells could be maintained in a sterile environment during the whole irradiation process, and then re-seeded and incubated to study the effects of radiation in time.

Chapter 5

Conclusions and perspectives

5.1 Final remarks

In clinical practice, proton beam therapy is based on the use of a generic RBE of 1.1, an assumption justified by the fact that the magnitude of RBE variations with treatment parameters is small relative to the uncertainties associated to RBEs [17]. However, the use of this generic, spatially invariant RBE within tumours and normal tissues disregards the evidence that proton RBE varies with linear energy transfer, physiological and biological factors and clinical endpoint. Furthermore, recent studies suggest that not taking into account RBE variations in proton therapy treatments could increase the dose delivered to organs at risk in the vicinity of the target volume, leading to possible toxicity [57–59, 107]. Taking advantage of the monotonic dependence of the RBE on LET, various efforts have been done to optimise LET distributions in treatment planning by introducing dose-averaged LET objective functions [113, 133], with the aim of mitigating the impact of RBE uncertainties in treatment planning decisions.
The thesis presented here fitted in this context, and faced the topic of proton RBE from two different perspectives:

1. experimentally, by designing and mounting a radiobiology beam line for the irradiation of mono-layer cell cultures with low energy proton beams (below 18 MeV);

2. computationally, by developing a Monte Carlo track structure application for the computation of microdosimetric quantities in water, to be used for the calculation of macroscopic dose-averaged LET distributions.

The main results obtained from this work are summarised in the following paragraphs.

Preparation of a radiobiology beam line at the 18 MeV proton cyclotron facility at the CNA Two different irradiation setups for radiobiology experiments were tested at the cyclotron external beam line installed at the CNA. Both setups resorted to a passive scattering of the beam, by means of foils of different thicknesses and materials, to obtain low-intensity broad homogeneous profiles suitable for the irradiation of mono-layer cell cultures. Finally, a beam line irradiation setup, based on a completely defocused beam, a 500 µm thick aluminium scattering foil and an ionisation chamber, was identified as that giving the best results in terms of dose rate and beam homogeneity. With this configuration, a homogeneous irradiation field was achieved, with average deviations from homogeneity lower than 4% in the whole sample area (3.5 cm diameter) for a beam energy of 12.8 MeV and a dose rate of about $5 - 6\,\mathrm{Gy\,min^{-1}}$, close to the value used in the clinics (usually $2\,\mathrm{Gy\,min^{-1}}$). Furthermore, a Monte Carlo simulation of the beam line and experimental setup was developed, using the Geant4 Monte Carlo toolkit. Simulations were tested towards experimental measurements and reproduced experimental data in what concerned the beam energy distribution and dose profiles with differences lower than 1% and 10%, respectively.
Finally, a protocol for the irradiation of biological samples was established, consisting in: (1) an accurate alignment of the target position with the beam axis by means of the steering magnets of the cyclotron external beam line; (2) a verification of the beam profile homogeneity, prior to irradiation, with radiochromic EBT3 films and (3) a control of the environmental parameters, such as temperature and pressure, to avoid extra stress to the cells that could lead to biased results.
The results of this work were published in two journals [134, 135].

Microdosimetry-based dose-averaged linear energy transfer calculation for mono-energetic proton beams: a Monte Carlo study with GEANT4-DNA A Monte Carlo code for the computation of microdosimetric distributions generated by proton track segments in liquid water was developed. With our code, the averages of the main microdosimetric variables (chord length, specific energy and lineal energy) in spherical sites can be obtained, including those of energy imparted per single proton collision, a feature that is foreseen to be included in an example of one of the next official releases of Geant4. This last quantity, in particular, is especially important, as the weighted average of the energy imparted per collision of the traversing proton can be used to obtain macroscopic dose-averaged LET as proposed by Kellerer [68].
The code implements two sampling algorithms for the scoring of the quantities of interest, uniform and weighted, the first serving as a reference for the second. By choosing appropriately the dimensions of the scoring volume, weighted sampling

results could be considered as equivalent to uniform ones. Furthermore, with the weighted method efficient and unbiased calculations of microdosimetric distributions could be obtained, saving computational time if compared to uniform calculations.

The code was tested and benchmarked by comparing dose-averaged lineal energy results with dose-averaged LET values obtained from Kellerer's formula. A very good agreement between simulation results and theoretical expectations was met, with relative percentage differences always lower than 6%.

The results obtained with our code were published in three papers [115, 121, 122], where they were used as a base for the definition of analytical microdosimetric models.

Irradiation of mono-layer cell cultures at the cyclotron radiobiology beam line Once identified the best setup for the irradiation of cell samples, a preliminary irradiation of U2OS mono-layer cell cultures was conducted, with success. In this occasion, a concomitant irradiation with photons and protons was carried out, to compare the differences in damage response between the two radiation qualities.

At the cyclotron radiobiology beam line, cells were irradiated without growth medium in the vertical position, trying to reduce as much as possible the time of exposure to air. Overall, the irradiation took approximately 30 minutes, after which the cells were immediately treated to be analysed with immunofluorescence.

No major differences emerged in terms of damage response at the proton LET considered ($3.8\,\mathrm{keV\,\mu m^{-1}}$ in water), a result that was not unexpected, since the proton RBE at those energies is close to 1.1. This result, however, served as a proof of the validity of the cyclotron beam line for radiobiology experiments, since the irradiation conditions did not alter the outcome of the experiment and the cells did not suffer from the stress of transportation, temperature variations and exposure to air.

One of the main limitations of the setup proposed is that irradiations cannot be performed in a sterile environment, enhancing the probabilities of bacterial infections. Therefore, it was not possible to perform a clonogenic essay, which is one of the most common ways to derive proton RBE. With the aim of computing a rough estimation of the expected RBE for the cell line and proton LET considered, the microdosimetric kinetic model was applied. To do so, our microdosimetry Monte Carlo code was used to extract the value of the dose-averaged lineal energy in the cell layer, reproducing in the simulation the experimental irradiation conditions. From this calculation, the expected U2OS proton survival curve could be obtained and compared with the experimental photon survival curve, resulting in an RBE at 10% survival of 1.1, as expected.

5.2 Future perspectives

Regarding the setup proposed for the irradiation of biological samples, various studies are foreseen to extend the energy range available for radiobiology experiments. In principle, lower energies should be easily obtained by further degrading the beam, eventually decreasing the dose rate while improving the dose homogeneity over the sample surface. With respect to higher energies, different foils with higher atomic numbers and lower thicknesses could be taken into consideration for the dispersion of the beam line in vacuum, thus achieving an increased beam aperture with lower energy degradation. A detailed study of the effects of changing the foil thickness and material will be performed in the next future, using the Monte Carlo simulation of the beam line to identify the best configuration. The addition of a second ionisation chamber, right after the exit window of the external beam line, has also been planned, to allow for a precise measurement of the beam fluence independent from Monte Carlo simulations. Furthermore, the design of a system to irradiate cell cultures within their growth medium is fundamental to exploit the potential of the radiobiology beam line, and is currently under study. Indeed, this would allow to investigate the kinetics of repair and to build clonogenic survival curves. On one hand, a system similar to that described in [136] could be built, with seeded culture plates vertically inserted in a box filled with medium and extracted only for the time of irradiation. On the other hand, customised culture plates, like the ones in [109], or commercial ones with an ultra-thin bottom could be used, in order to allow irradiations from behind with minimum energy loss.

Concerning our code for the computation of microdosimetric quantities, more studies are foreseen to test its robustness against variations of site dimensions and shape. Indeed, the implementation of cylindrical sites would be highly interesting as many microdosimeters have this shape. A collaboration has also been established, to compare the results obtained with our Geant4-DNA application with the PARTRAC code [137], a well-established tool for track structure calculations. Furthermore, the validity of Kellerer's formula and the performances of the code should be tested for higher proton energies, at least comparable to the ones used in clinical applications.

At the radiobiology beam line, experimental measurements with 3D solid state microdetectors [138–140] are also foreseen in the future, to measure lineal energy distributions and compared them with Monte Carlo ones. This measurements would be of great interest for radiobiology experiments, as they would allow for a direct evaluation of the RBE through the MK model. Finally, following our first irradiation of cell cultures (described in this thesis), that has been carried out successfully, we espect to begin a prolific collaboration with our colleagues at the CABIMER, thus establishing new research lines in our group related to radiobiology.

List of Figures

List of Tables

Bibliography

[1] Wild, CP, Weiderpass, E, Stewart, BW, editors. World Cancer Report: cancer research for cancer prevention. Lyon: International Agency for Research on Cancer; 2020.

[2] IAEA & ICRU. Relative biological effectiveness in ion beam therapy (Technical Report No. 461). Vienna: International Atomic Energy Agency; 2008.

[3] Borras, JM, Lievens, Y, Barton, M, Corral, J, Ferlay, J, Bray, F, Grau, C. How many new cancer patients in Europe will require radiotherapy by 2025? An ESTRO–HERO analysis. Radiother Oncol 2016;119(1):5–11. doi:10.1016/j.radonc.2016.02.016.

[4] Bryant, AK, Banegas, MP, Martinez, ME, Mell, LK, Murphy, JD. Trends in radiation therapy among cancer survivors in the United States, 2000–2030. Cancer Epidemiol Biomarkers Prev 2017;26(6):963–70. doi:10.1158/1055-9965.EPI-16-1023.

[5] Galvin, JM, Ezzell, G, Eisbrauch, A, Yu, C, Butler, B, Xiao, Y, et al. Implementing IMRT in clinical practice: a joint document of the American Society for Therapeutic Radiology and Oncology and the American Association of Physicists in Medicine. Int J Radiation Oncology Biol Phys 2004;58(5):1616–34. doi:10.1016/j.ijrobp.2003.12.008.

[6] Rehman, J, Zahra, Ahmad, N, Khalid, M, Asghar, HMNHK, Gilani, ZA, et al. Intensity modulated radiation therapy: a review of current practice and future outlooks. J Radiat Res Appl Sci 2018;11(4):361–7. doi:10.1016/j.jrras.2018.07.006.

[7] Intensity-Modulated Radiation Therapy (IMRT). Radiological Society of North America, Inc. <http://www.radiologyinfo.org/en/pdf/imrt.pdf>; 2019 [accessed 17.09.20].

[8] Orecchia, R, Zurlo, A, Loasses, A, Krengli, M, Tosi, G, Zurrida, S, et al. Particle beam therapy (hadrontherapy): basis for interest and clinical experience. Eur J Cancer 1998;34(4):459–68. doi:10.1016/s0959-8049(97)10044-2.

[9] Wilson, RR. Radiological Use of Fast Protons. Radiology 1946;47(5):487–91. doi:10.1148/47.5.487.

[10] Nuclear Physics for Medicine. Chapter I: Hadrontherapy. <http://archives.esf.org/fileadmin/Public_documents/Publications/Nuclear_Physics_in_Medicine.pdf>; 2014 [accessed 17.09.20].

[11] Durante, M, Loeffler, JS. Charged particles in radiation oncology. Nat Rev Clin Oncol 2010;7(1):37–43. doi:10.1038/nrclinonc.2009.183.

[12] Dinh, JQ, Mahajan, A, Palmer, MB, Grosshans, DR. Particle therapy for central nervous system tumors in pediatric and adult patients. Transl Cancer Res 2012;1(3):137–49. doi:10.3978/j.issn.2218-676X.2012.10.02.

[13] Durante, M, Paganetti, H. Nuclear physics in particle therapy: a review. Rep Prog Phys 2016;79(9):096702–61. doi:10.1088/0034-4885/79/9/096702.

[14] Durante, M, Orecchia, R, Loeffler, JS. Charged-particle therapy in cancer: clinical uses and future perspectives. Nat Rev Clin Oncol 2017;14(8):483–95. doi:10.1038/nrclinonc.2017.30.

[15] ICRU. Prescribing recording and reporting proton-beam therapy (ICRU Report 78). J ICRU 2007;7(2):1–210. doi:10.1093/jicru/ndm021.

[16] Mohan, R, Peeler, CR, Guan, F, Bronk, L, Cao, W, Grosshans, DR. Radiobiological issues in proton therapy. Acta Oncol 2017;56(11):1367–73. doi:10.1080/0284186X.2017.1348621.

[17] Paganetti, H, Niemierko, A, Ancukiewicz, M, Gerweck, LE, Goitein, M, Loeffler, JS, Suit, HD. Relative biological effectiveness (RBE) values for proton beam therapy. Int J Radiat Oncol Biol Phys 2002;53(2):407–21. doi:10.1016/s0360-3016(02)02754-2.

[18] Matsuura, T, Egashira, Y, Nishio, T, Matsumoto, Y, Wada, M, Koike, S, et al. Apparent absence of proton beam dose rate effect and possible differences in RBE between Bragg peak and plateau. Med Phys 2010;37(10):5376–81. doi:10.1118/1.3490086.

[19] Paganetti, H. Relative biological effectiveness (RBE) values for proton beam therapy. Variations as a function of biological endpoint, dose and linear energy transfer. Phys Med Biol 2014;59(22):R419–72. doi:10.1088/0031-9155/59/22/R419.

[20] Jones, B. Why RBE must be a variable and not a constant in proton therapy. Brit J Radiol 2016;89(1063):20160116. doi:10.1259/bjr.20160116.

[21] Giovannini, G, Böhlen, T, Cabal, G, Bauer, J, Tessonnier, T, Frey, K, et al. Variable RBE in proton therapy: comparison of different model predictions and their influence on clinical like-scenarios. Radiat Oncol 2016;11(68):1–16. doi:10.1186/s13014-016-0642-6.

[22] Carabe, A, Moteabbed, M, Depauw, N, Schuemann, J, Paganetti, H. Range uncertainty in proton therapy due to variable biological effectiveness. Phys Med Biol 2012;57(5):1159–72. doi:10.1088/0031-9155/57/5/1159.

[23] Leroy, C, Rancoita, P. Principles of Radiation Interaction in Matter and Detection. Singapore: World Scientific Publishing Co. Pte. Ltd.; 2004.

[24] Breuer, H, Smit, BJ. Proton Therapy and Radio-surgery. Berlin, Heidelberg: Springer-Verlag; 2000.

[25] Paganetti, H, editor. Proton therapy physics. Boca Raton (FL): Taylor & Francis Group; 2011.

[26] Knoll, GF. Radiation Detection and Measurement. New York: John Wiley & Sons, Inc; 2000.

[27] Bethe, H. Zur theorie des durchgangs schneller korpuskularstrahlen durch materie. Ann Phys 1930;397(3):325–400. doi:10.1002/andp.19303970303.

[28] Bloch, F. Zur bremsung rasch bewegter teilchen beim durchgang durch materie. Ann Phys 1933;408(3):285–320. doi:10.1002/andp.19334080303.

[29] Fano, U. Penetration of protons, alpha particles and mesons. Ann Rev Nucl Sci 1963;13(1):1–66. doi:10.1146/annurev.ns.13.120163.000245.

[30] Kim, YS. Density Effect in dE/dx of Fast Charged Particles Traversing Various Biological Materials. Radiat Res 1973;56(1):21–7. doi:10.2307/3573787.

[31] PSTAR. Stopping-power and range tables for protons. National Insitute of Standards and Technology (NIST). <https://physics.nist.gov/PhysRefData/Star/Text/PSTAR.html>; [accessed 17.09.20].

[32] Barkas, HW. Nuclear research emulsions. New York: Academic Press; 1963–73.

[33] ICRU. Key data for ionizing-radiation dosimetry: measurement standards and applications (ICRU Report 90). J ICRU 2014;14(1):1–110. doi:10.1093/jicru/ndw043.

[34] Newhauser, WD., Zhang, R. The physics of proton therapy. Phys Med Biol 2015;60(8):R155–209. doi:10.1088/0031-9155/60/8/R155.

[35] Bodine, EN, Monia, KL. A proton therapy model using discrete difference equations with an example of treating hepatocellular carcinoma. Math Biosci Eng 2017;14(4):881–99. doi:10.3934/mbe.2017047.

[36] Tabata, T, Ito, R, Okabe, S. Generalized semiempirical equations for the extrapolated range of electrons. Nucl Instrum Meth 1972;103:85–91. doi:10.1016/0029-554X(72)90463-6.

[37] Leo, WR. Techniques for Nuclear and Particle Physics Experiments: A How-To Approach. Berlin, Heidelberg: Springer-Verlag; 1994.

[38] Vavilov, PV. Ionization losses of high energy heavy particles. Sov Phys JETP 1957;5(4):749–51.

[39] Bohr, N. On the decrease of velocity of swiftly moving electrified particles in passing through matter. Phyl Mag 1915;30(178):581–612. doi:10.1080/14786441008635432.

[40] Ahlen, SP. Theoretical and experimental aspects of the energy loss of relativistic heavily ionizing particles. Rev Mod Phys 1980;52(653):121–73. doi:10.1103/RevModPhys.52.121.

[41] Seb, DI. Range Straggling of Charged Particles in Various Substances. Sov Phys JETP 1964;18(2):540–541.

[42] Schardt, S, Elsässer, T, Schulz-Ertner, D. Heavy-ion tumor therapy: Physical and radiobiological benefits. Rev Mod Phys 2010;82:383–425. doi:10.1103/RevModPhys.82.383.

[43] Rossi, BB. High-energy Particles. New York: Prentice-Hall physics series; 1952.

[44] Rutherford, E. The scattering of α and β particles by matter and the structure of the atom. Phil Mag Ser 6 1911;21(125):669–88. doi:10.1080/14786440508637080

[45] Highland, VL. Some practical remarks on multiple scattering. Nucl Instrum Meth 1975;129(2):497–99. doi:10.1016/0029-554X(75)90743-0.

[46] Joiner, M, Kogel, A, editors. Basic Clinical Radiobiology, 4th ed. London: Hodder Arnold; 2009.

[47] Hall, EJ, Giaccia, AJ. Radiobiology for the Radiologist, 8th ed. Philadelphia: Lippincott Williams & Wilkins, 2019.

[48] Scholz, M. Effects of Ion Radiation on Cells and Tissues. In: Kausch, H et al., editors. Radiation Effects on Polymers for Biological Use. Advances in Polymer Science, vol 162. Berlin, Heidelberg: Springer; 2003. doi:10.1007/3-540-45668-6_4.

[49] Bäckström, G. Protons, other Ligt Ions, and ^{60}Co Photons: Study of Energy Deposit Clustering via Track Structure Simulations. Acta Universitatis Upsaliensis. Uppsala: Digital Comprehensive Summaries of Uppsala Dissertations from the Faculty of Medicine 930; 2013.

[50] ICRU. Linear Energy Transfer (ICRU Report 16). J ICRU 1970;9(1): 1–51. doi:https://doi.org/10.1093/jicru/os9.1.Report16.

[51] ICRU. Fundamental quantities and units for ionizing radiation (ICRU Report 85). J ICRU 2011;11(1):1–31. doi:10.1093/rpd/ncs077.

[52] Zackrisson, B. Radiobiological cell survival models, a methodological overview. Acta Oncol 1992;31(4):433–41. doi:10.3109/02841869209088286.

[53] Bodgi, L, Canet, A, Pujo-Menjouet, L, Lesne, A, Victor, J, Foray, N. Mathematical models of radiation action on living cells: from the target theory to the modern approaches. A historical and critical review. J Theor Biol 2016;394:93–101. doi:10.1016/j.jtbi.2016.01.018.

[54] Tommasino, F, Scifoni, E, Durante, M. New Ions for Therapy. Int J Part Ther 2016;2(3):428–38. doi:10.14338/IJPT-15-00027.1.

[55] Carabe-Fernandez, A, Dale, RG, Jones, B. The incorporation of the concept of minimum RBE (RBE min) into the linear-quadratic model and the potential for improved radiobiological analysis of high-LET treatments. Int J Radiat Biol 2007;83(1):27–39. doi:10.1080/09553000601087176.

[56] Wedenberg, M, Lind, BK, Hårdemark, B. A model for the relative biological effectiveness of protons: the tissue specific parameter α/β of photons is a predictor for the sensitivity to LET changes. Acta Oncol 2013;52(3):580–8. doi:10.3109/0284186X.2012.705892.

[57] Tilly, N, Johansson, J, Isacsson, U, Medin, J, Blomquist, E, Grusell, E, Glimelius, B. The influence of RBE variations in a clinical proton treatment plan for a hypopharynx cancer. Phys Med Biol 2005;50(12):2765–77. doi:10.1088/0031-9155/50/12/003.

[58] Carabe, A, España, S, Grassberger, C, Paganetti, H. Clinical consequences of relative biological effectiveness variations in proton radiotherapy of the prostate, brain and liver. Phys Med Biol 2013;58(7):2103–17. doi:10.1088/0031-9155/58/7/2103.

[59] Wedenberg, M, Toma-Dasu, I. Disregarding RBE variation in treatment plan comparison may lead to bias in favor of proton plans. Med Phys 2014;41(9):091706. doi:10.1118/1.4892930.

[60] Giantsoudi, D, Grassberger, C, Craft, D, Niemierko, A, Trofimov, A, Paganetti, A. Linear energy transfer-guided optimization in intensity modulated proton therapy: feasibility study and clinical potential. Int J Radiat Oncol Biol Phys 2013;87(1):216–22. doi:10.1016/j.ijrobp.2013.05.013.

[61] Bassler, N, Jäkel, O, Søndergaard, CS, Petersen, JB. Dose- and LET-painting with particle therapy. Acta Oncol 2010;49(7):1170–6. doi:10.3109/0284186X.2010.510640.

[62] Rossi, HH. Spatial distribution of energy deposition by ionizing radiation source. Radiat Res Suppl. 1960;2:290–99. doi:10.2307/3583601.

[63] Rossi, HH. Distribution of radiation energy in the cell. Radiology 1962;78:530–5. doi:10.1148/78.4.530.

[64] Rossi, HH. Correlation of radiation quality and biological effect. Ann N Y Acad Sci 1964;114:4–15. doi:10.1111/j.1749-6632.1964.tb53559.x.

[65] ICRU. Microdosimetry (ICRU Report 36). J ICRU 1983;19(1):1–118. doi:10.1148/radiology.154.2.528.

[66] Kellerer, AM. Microdosimetry and the theory of straggling. In: Biophysical Aspects of Radiation Quality. Second Panel Report. Vienna: International Atomic Energy Agency; 1968.

[67] Kellerer, AM. Analysis of patterns of energy deposition. In: Ebert, HG, editor. Proceedings Second Symposium on Microdosimetry; 1970. doi:10.5282/ubm/epub.7951.

[68] Kellerer, AM. Fundamentals of microdosimetry. In: Kase, KR, Bjärngard, BE, Attix, FH, editors. The Dosimetry of Ionizing Radiation. Cambridge: Academic Press Inc.; 1985.

[69] Hawkins, RB. A Microdosimetric-Kinetic Model of cell death from exposure to ionizing radiation of any LET, with experimental and clinical applications. Int J Radiat Biol 1996;69(6):739–55. doi:10.1080/095530096145481.

[70] Hawkins, RB. A Microdosimetric-Kinetic Model for the sensitization of V79 cells to radiation by incorporation fo bromodeooxyuridine. Radiat Res 2001;155(5):698–702. doi:10.1667/0033-7587(2001)155[0698:amkmft]2.0.co;2.

[71] Hawkins, RB. A Microdosimetric-Kinetic Model for the effect of non-Poisson distribution of lethal lesions on the variation of RBE with LET. Radiat Res 2003;160(1):61–9. doi:10.1667/rr3010.

[72] Kellerer, AM, Rossi, HH. A generalized formulation of dual radiation action. Radiat Res 2012;178(2):AV204–13. doi:10.1667/rrav17.1.

[73] Sato, T, Furusawa, Y. Cell survival fraction estimation based on the probability densities of domain and cell nucleus specific energies using improved microdosimetric kinetic models. Radiat Res 2012;178(4):341–56. doi:10.1667/rr2842.1.

[74] Hawkins, RB. A microdosimetric-kinetic theory of the dependence of the RBE for cell death on LET. Med Phys 1998;25(7):1157–70. doi:10.1118/1.598307.

[75] Kase, Y, Kanai, T, Matsumoto, Y, Furusawa, Y, Okamoto, H, Asaba, T, et al. Microdosimetric measurements and estimation of human cell survival for heavy-ion beams. Radiat Res 2006;166(4):629–38. doi:10.1667/RR0536.1.

[76] Rogers, DWO. Fifty years of Monte Carlo simulations for medical physics. Phys Med Biol 2006;51(13):R287–301. doi:10.1088/0031-9155/51/13/R17.

[77] Ziegler, JF, Ziegler, MD, Biersack, JP. SRIM – The stopping and range of ions in matter. Nucl Instrum Meth Phys Res B 2010;268(11):1818–23. doi:10.1016/j.nimb.2010.02.091.

[78] Agostinelli, S, Allison, J, Amako, K, Apostolakis, J, Araujo, H, Arce, P, et al. Geant4 – a simulation toolkit. Nucl Instrum Meth Phys Res A 2003;506(3):250–303. doi:10.1016/S0168-9002(03)01368-8.

[79] Allison, J, Amako, K, Apostolakis, J, Araujo, H, Arce, P, Asai, M, et al. Geant4 developments and applications. IEEE T Nucl Sci 2006;53(1):270–78. doi:10.1109/TNS.2006.869826.

[80] Allison, J, Amako, K, Apostolakis, J, Arce, P, Asai, M, Aso, T, et al. Recent developments in Geant4. Nucl Instrum Meth Phys Res A 2016;835:186–225. doi:10.1016/j.nima.2016.06.125.

[81] Incerti, S, Baldacchino, G, Bernal, M, Capra, R, Champion, C, Francis, Z, et al. The Geant4-DNA project. Int J Model Simul Sci Comput 2010;1(2):157–78. doi:10.1142/S1793962310000122.

[82] Incerti, S, Ivanchenko, A, Karamitros, M, Mantero, A, Moretto, P, Tran, HN, et al. Comparison of Geant4 very low energy cross section models with experimental data in water. Med Phys 2010;37(9):4692–708. doi:10.1118/1.3476457.

[83] Bernal, MA, Bordage, MC, Brown, JMC, Davídková, M, Delange, E, El Bitar, Z, et al. Track structure modeling in liquid water: A review of the Geant4-DNA very low energy extension of the Geant4 Monte Carlo simulation toolkit. Phys Medica 2015;31(8):861–74. doi:10.1016/j.ejmp.2015.10.087.

[84] Incerti, S, Kyriakou, I, Bernal, MA, Bordage, MC, Francis, Z, Guatelli, S et al. Geant4-DNA example applications for track structure simulations in liquid water: a report from the Geant4-DNA Project. Med Phys 2018;45(8):e722-39. doi:10.1002/mp.13048

[85] IAEA. Absorbed dose determination in external beam radiotherapy: an international code of practice for dosimetry based on standards of absorbed dose to water (Technical Report No. 398). Vienna: International Atomic Energy Agency; 2000.

[86] Podgorsak, EB. Radiation oncology physics: a handbook for teachers and students. Vienna: International Atomic Energy Agency; 2005.

[87] Devic, S. Radiochromic film dosimetry: past, present and future. Phys Medica 2011;27(3):122–34. doi:10.1016/j.ejmp.2010.10.001.

[88] Piermattei, A, Miceli, R, Azario, L, Fidanzio, A, Delle Canne, S, De Angelis, C, et al. Radiochromic film dosimetry of a low energy proton beam. Med Phys 2000;27(7):1655–60. doi:10.1118/1.599032.

[89] Zhao, L, Das, IJ. Gafchromic EBT film dosimetry in proton beams. Phys Med Biol 2010;55(10):N291–301. doi:10.1088/0031-9155/55/10/N04.

[90] Kirby, D, Green, S, Palmans, H, Hugtenburg, R, Wojnecki, C, Parker, D. LET dependence of GafChromic films and an ion chamber in low-energy proton dosimetry. Phys Med Biol 2010;55(2):417–33. doi:10.1088/0031-9155/55/2/006.

[91] Fiorini, F, Kirby, D, Thompson, J, Green, S, Parker, DJ, Jones, B, Hill, MA. Under-response correction for EBT3 films in the presence of proton spread out Bragg peaks. Phys Medica 2014;30(4):454–61. doi:10.1016/j.ejmp.2013.12.006.

[92] Reinhardt, S, Würl, M, Greubel, C, Humble, N, Wilkens, JJ, Hillbrand, M, et al. Investigation of EBT2 and EBT3 films for proton dosimetry in the 4–20 MeV energy range. Radiat Environ Biophys 2015;54:71–79. doi:10.1007/s00411-014-0581-2.

[93] Battaglia, MC, Espino, JM, Gallardo, MI, Lallena, AM, Fernandez, B, Cortés-Giraldo, MA, et al. EBT3 film calibration in the Bragg peak region for proton beams below 5 MeV. Nucl Instrum Meth Phys Res B 2019;444:117–124. doi:10.1016/j.nimb.2019.02.018.

[94] Soares, CG. New developments in radiochromic film dosimetry. Radiat Prot Dosimetry 2006;120(1-4):100–6. doi:10.1093/rpd/nci698.

[95] Khachonkham, S, Dreindl, R, Heilemann, G, Lechner, W, Fuchs, H, Palmans, H, et al. Characteristics of EBT-XD and EBT3 radiochromic film dosimetry for photon and proton beams. Phys Med Biol 2018;63(6):065007. doi:10.1088/1361-6560/aab1ee.

[96] Shi, C, Chen, C, Mah, D, Chan, MF. Monte Carlo calculation of the mass stopping power of EBT3 and EBT-XD films for protons for energy ranges of 50-400 MeV. Prec Radiat Oncol 2018;2(4):106–13. doi:10.1002/pro6.55.

[97] Niroomand-Rad, A, Blackwell, CR, Coursey, BM, Gall, KP, Galvin, JM, McLaughlin, WL, et al. Radiochromic film dosimetry: Recommendations of AAPM Radiation Therapy Committee Task Group 55. Med Phys 1998;25(11):2093–115. doi:10.1118/1.598407.

[98] GAFChromic™ EBT3 film specifications. <http://www.gafchromic.com/documents/EBT3_Specifications.pdf>; [accessed 17.09.20].

[99] Borca, VC, Pasquino, M, Russo, G, Grosso, P, Cante, D, Sciacero, P, et al. Dosimetric characterization and use of GAFCHROMIC EBT3 film for IMRT dose verification. J Appl Clin Med Phys 2013;14(2):4111. doi:10.1120/jacmp.v14i2.4111.

[100] Mayer, RR, Ma, F, Chen, Y, Miller, RI, Belard, A, McDonough, J, O'Connell, JJ. Enhanced dosimetry procedures and assessment for EBT2 radiochromic film. Med Phys 2012;39(4):2147–55. doi:10.1118/1.3694100.

[101] Azorín, JFP, García, LIR, Martí-Climent JM. A method for multichannle dosimetry with EBT3 radiochromic films. Med Phys 2014;41(6):062101. doi:10.1118/1.4871622.

[102] Belli, M, Cherubini, R, Galeazzi, G, Mazzucato, S, Moschini, G, Sapora, O, et al. Proton irradiation facility for radiobiological studies at a 7 MV Van de Graaf accelerator. Nucl Instrum Meth Phys Res A 1987;256(3):576–80. doi:10.1016/0168-9002(87)90304-4.

[103] Scampoli, P, Casale, M, Durante, M, Grossi, G, Pugliese, M, Gialanella, G. Low-energy light ion irradiation beam-line for radiobiological studies. Nucl Instrum Meth Phys Res B 2001;174(3):337–43. doi:10.1016/S0168-583X(00)00622-4.

[104] Huerta-Parajon, M, Martinez-Ballarin, R, Abad, E. Design study of the ESS-Bilbao 50 MeV proton beam line for radiobiological studies. Nucl Instrum Meth Phys Res B 2015;344:33–8. doi:10.1016/j.nimb.2014.11.093.

[105] Tordis, JD, Rykkelid, AM, Stokkevåg, CH, Mairani, A, Görgen, A, Edin, NJ, et al. Monte Carlo simulations of a low energy proton beamline for radiobiological experiments. Acta Oncol 2017;56(6):779–86. doi:10.1080/0284186X.2017.1289239.

[106] Battaglia, MC, Schardt, D, Espino, JM, Gallardo, MI, Cortés-Giraldo, MA, Quesada, JM, et al. Dosimetric response of radiochromic films to protons of low energies in the Bragg peak region. Phys Rev Accel Beams 2016;19:064701.doi:10.1103/PhysRevAccelBeams.19.064701.

[107] Lühr, A, Neubeck, C, Krause, M, Troost, EGC. Relative biological effectiveness in proton beam therapy – Current knowledge and future challenges. Clin Transl Oncol 2018;9:35–41. doi:10.1016/j.ctro.2018.01.006.

[108] Devic, S, Seuntjens, J, Hegyi, G, Podgorsak, EB, Soares, CG, Kirov, AS, et al. Dosimetric properties of improved GafChromic films for seven different digitizers. Med Phys 2004;31(9):2392–401. doi:10.1118/1.1776691.

[109] Belli, M, Cera, F, Cherubini, R, Dalla Vecchia, M, Haque, AM, Lanzini, F, et al. RBE-LET relationship for cell inactivation and mutation induced by low energy protons in V79 cells: Further results at the LNL facility. Int J Radiat Biol 1998;74(4):501–9. doi:10.1080/095530098141375.

[110] Peeler, CR, Mirkovic, D, Titt, U, Blanchard, P, Gunther, JR, Mahajan, A, et al. Clinical evidence of variable proton biological effectiveness in pediatric patients treated for ependymoma. Radiother Oncol 2016;121(3):395–401. doi:10.1016/j.radonc.2016.11.001.

[111] Grün, R, Friedrich, T, Traneus, E, Scholz, M. Is the dose-averaged LET a reliable predictor for the relative biological effectiveness? Med Phys 2019;46(2):1064–74. doi:10.1002/mp.13347.

[112] Fager, M, Toma-Dasu, I, Kirk, M, Dolney, D, Diffenderfer, ES, Vapiwala, N, Carabe, A. Linear energy transfer painting with proton therapy: a means of reducing radiation doses with equivalent clinical effectiveness. Int J Radiat Oncol Biol Phys 2015;91(5):1057–64. doi:10.1016/j.ijrobp.2014.12.049.

[113] Unkelbach, J, Botas, P, Giantsoudi, D, Gorissen, BL, Paganetti, H. Reoptimization of intensity modulated proton therapy plans based on linear energy transfer. Int J Radiat Oncol Biol Phys 2016;96(5):1097–106. doi:10.1016/j.ijrobp.2016.08.038.

[114] Kellerer, AM, Chmelevsky, D. Criteria for the applicability of LET. Radiat Res 1975;63(2):226–34. doi:10.2307/3574148.

[115] Bertolet, A, Baratto-Roldán, A, Barbieri, S, Baiocco, G, Carabe, A, Cortés-Giraldo, MA. Dose-averaged LET calculation for proton track segments using microdosimetric Monte Carlo simulations. Med Phys 2019;46(9):4184–92. doi:10.1002/mp.13643.

[116] Kellerer, AM. Chord-length distributions and related quantities for spheroids. Radiat Res 1984;98(3):425–37. doi:10.2307/3576477.

[117] Cortés-Giraldo, MA, Carabe, A. A critical study of different Monte Carlo scoring methods of dose average linear-energy-transfer maps calculated in voxelized geometries irradiated with clinical proton beams. Phys Med Biol 2015;60(7):2645–69. doi:10.1088/0031-9155/60/7/2645.

[118] Kyriakou, I, Emfietzoglou, D, Ivanchenko, V, Bordage, MC, Guatelli, S, Lazarakis, P, et al. Microdosimetry of electrons in liquid water using the low-energy models of Geant4. J Appl Phys 2017;122:024303. doi:10.1063/1.4992076.

[119] Famulari, G, Pater, P, Enger, SA. Microdosimetry calculations for monoenergetic electrons using Geant4-DNA combined with a weighted track sampling algorithm. Phys Med Biol 2017;62(13):5495–508. doi:10.1088/1361-6560/aa71f6.

[120] Walters, BRB, Kawrakow, I, Rogers, DWO. History by history statistical estimator in the BEAM code system. Med Phys 2002;29(12):2745–52. doi:10.1118/1.1517611.

[121] Perales, A, Baratto-Roldán, A, Kimstrand, P, Cortés-Giraldo, MA, Carabe, A. Parameterising microdosimetric distributions of mono-energetic proton beams

for fast estimates of y_D and y^*. Biomed Phys Eng Express 2019;5(4):045014. doi:10.1088/2057-1976/ab236a.

[122] Bertolet, A, Baratto-Roldán, A, Cortés-Giraldo, MA, Carabe-Fernandez, A. Segment-averaged LET concept and analytical calculation from microdosimetric quantities in proton radiation therapy. Med Phys 2019;46(9):4204–14. doi:10.1002/mp.13673.

[123] lgcstandards-atcc.org. U-2 OS (ATCC® HTB-96™) <https://www.lgcstandards-atcc.org/products/all/HTB-96.aspx>; [accessed 17.09.20].

[124] Voet, D, Voet, J.G. Biochemistry, 4th ed. Hoboken (NJ): John Wiley & Sons, Inc.; 2011.

[125] Annunziato, AT. DNA Packaging: Nucleosomes and Chromatin. Nature Education 2008;1(1):26.

[126] Johns, HE, Cunningham, JR. The physics of radiology, 4th ed. Springfield (IL): Charles C Thomas Publisher; 1983.

[127] Kliauga, P, Dvorak, R. Microdosimetric measurements of ionization by monoenergetic photons. Radiat Res 1978;73(1):1–20. doi:10.2307/3574570.

[128] Zhang, R, Taddei, PJ, Fitzek, MM, Newhauser, WD. Water equivalent thickness values of materials used in beams of protons, helium, carbon and iron ions. Phys Med Biol 2010;55(9):2481–93. doi:10.1088/0031-9155/55/9/004.

[129] Grosse, N, Fontana, AO, Hug, EB, Lomax, A, Coray, A, Augsburger, M, et al. Deficiency in homologous recombination renders mammalian cells more sensitive to proton versus photon irradiation. Int J Radiat Oncol Biol Phys 2014;88(1):175–81. doi:10.1016/j.ijrobp.2013.09.041.

[130] Gerelchuluun, A, Manabe, E, Ishikawa, T, Sun, L, Itoh, K, Sakae, T, Suzuki, K, et al. The major DNA repair pathway after both proton and carbon-ion radiation is NHEJ, but the HR pathway is more relevant in carbon ions. Radiat Res 2015;183(3):345–56. doi:10.1667/RR13904.1.

[131] Fontana, AO, Augsburger, MA, Grosse, N, Guckenberger, M, Lomax, AJ, Sartori, AA, Pruschy, MN. Differential DNA repair pathway choice in cancer cells after proton- and photon-irradiation. Radiother Oncol 2015;116(3):374–80. doi:10.1016/j.radonc.2015.08.014.

[132] Szymonowicz, K, Krysztofiak, A, Linden, JV, Kern, A, Deycmar, S, Oeck, S, et al. Proton Irradiation Increases the Necessity for Homologous Recombination Repair Along with the Indispensability of Non-Homologous End Joining. Cells 2020;9(4):889. doi:10.3390/cells9040889.

[133] Cao, W, Khabazian, A, Yepes, PP, Lim, G, Poenisch, F, Grosshans, D, Mohan, R. Linear energy transfer incorporated intensity modulated proton therapy optimization. Phys Med Biol 2017;63(1):015013. doi:10.1088/1361-6560/aa9a2e.

[134] Baratto-Roldán, A, Jiménez-Ramos, MC, Battaglia, MC, García-López, J, Gallardo, MI, Cortés-Giraldo, MA, Espino, JM. Feasibility study of a proton irradiation facility for radiobiological measurements at an 18 MeV cyclotron. Instruments 2018;2(4):26. doi:10.3390/instruments2040026.

[135] Baratto-Roldán, A, Jiménez-Ramos, MC, Jimeno, S, Huertas, P, García-López, J, Gallardo, MI, et al. Preparation of a radiobiology beam line at the 18 MeV proton cyclotron facility at CNA. Phys Medica 2020;74:19–29. doi:10.1016/j.ejmp.2020.04.022.

[136] Kraft-Weyrather, W, Kraft, G, Ritter, S, Scholz, M, Stanton, JA. The preparation of biological targets for heavy-ion experiments up to 20 MeV/u. Nucl Instrum Meth Phys Res A 1989;282(1):22–7. doi:10.1016/0168-9002(89)90104-6.

[137] Friedland, W, Kundrát, P. Track structure based modelling of chromosome aberrations after photon and alpha-particle irradiation. Mutat Res 2013;756(1-2):213–23. doi:10.1016/j.mrgentox.2013.06.013.

[138] Guardiola, C, Quirion, D, Pellegrini, G, Fleta, C, Esteban, S, Cortés-Giraldo, M, et al. Silicon-based three dimensional microstructures for radiation dosimetry in hadrontherapy. Appl Phys Lett 2015;107(2):023505. doi:10.1063/1.4926962.

[139] Guardiola, C, Fleta, C, Rodríguez, J, Lozano, M, Gómez, F. Preliminary microdosimetric measurements with ultra-thin 3D silicon detectors of a 62 MeV proton beam. J Instrum 2015;10(1):P01008. doi:10.1088/1748-0221/10/01/P01008.

[140] Prieto-Pena, J, Gómez, F, Guardiola, C, Jiménez-Ramos, MC, García-López, A, Baratto-Roldán, A, et al. Impact of charge collection efficienc and electronic noise on the performance of solid state 3D-microdetectors. Phys Med Biol 2020;65(17):175004. doi:10.1088/1361-6560/ab87fa.